

# Rare Earth and Bimetallic Transition Metal Islands at Surfaces

THÈSE N° 7877 (2017)

PRÉSENTÉE LE 24 AOÛT 2017  
À LA FACULTÉ DES SCIENCES DE BASE  
LABORATOIRE DE NANOSTRUCTURES SUPERFICIELLES  
PROGRAMME DOCTORAL EN PHYSIQUE

ÉCOLE POLYTECHNIQUE FÉDÉRALE DE LAUSANNE

POUR L'OBTENTION DU GRADE DE DOCTEUR ÈS SCIENCES

PAR

Dimitrios MOUSADAKOS

acceptée sur proposition du jury:

Prof. F. Mila, président du jury  
Prof. H. Brune, Dr S. Rusponi, directeurs de thèse  
Prof. M. Fonin, rapporteur  
Dr J. Coraux, rapporteur  
Prof. H. Dil, rapporteur



ÉCOLE POLYTECHNIQUE  
FÉDÉRALE DE LAUSANNE

Suisse  
2017



Κατὰ τον δαίμονα ἑαυτοῦ.





# Abstract

This thesis reports on the growth and on the magnetic characterization of nanostructures made of  $3d$ - $4d$  transition metals and rare earths. In all the experiments the nanostructures have been grown by atomic beam epitaxy (ABE) in ultra high vacuum conditions (UHV) by performing growth steps with the precise selection of external parameters as: the deposition flux  $F$ , the sample deposition temperature  $T_{\text{dep}}$  and the sample annealing temperature  $T_{\text{ann}}$ . The morphological and magnetic properties of the nanostructures have been characterized by performing two *in situ* measurement techniques in our experimental setup, namely: scanning tunneling microscopy (STM) and magneto-optical Kerr effect (MOKE).

The first aims of the thesis consisted in the formation of a superlattice of rare earth on the graphene moiré pattern induced by the lattice mismatch of a single graphene layer grown on Ir(111) crystal surface. We report the first cluster superlattice made of rare earths, namely Sm, where clusters nucleate in registry with the moiré pattern, forming a superlattice for deposition temperatures between 80 K and 110 K. Within this temperature range, the Sm superlattice shows long-range order extending over several tens of nanometers and a cluster size distribution competing with the finest superlattices grown by ABE. Sm cluster spatial order is preserved, up to a coverage of 0.5 ML yielding a mean cluster size of 50 atoms, while for higher coverages coalescence starts. Moreover, Sm clusters with a mean size of 9 atoms are thermally stable up to  $T_{\text{ann}} = 130$  K from where on the order is lost and the density reduces progressively by cluster coalescence. Similar experiments carried out for Dy in the same deposition temperature range show the absence of cluster arrays.

The second part focused on the enhancement of the magnetic anisotropy energy (MAE) of bimetallic nanostructures of Co-core, grown on Pt(111), by forming atomically sharp interlines and interfaces with three  $4d$  elements, namely Ag, Pd and Rh. Our approach is based on the experimental measurement of the island magnetic susceptibility  $\chi(T)$  and morphology by means of MOKE and STM, respectively, combined with magnetic simulation analysis in order to quantify the different contributions to the island magnetic anisotropy. The monolayer capping for all studied elements contributes positively to the out-of-plane MAE of Co islands, with Pd giving the largest increase in the magnetic hardness. In addition, the capping with two Pd monolayers of pure Co islands maximizes the blocking temperature  $T_b$ . However, the lateral decoration of Co islands with all elements contributes negatively to MAE, with the Co/Pd shell giving the smallest effect

---

and Rh the largest. Morphologically, Ag was found to produce a partial decoration of the Co island edges while Rh completely decorates laterally Co islands forming a rim of irregular shape without nucleating on top of Co islands for the used deposition parameters. Simulations of the magnetization reversal process by using coherent rotation (CR) and/or domain wall nucleation and propagation (DW) reversal models including different contributions to the MAE for atoms located at the interface ( $K_s$ ) and at interline ( $K_p$ ) and an exchange interaction between Co and  $4d$  transition metals have reproduced the experimental  $\chi'(T)$  and  $\chi''(T)$  curves.

Key words: magnetic nanostructure, magnetic cluster, magnetic anisotropy, magnetic susceptibility, graphene, graphene moiré, rare earth clusters, cobalt, rhodium, palladium, silver, samarium, dysprosium, scanning tunneling microscopy (STM), magneto-optical kerr effect (MOKE).

# Résumé

Cette thèse traite de la croissance et de la caractérisation magnétique des nanostructures composées de métaux de transition  $3d-4d$  et de terres rares. Dans toutes les expériences les nanostructures ont été formées par épitaxie par jet atomique (ABE) en environnement ultravide (UHV). Des paramètres externes sont choisis précisément pour chaque étape de la croissance : le flux de déposition  $F$ , la température de déposition de l'échantillon  $T_{\text{dep}}$  et la température de recuit  $T_{\text{ann}}$ . Les propriétés morphologique et magnétiques des nanostructures ont été déterminées *in situ* par deux techniques de mesure dans notre dispositif expérimental : La microscopie à effet tunnel (STM) et l'effet magnéto-optique Kerr (MOKE).

Le premier objectif de cette thèse est la formation d'un super réseau de terre rare sur un graphène moiré induit par le décalage de la couche de graphène sur la surface de cristal d'iridium Ir(111). Nous avons créé le premier super réseau constitué de terres rares, à savoir du Sm, où les clusters se forment d'après le motif moiré, formant un super réseau pour des températures de dépositions entre 80 K et 110 K. Dans cette gamme de température, le super réseau de Sm montre un ordre à longue distance s'étendant sur plusieurs dizaines de nanomètres et une distribution de la taille des clusters rivalisant avec les meilleurs super réseaux obtenus par ABE. L'ordre spécial des clusters de Sm est préservé jusqu'à un recouvrement de 0.5 ML, lequel correspond à une taille moyenne des clusters de 50 atomes. Pour des recouvrements plus importants les clusters commencent à fusionner. De plus, les clusters de Sm avec une taille moyenne de 9 atomes sont thermiquement stables jusqu'à une température  $T_{\text{ann}} = 130$  K à partir de laquelle l'ordre est perdu et la densité diminue progressivement à cause des fusions de cluster. Des expériences similaires avec du Dy menées dans la même gamme de température de déposition montrent l'absence d'ordre des clusters.

La deuxième partie se concentre sur l'amélioration de l'énergie d'anisotropie magnétique (MAE) de nanostructures bimétalliques ayant un cœur de Cobalt, fabriquées sur un cristal Pt(111). L'amélioration est obtenue grâce à la formation d'interlignes et d'interfaces atomiques avec des éléments  $4d$ , à savoir de l'argent, de palladium et du rhodium. Notre approche est basée sur la mesure expérimentale de la susceptibilité  $\chi(T)$  magnétique de l'îlot, et de la morphologie par MOKE and STM respectivement, combinée avec des simulations du magnétisme pour quantifier les différentes contributions sur l'anisotropie magnétiques des îlots. Le recouvrement par une monocouche contribue positivement au MAE des îlots de cobalt pour tous les éléments étudiés, le palladium donnant la plus grande

---

augmentation de la dureté magnétique. De plus, le recouvrement par deux monocouches de Pd d'îlot de Co pure maximise la température de blocage  $T_b$ . Cependant, la décoration latérale des îlots de Co avec tous les éléments contribue négativement au MAE, la coquille Co/Pd donnant le plus petit effet et le Rh le plus grand. Morphologiquement, l'argent produit une décoration partielle des bords des îlots de Co alors que le rhodium décore complètement les îlots de Cobalt en formant des rebords irréguliers sans nucléation sur les îlots de Cobalt avec les paramètres de dépositions utilisées. Les simulations du processus de renversement de la magnétisation ont été faites en utilisant un renversement cohérent (CR) et/ou par modèle de renversement par formation et propagation de parois de domaine (DW) incluant différentes contributions sur le MAE pour des atomes localisés à l'interface ( $K_s$ ) et à l'interligne ( $K_p$ ) et une interaction d'échange entre le Cobalt et les métaux de transitions  $d$ . Elles ont reproduit les courbes  $\chi'(T)$  et  $\chi''(T)$  obtenues de manière expérimentale.

Mots clefs : Nanostructures magnétique, cluster magnétiques, anisotropie magnétique, susceptibilité magnétique, graphène, graphène moiré, cluster de terres rares, cobalt, rhodium, palladium, argent, samarium, dysprosium, microscopie électronique à balayage (STM), effet magnéto-optique Kerr (MOKE).

# Contents

<b>Abstract (English/Français)</b>	<b>v</b>
<b>Frequently Used Abbreviations</b>	<b>xi</b>
<b>1 Introduction</b>	<b>1</b>
1.1 History of Magnetic Disk Drives . . . . .	1
1.2 The Current State of The Art in Hard Drives . . . . .	3
1.3 The State of the Art in MRAMs . . . . .	6
1.4 Thesis Outline . . . . .	8
<b>2 Basics of nanomagnetism and nanostructure growth by ABE</b>	<b>11</b>
2.1 Nanomagnetism . . . . .	11
2.1.1 Basic Interactions . . . . .	11
2.1.2 Magnetic Anisotropy . . . . .	13
2.1.3 Magnetization Reversal . . . . .	14
2.1.4 Superparamagnetism . . . . .	15
2.2 Nucleation and Growth . . . . .	18
2.2.1 Processes in Epitaxial Growth . . . . .	18
2.2.2 Rate Equations and Scaling Laws . . . . .	19
2.2.3 Growth Regimes . . . . .	21
2.2.4 Island Shapes . . . . .	21
2.2.5 Island Size Distribution . . . . .	22
2.3 Graphene . . . . .	24
2.3.1 Growth and Structure of Graphene on Ir(111) . . . . .	25
2.3.2 Graphene on Ir(111) as Template for Cluster Superlattice Growth	26
<b>3 Experimental Methods</b>	<b>29</b>
3.1 Scanning Tunneling Microscopy . . . . .	29
3.2 Magneto-Optical Kerr Effect . . . . .	32
<b>4 MBE Chamber and Sample Preparation</b>	<b>35</b>
4.1 The Ultra High Vacuum System . . . . .	35
4.2 Sample Preparation . . . . .	38
4.2.1 Metal Deposition . . . . .	38

## Contents

---

4.2.2	Graphene Growth . . . . .	39
<b>5</b>	<b>Nucleation of Sm and Dy Clusters on Graphene/Ir(111)</b>	<b>41</b>
5.1	Introduction . . . . .	41
5.2	Sm/gr/Ir(111) . . . . .	43
5.3	Dy/gr/Ir(111) . . . . .	49
5.4	Conclusions . . . . .	50
<b>6</b>	<b>Tuning the MAE of Bimetallic Nanostructures</b>	<b>53</b>
6.1	From Thin Films to 2D Nanostructures . . . . .	55
6.2	Engineering Sharp Interlines and Interfaces . . . . .	56
6.3	Magnetization Reversal Simulations . . . . .	58
6.4	Dipolar Interactions . . . . .	60
6.5	Co/Ag Interline and Interface . . . . .	61
6.5.1	Decoration morphology . . . . .	61
6.5.2	Magnetic characterization . . . . .	64
6.6	Co/Pd Interface . . . . .	68
6.7	Co/Rh Interline and Interface . . . . .	72
6.8	Multilayer Pd Capping of Co islands . . . . .	77
6.9	Conclusions . . . . .	78
<b>7</b>	<b>Nucleation and Growth of Rh/Pt(111)</b>	<b>81</b>
7.1	Experimental Procedure . . . . .	81
7.2	Island Nucleation . . . . .	82
7.3	Island Morphology . . . . .	86
7.4	Conclusions . . . . .	87
	<b>Conclusions and Perspectives</b>	<b>89</b>
	<b>Appendix</b>	<b>93</b>
A.1	Supplementary information for Chapter 5 . . . . .	93
A.2	Mathematica Code used in Chapter 6 . . . . .	94
	<b>Bibliography</b>	<b>99</b>
	<b>Acknowledgements</b>	<b>115</b>
	<b>Curriculum Vitae</b>	<b>117</b>

# Frequently Used Abbreviations

The chemical elements used in this thesis are platinum (Pt), iridium (Ir), rhodium (Rh), cobalt (Co), samarium (Sm), dysprosium (Dy), oxygen (O), argon (Ar) and carbon (C).

ABE	Atomic Beam Epitaxy
BPMR	Bit Patterned Magnetic Recording
CR	Coherent Rotation
CVD	Chemical Vapor Deposition
DW	Domain Wall Nucleation and Propagation
ES	Ehrlich-Schwöbel
fcc	Face-centered cubic
gr	graphene
hcp	Hexagonal close-packed
HWHM	Half Width at Half Maximum
MAE	Magnetic Anisotropy Energy
MBE	Molecular Beam Epitaxy
MOKE	Magneto-Optical Kerr Effect
MRAM	Magnetoresistive Random Access Memory
SOC	Spin Orbit Coupling
STM	Scanning Tunneling Microscope
STT	Spin Transfer Torque
UHV	Ultra High Vacuum





# 1 Introduction

From the beginning of mankind, man has always tried to find ways to store information for processing, developing but also to convey the achieved knowledge to the next generations. From painting on cave walls, engraving to stone and writing with ink, we passed to a different way of storing information by using digital devices. Nowadays, the majority of data is stored in non-volatile memory devices as hard disk drives (HDD), solid state memory cells (like the Flash) and spintronic devices (as magnetoresistive memories). These memory devices were developed during the evolution of computer systems in the last century and are one of the key features as they can retain the stored data when computers are switched off. Moreover, these memories are designed such that data can be accessed and distributed many times faster compared to any previous storing method. The most popular non-volatile device used during the last fifty years, the HDD, uses magnetic media supported on discs to store the information. The areal density of the magnetic media is still increasing these days due to the ever increasing demands of information storage promoted by large data centers, cloud storage services, streaming channels and social networks. Very soon existing technologies will be outdated and new innovations and discoveries must emerge to further increase the areal density and the accessing speeds of the magnetic recording media.

## 1.1 History of Magnetic Disk Drives

Looking back in history, the first commercially available hard drive introduced in 1959 had a capacity of 3.75 megabytes (IBM 350). The storage amount was distributed in fifty disks of 24" diameter with an areal recording density of 0.002 megabits/in<sup>2</sup> [1]! From then, many developments from different fields accelerated the evolution of the magnetic storage media. Implementation of sensors, data controllers, protective surface coatings, error correction algorithms made the devices faster and more reliable, while advances in the reading heads allowed decreasing the average bit size. The first discovery that provided the means to increase the sensitivity of the reading head was the giant magnetoresistance

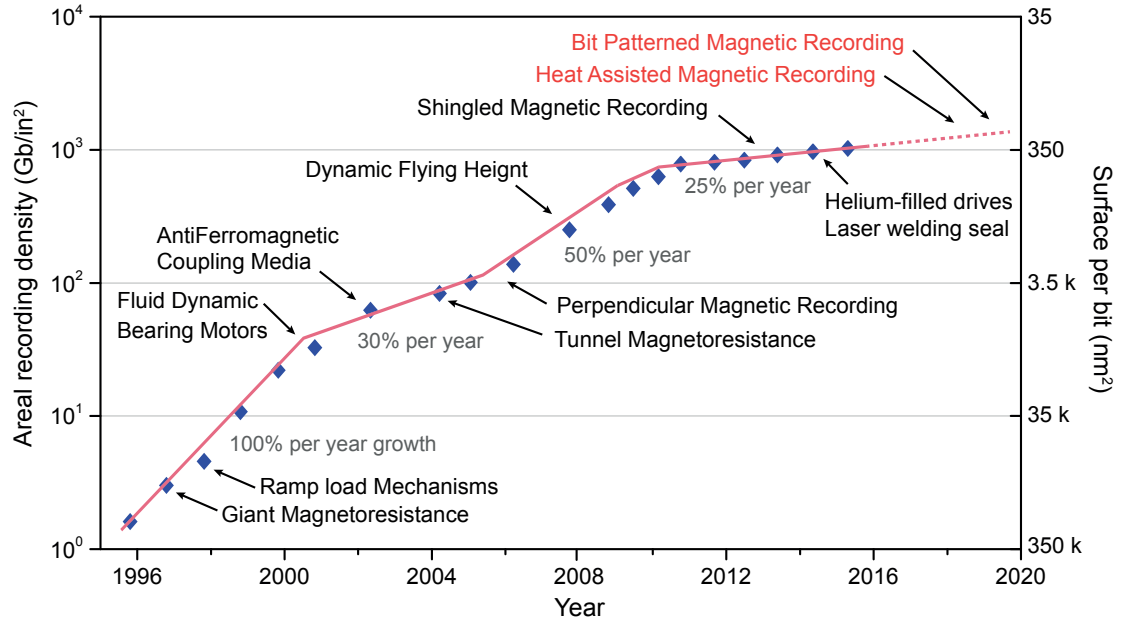


Figure 1.1 – Increase of the areal recording density promoted by recent technological implementations in magnetic recording media, reproduced from Ref. [7, 8].

(GMR) [2, 3]. The signal to noise ratio (SNR) of the readout improved dramatically and thus, it contributed greatly to the increase of the areal density. The second great discovery that found commercial implementation was the tunnel magnetoresistance (TMR). The TMR was operational only at very low temperature [4] in the beginning but in 2004 came the important breakthrough from IBM [5] and Tsukuba [6] researchers, who found very large TMR ratios of 200% at room temperature by employing crystalline MgO as spacer in place of amorphous alumina (see Fig. 1.1 for the impact of these discoveries in the areal density trend). A magnetic head equipped with TMR could detect smaller signals than a GMR and hence, it could read smaller bits.

The reading capabilities of the TMR sensors are such that could detect the signal from bits that were smaller than the minimum size. Hence, the limiting factor for further increasing the areal density shifted from the reading technology to the magnetic media. The bits' magnetization easy axis was in-plane with respect to the surface media. As the bits become smaller, their coercive field reduces and thus, when are packed in a closer arrangement, interference from dipolar interactions would induce instabilities to their magnetic state. To overcome these limitations, the longitudinal recording technology has been replaced by the perpendicular magnetic recording (PMR), where the bits' easy axis is perpendicular to the media plane. The bits aligned in this manner allow minimizing the mutual dipolar interactions and consequently, increasing the number of magnetic elements that can be stored in the same area without cross-talk (see a graphical example in Fig. 1.2). Furthermore, the elements in this arrangement have also the ability to consist of higher coercivity materials. The writing in PMR is more efficient, as the

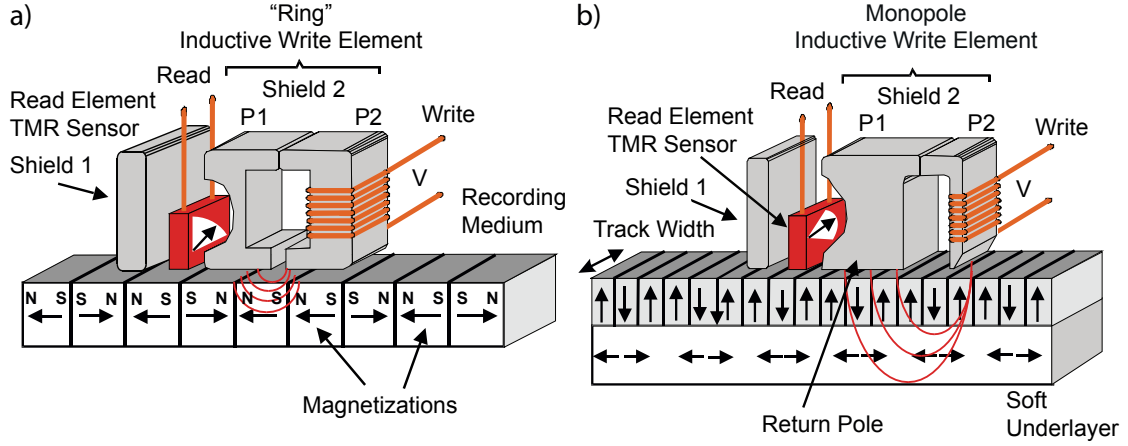


Figure 1.2 – Graphical representation of the increase of areal density by switching from a) longitudinal to b) perpendicular magnetic recording, reproduced from [9].

geometry combined with a magnetically soft underlayer allow larger part of the magnetic field to pass through the bit, hence larger writing fields are possible (see in Fig. 1.2 b). This solution provided a way to increase the onset of magnetic thermal instability, which causes spontaneous magnetic erasure of the medium.

## 1.2 The Current State of The Art in Hard Drives

The magnetic media consist of a magnetic film of nanometric grains mainly made of alloys of Co, Pt and Cr [10] with hexagonal close-packed (hcp) crystalline structure. Currently, the average grain size is about 7 nm in which all spins are ferromagnetically aligned by the exchange interaction such that the total magnetization of the particle can be described as a single macrospin. However, the magnetization direction and the size of the grains are not uniform. These variations are caused by the limitations of the fabrication processes. Due to this drawback the head needs to average over several grains to obtain a satisfactory SNR which defines the size of a bit. Consequently, every bit is made of about one hundred grains and the bit size and shape is determined by the head during the writing process. Commercial storage media must keep their magnetization state stable for at least 10 years. With the continuous grain size miniaturization, the temperature marking the transition between the ferromagnetic to superparamagnetic state (which is called the superparamagnetic limit  $T_b$ ) tends to become smaller than room temperature. Consequently, new materials and reading-writing technologies are needed to implement new storage media devices with increased performances.

From the time the GMR was implemented in commercial products, the areal density of magnetic memories has grown at a rate of almost 100% per year reaching recently values close to 1 Tbit/in<sup>2</sup> [11]. One of the new technologies reaching the 1 Tbit/in<sup>2</sup> limit is the shingled magnetic recording [12] (SMR). In this technology the perpendicular

bit orientation is maintained but the tracks, partially overlap in a staggered fashion which resembles the shingles on a roof. Another recent implemented innovation is the transition from air to helium filled drives. Until now traditional hard drives were not hermetically sealed as the need to equalize the air pressure through a small hole was critical for the optimum operation of the flying head above the magnetic surface. Even though behind this hole there is a filter, the device starts to contaminate after sometime resulting in deterioration of the magnetic surface through friction. Helium unlike air has many benefits as an internal light gas. It has almost six times higher thermal conductivity than air, lowering the temperature of the platters. It reduces the friction and turbulence enabling the platters to be thinner such that a larger number of them can be stacked in the same unit. Hermetically sealing not only ensures the optimal operation of the drive but also creates ideal conditions for higher density configurations.

As the bit miniaturization is an ongoing process, materials with higher coercivity are needed in order to keep the  $T_b$  above room temperature and to prevent mutual interference from neighboring bits. However, the increase of the coercive field makes more problematic the writing process as the head needs to apply higher magnetic fields in order to change the magnetic state. A possible solution to this problem, is the heat assisted magnetic recording (HAMR) technology. HAMR uses a laser beam to heat temporarily the bit area in order to reduce the coercive field and facilitate the change of the bit's magnetic orientation. After that, the rapid subsequent cooling stabilizes the written state. The alloys used in this technology exhibit much higher coercivity to withstand interference as the grains have smaller volume and are placed closer. With HAMR the areal density is expected to reach 10 Tbit/in<sup>2</sup>.

Another proposed technology is the bit patterned magnetic recording (BPMR) [16]. The bits in this technology consist of a single magnetic element (grain or island) which are equally spaced forming a periodic array (see Fig. 1.3 a). The realization of these structures needs a nanofabrication process that guarantees nanoparticles with a narrow size distribution and thus bits with identical magnetic properties. So far great efforts have been made by self-assembly techniques in colloidal nanoparticles [17–19] or with block copolymers [14] (see Fig. 1.3 b). Nevertheless, the uniformity of the particle diameter has an accountable distribution [20–22]. Additionally, when the nanoparticles deposited on a surface their magnetization easy axes are not aligned and thus, reading or writing is not always achieved by using the same field. On the other hand, one can produce with electron beam lithography patterns with a narrow size distribution [23] but this type of process is limited to the research field due to its low speed of fabrication. Great progress has been made during the last decade in magnetic nanopillars and nanodots by using extreme UV lithography process. Size distributions with size variation ( $\sigma$ ) below 6% [24–26] are possible, but with densities limited to about 4.5 Tbit/in<sup>2</sup>, as the size accuracy decreases when the density increases due to the difficulty in fabricating a high-density template during the nanoimprint lithography process [27]. The particle size affects its magnetic anisotropy energy (MAE), which determines the energy barrier

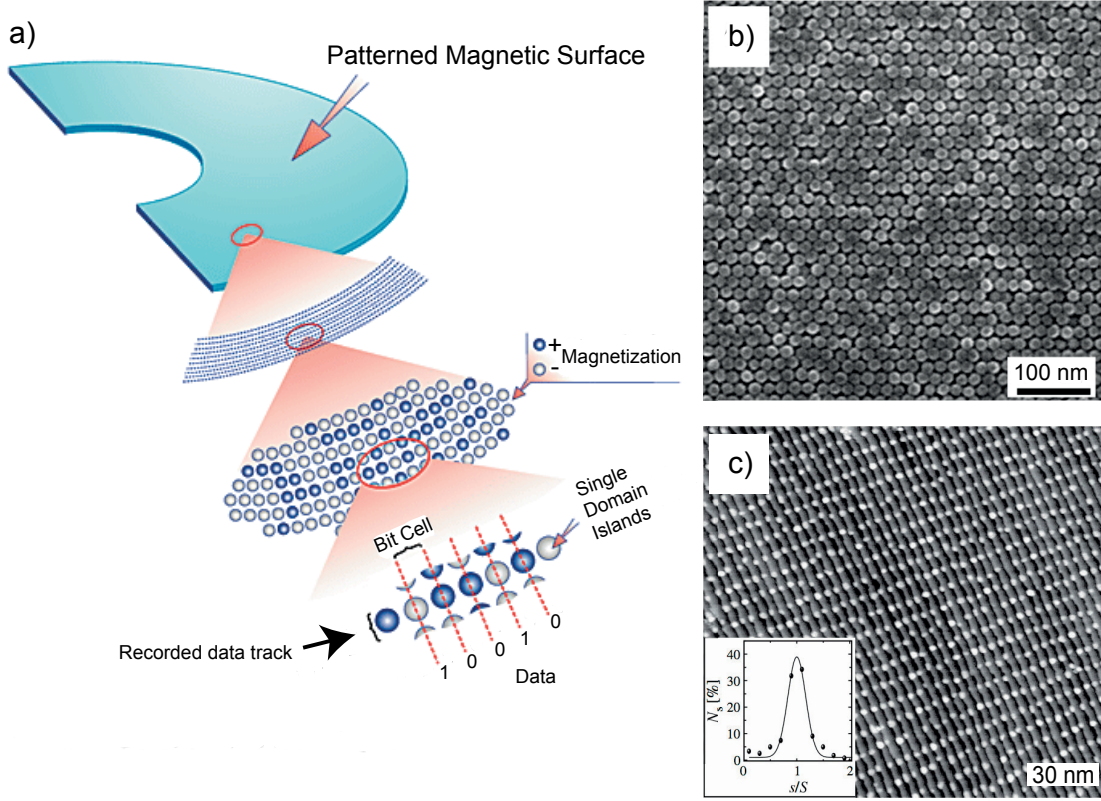


Figure 1.3 – a) Graphical representation of bit patterned recording reproduced from [13], b) scanning electron microscope image of magnetic dots made via block copolymers, areal density of 2 Tbit/in<sup>2</sup> and size distribution at half width at half maximum (HWHM)  $\sim 8\%$  adapted from [14], c) Scanning tunneling microscope image of Co clusters on Au(788) with an areal density of 26 Tbit/in<sup>2</sup>,  $T_b \sim 50$  K and a MAE distribution at HWHM of only 17%, Inset: Size distribution with mean island size  $S = 70$  atoms and HWHM<sub>s</sub> = 20% reproduced from [15].

separating the two stable magnetization states. In most cases, where the MAE scales linearly with the volume of the particle, a 10% difference in radius gives a volume and MAE variation of 30%. This relatively small MAE variation has a great impact on the magnetization lifetime that changes by orders of magnitude. The lifetime of the magnetic state of a single domain grain, in case of a coherent magnetization switching process, is given by the Néel-Brown relaxation law:  $\tau_N = \tau_0 \exp(KV/k_B T)$  where  $\tau_0 \approx 10^{-10}$  s is the attempt time,  $V$  is the particle volume,  $K$  is the magnetic anisotropy constant ( $k_B$  is the Boltzmann constant and  $T$  the temperature). Considering for example a particle ensemble, and assuming that the particle with a size equal to the mean size of the distribution has a lifetime of 10 years, we find for a particle with 30% less MAE a magnetization lifetime of only a few weeks. So far, one of the smallest MAE distribution in ultra dense arrays has been reported for Co nanostructures grown by molecular beam epitaxy (MBE) on Au(788) [15]. These non-interacting monodomain nanostructures have

an ultra high density of 26 Tbit/in<sup>2</sup> and a very narrow MAE distribution at half width at half maximum of 17% (see Fig. 1.3 c). However, despite these remarkable properties, further advances should be made in order to be implemented in a BPMP media, as these structures due to their small size have low magnetization reversal energy barrier resulting in a thermally activated switch of the magnetization at about 50 K.

### 1.3 The State of the Art in MRAMs

The magnetoresistive random access memory (MRAM) is a non-volatile memory technology under development since 1990. In MRAM the data is stored by manipulating magnetic moments instead of electron charges, as used in traditional RAM technologies. The discovery of GMR [2, 3] was the catalyst for the realization of this technology as it uses a non-ferromagnetic spacer between two magnetic elements to decouple their magnetic moments. The magnetic junction comprises a free layer, a spacer, and a "pinned" layer, stacked on top of each other [28]. The free layer made of a soft magnetic material can easily change its magnetization direction under the effect of an external field generated by the Bit and Word lines of the junction, the spacer is made of a conductive non-magnetic element and the pinned layer is made of a combination of a hard magnet and an antiferromagnet in order to keep always its magnetization direction constant. When the magnetization of the free and pinned layer are antiparallel, the spin polarized electrons cannot pass from the pinned to the free layer inducing a high resistance in the circuit, on the contrary when the magnetizations are parallel the spin polarized electrons can pass through the non-ferromagnetic layer to the free layer inducing a very low resistance. This concept is often named as "spin valve" describing one of the most efficient methods to read the magnetization direction of the free layer. Compared to other technologies, MRAM is the only memory that combines unlimited endurance with inherent non-volatility. This combination makes MRAM an ideal technology for always-on low power devices being of the basis of the Internet of Things, sensors, mobile devices and wearable electronics, offering faster operation and longer battery life.

The most advanced version of MRAM today is the spin transfer torque MRAM (STT - MRAM) which uses a magnetic tunnel junction (MTJ) instead of a GMR. The MTJ adopts a MgO(100) thin film as tunnel barrier giving a much higher relative resistance change than GMR. For example, the best GMR junction to date has relative resistance change of 74.8% at room temperature [33] while typical MTJ junctions exhibit over 600% [34]. In STT - MRAM the working principle is completely different than MRAM. Instead of using magnetic fields generated by the Bit-Word lines to manipulate the orientation of the magnetic moment of the cell, the STT - MRAM uses spin polarized currents to change magnetic orientation of the free layer [35]. The interaction between magnetization and a spin-polarized current is attributed to angular momentum exchange between the spins of local magnetic moment and free electrons passing through the MTJ [36]. In antiparallel to parallel switching, electrons flow from the pinned layer to the



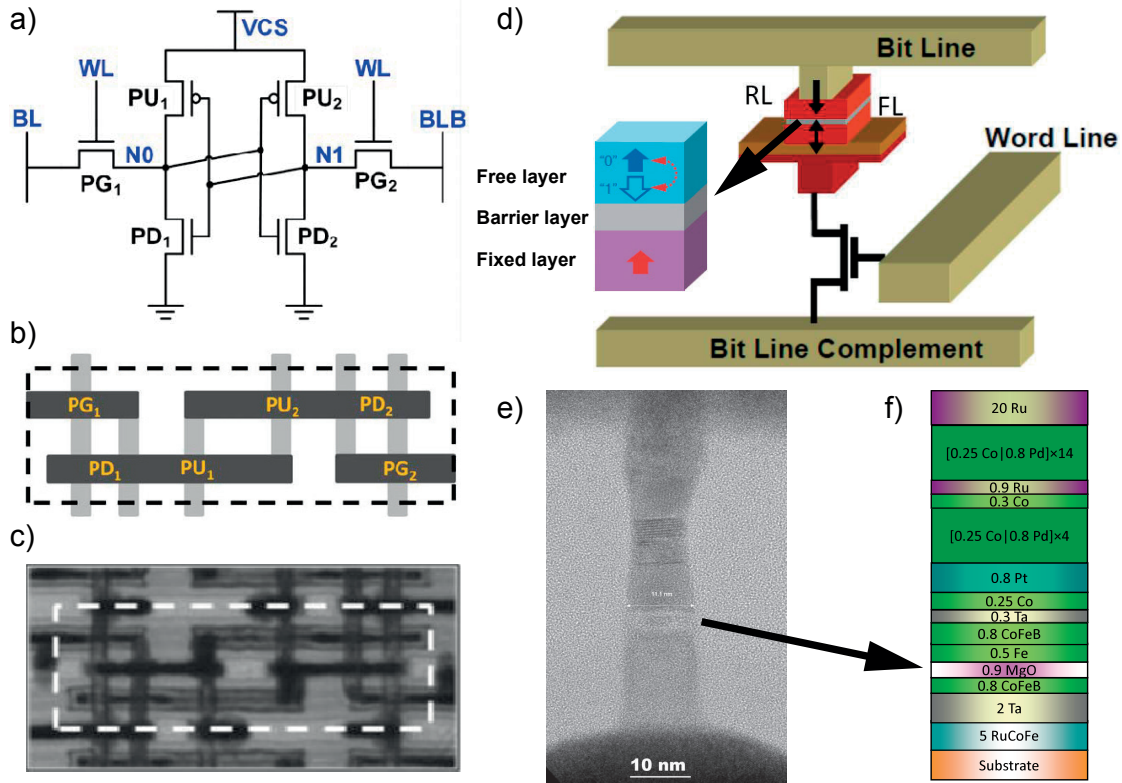


Figure 1.4 – a) Schematic of a 6T SRAM 1-bit cell, the PU and PD transistors in a flip-flop arrangement to retain the bit state and the PG transistors control the read/write operation, b) graphical representation of the MOSFETs, images adapted from [29], c) SEM image of a 6T cell of 14 nm lithographic process, the area inside the dashed rectangle boundary is  $0.058 \mu\text{m}^2$  [30], d) graphic representation of an STT-MRAM cell including the magnetic junction and a MOSFET to control the read/write operation [31], e) transmission electron microscope (TEM) image of an STT junction of 11 nm length, reproduced from [32], f) the element stacking of an STT-MRAM, from [31].

free layer. This spin-polarized current applies spin torque on the magnetization of the free layer, and when the spin-polarized current exceeds the threshold value, the magnetization of the free layer is switched. In parallel to antiparallel switching, electrons flow from the free layer to the pinned layer. After electrons pass through the free layer, the ones with the same spin direction as that of the magnetization in the pinned layer can pass through that layer. On the contrary, the electrons with the opposite spin direction are reflected at the boundary between the MgO barrier and the pinned layer and injected back into the free layer. This current applies a spin transfer torque on the magnetization of the free layer, and when the amount of the spin-polarized current exceeds the threshold value, the magnetization of the free layer is switched. In reading mode, when the moments are antiparallel a maximum resistance is observed since, the electrons cannot pass through the junction while when the moments are parallel the electrons pass through. The reading and the writing of the information takes only several nanoseconds in the state of the art

memories and thus, competes favorably with the other traditional memory rivals [37].

As the STT cells come closer and get smaller due to size scaling, the moments in the free layer are affected by the moments of neighbour cells and a spontaneous reversal can be induced by the cross-talk and the smaller MAE. To minimize this effect the magnetization orientation in the elements of the junction changed to perpendicular direction (with respect to the substrate) thanks to the discovery of perpendicular magnetic anisotropy (PMA) of crystalline MgO-CoFeB ultra-thin film system [38–40]. The PMA technology achieves both higher thermal stability and lower threshold current than those having an in-plane recording scheme with the advantage to scale down to 11 nm lithography process (see Fig. 1.4 e) [32]. The magnetic memories are not only suitable for replacing solid-state non-volatile memories as the Flash memory, but also random access memories (RAMs) as they have similar access times. Until now in conventional computers and most embedded systems the type of RAM used is the static random access memory (SRAM) and the dynamic random access memory (DRAM). SRAM and DRAM are volatile memories which lose the stored information once the power is interrupted. The SRAM is storing the bit state through two inverters in a flip-flop arrangement needing continuous power and the DRAM cell uses one transistor and one capacitor and it needs to be refreshed many times per second to retain the data. The STT - MRAM bit cell uses power only when accessing the information and takes only one sixth of the SRAM cell area (see Fig. 1.4 c), allowing a much denser configuration for central processing unit caches or RAMs where area on silicon is limited and costly. Moreover, MRAM is tolerant to radiation and combined with the extreme low power consumption is the most suitable logic component for future space applications.

### 1.4 Thesis Outline

The increase of the areal density in magnetic recording media is stagnating at the moment. In order to promote storage media of new generation, nanostructures with larger MAE and narrow size distribution should be developed. The origin of magnetic anisotropy must be better understood in nanostructures with reduced size and containing a large fraction of atoms with low coordination. Currently, the best achievement is represented by bit patterned media consisting of arrays of FePt nanodots of L1<sub>0</sub> ordered phase, with an areal density of 5 Tbit/in<sup>2</sup>, exhibit ferromagnetic hysteresis at room temperature with a switching field distribution of 21%. This variation is attributed to the dot size distribution resulting in from the induced damage during the etching process [41]. Particle shape and size variations in sub-20 nm lithography scale are mainly attributed to photoresist materials reaching their intrinsic technological limit [42, 43]. On the contrary, self-assembly techniques, like atomic beam epitaxy (ABE), promote nanoparticle growth with narrow size distribution and shape uniformity, and furthermore, the possibility of long-range periodic ordering [15, 44–55].



This thesis focuses on two principal goals. The first consists in developing a procedure to grow high dense cluster arrays of rare earth on a template by ABE. The growth of highly ordered and monodisperse magnetic nanostructures plays one of the most crucial challenges for increasing the areal bit density of the magnetic recording media. Until now, only transition metal clusters have been organized in such periodic arrays, while rare earth cluster arrays have never been studied before, despite their potential in magnetic applications. The large spin-orbit coupling of the highly localized  $4f$  orbitals can lead to larger magnetic anisotropies compared to the ones observed in  $3d$  metals [56, 57]. For example, magnetic remanence has been recently reported for Er trimers at 3 K [58], while Fe trimers exhibit magnetic bistability only at 0.3 K [59]. It can also open the possibility to grow periodic arrays of  $4f$  -  $3d$  clusters with MAE large enough to retain their magnetic state above room temperature. Here we studied the growth of rare earth clusters on the moiré template formed due to the lattice mismatch between graphene and the Ir(111) surface. We report the first cluster superlattice made of rare earths, namely Sm, grown on graphene/Ir(111). The superlattice forms when Sm is deposited for substrate temperature between 80 K and 110 K. The interparticle distance of 2.53 nm is defined by the moiré period, with a single Sm cluster nucleated per moiré unit cell and it corresponds to an ultra-high density of 115 Tbit/in<sup>2</sup> [60]. The superlattice shows long range order extending over several tens of nanometers and a cluster size distribution competing the finest superlattices grown by ABE.

The second aims at enhancing the MAE of bi- and tri-metallic nanostructures on a single crystal surface via the fine control of their chemistry and crystallographic arrangement by the formation of atomically sharp interfaces and interlines. Nanostructures with reduced coordination exhibit often different magnetic properties from those observed in the bulk [61]. The surface and/or perimeter atoms of particles with reduced coordination interact differently with the surrounding environment compared to the atoms in its volume and thus, contribute differently to MAE. By reducing the particle size, the fraction of the low coordinated atoms with respect to the ones in the volume increases and thus it is crucial to understand these interactions in order to engineer the MAE of small particles [62, 63]. In this sense, the choice of the capping layer is essential not only because it protects the cluster from contamination but also because it alters the cluster's MAE. In this work we focus on surface supported 2D nanostructures having a ferromagnetic core of about 1000 atoms. A previous work on bi-metallic islands on Pt(111) showed an out-of-plane MAE with magnetic remanence at 250 K [63]. The MAE of these nanostructures was engineered by atomically sharp bimetallic interlines and interfaces, using Co as core element, Fe as a surrounding shell and Pd as a capping overlayer. The average size of these nanostructures is approximately 1400 atoms. Synthesized L1<sub>0</sub> CoPt alloy nanoparticles with average size of about 1700 atoms have also demonstrated ferromagnetic behavior above room temperature [64]. Similarly, an earlier study has shown for nanoparticles of the same alloy and an average size of 900 atoms a  $T_b = 280$  K [65]. Therefore, it stands as a challenging task to enhance the MAE of bi- and tri-metallic nanostructures in order

to keep the  $T_b$  above room temperature, while reducing the average size below 1000 atoms. In this part we studied how the MAE of Co islands on Pt(111) can be tuned by decorating and capping the islands with different  $4d$  transitional metals. We report an increased MAE when pure Co islands are capped by Ag, Rh and Pd, with Pd producing the largest variation in  $T_b$ . The lateral decoration of Co edges with all studied elements has been found to reduce the out-of-plane MAE, with Pd producing the smallest decrease in  $T_b$ .

The thesis is structured as follows: In Chap. 2 I give an overview on the theoretical background used in the rest of the thesis. The main subjects explained are i) some insights on nanomagnetism, ii) elements of the nucleation theory shedding light on how the nanostructures are developed, and iii) the growth and properties of graphene (gr) on Ir(111) and its advantages as cluster template. In Chap. 3 the basic concepts regarding the used experimental techniques are given. More specifically, the working principles of the Scanning Tunneling Microscope (STM) and the Magneto-Optical Kerr Effect (MOKE) are presented. In Chap. 4, the home-made Ultra High Vacuum (UHV) chamber used to conduct all the experiments is introduced along with the experimental procedures for sample preparation. In Chap. 5 the nucleation and growth of Sm and Dy clusters on gr/Ir(111) is described. In Chap. 6, the magnetic properties of Co-core  $4d$  transitional metal shell islands are presented, together with the contribution in MAE of multiple Pd layers on Co islands on Pt(111). Chap. 7 is dedicated to the results on nucleation and growth of Rh/Pt(111).

## 2 Basics of nanomagnetism and nanostructure growth by ABE

In this chapter, I introduce the basic concepts of nanomagnetism and nucleation theory. In addition, I review the properties of the graphene grown on Ir(111) used as template for the growth of cluster superlattice.

### 2.1 Nanomagnetism

The magnetic properties of objects at the nanoscale often differ from the ones seen in bulk. These differences arise from two reasons. First, due to reduced coordination which brings higher proportion of atoms on the surface, with respect to the volume. The way the atoms of the surface interact with their surrounding environment differs compared to the volume atoms and hence, their magnetic properties. Second, the size of the objects are comparable to characteristic lengths as the exchange length and the magnetic domain wall width. In the bulk, magnetic domains are separated by domain walls in order to minimize the energy of the system. Below a critical volume, the energy cost to produce a domain wall is greater than the corresponding magnetostatic energy and thus, the nanostructure maintains a single magnetic domain. Single domain ferromagnetic nanoparticles exhibit unstable behavior of the magnetization due to thermal agitation resulting in the phenomenon of superparamagnetism.

#### 2.1.1 Basic Interactions

In the following section the basic interactions that govern the behavior of magnetic systems are shortly described.

### Magnetic Moments

The spin magnetic moment of an atom with a total electron spin  $\vec{S}$  is:

$$\vec{m}_S = -g_S \frac{\vec{S}}{\hbar} \mu_B \quad (2.1)$$

where  $\mu_B$  is the Bohr magneton, which is defined as:

$$\mu_B = \frac{e\hbar}{2m} \quad (2.2)$$

with the elementary charge  $e$ , the reduced Plank constant  $\hbar$  and the electron mass  $m$ .  $g_S$  is the spin Landé factor which equals to 2.002319 [66]. Similarly, the total electron orbital angular momentum  $\vec{L}$  of an atom is related to the orbital moment of:

$$\vec{m}_L = -g_L \frac{\vec{L}}{\hbar} \mu_B \quad (2.3)$$

where the orbital Landé factor equals to 1. An isolated Co atom for example has seven electrons in the  $3d$  level. When applying the Hund's rules, five spins point up and 2 spins point down, resulting in a spin and orbital moment of  $m_S = 3 \mu_B$  and  $m_L = 3 \mu_B$ , respectively.

### Direct Exchange

The origin of the ferromagnetic state is the exchange interaction, originating from the overlapping of the electron orbitals of neighbor atoms. In particular, the exchange interaction is a quantum mechanical effect that arises from the combination of the Coulomb repulsion and the Pauli exclusion principle. The energies of a two-electron system can be expressed by their relative spin orientation, so one can replace the overall Hamiltonian by an effective spin interaction. The extension of this two-spin interaction to multi-electron systems is the Heisenberg model:

$$E_{ex} = - \sum_{i,j} J_{i,j} \hat{S}_i \hat{S}_j \quad (2.4)$$

where  $\hat{S}_i$  and  $\hat{S}_j$  are dimensionless spin operators of the appropriate size or the  $i$ -th and  $j$ -th electrons and  $J_{i,j}$  is the exchange constant between them. The  $J_{i,j}$  will be positive for ferromagnetic materials, where the spins of the corresponding electrons prefer to align parallel to each other and negative for antiferromagnetic materials, where the adjacent spins are aligned antiparallel. The direct exchange interaction is extremely short ranged, for example in monolayer films of Fe, Co and Ni has been found to be limited to the nearest neighbor atoms [67].

### Zeeman Energy

When an external field is applied to a ferromagnetic material, the magnetic moments inside the material tend to align with this external field. The energy term arising from the interaction between the magnetic moments inside the system and the external field is called Zeeman energy and is given as:

$$E_Z = -\mu_0 \vec{M} \cdot \vec{H} \quad (2.5)$$

where  $\vec{H}$  is the applied external field,  $\vec{M}$  is the magnetic moment, and  $\mu_0$  is the vacuum permeability. This energy term contributes only when the external field is present and depends on its strength.

#### 2.1.2 Magnetic Anisotropy

The magnetic anisotropy describes the dependence of the magnetic energy of a material on the direction along which its magnetization is aligned. The most common type of anisotropy is the magnetocrystalline anisotropy, which stems from the spin-orbit interaction of the electrons of a magnetic atom and its environment. The electron orbital moments are linked to the crystallographic structure, and by their interaction with the spins they generate an anisotropic energy landscape that provides favorite spin alignment along well-defined crystallographic axes [68, 69]. The direction along which the spin prefer to align is called “easy axis”, whereas the directions along which the MAE is at the maximum are called “hard axes”. The direction of the magnetization, is determined only by the anisotropy, because the exchange interaction favors the parallel alignment of the magnetic moments, no matter in which direction. When the magnetization aligns along only one preferred direction the anisotropy is called uniaxial which is the simplest case of magnetocrystalline anisotropy. For example, in hexagonal crystals as the *hcp* Co, the anisotropy energy is a function of only one parameter of first order, that is the angle between the magnetization and the *c*-axis. The MAE can be expressed in the form:

$$E = KV \sin^2 \phi \quad (2.6)$$

where  $V$  is the sample volume,  $K$  the anisotropy constant and  $\phi$  the angle between the easy axis and the magnetization, for  $K > 0$ . If  $K$  is negative, the anisotropy energy has a minimum, which corresponds to the plane perpendicular to the magnetocrystalline anisotropy axis. In this case there is a preferable plane known as easy plane in place of a single easy axis. Some special cases of magnetocrystalline anisotropy are the surface or interface anisotropy. The surface anisotropy is attributed to the local breaking of symmetry at surface due to the lower atom coordination, as it was pointed out by Néel [70]. When a magnetic moment is considered in free space, its moment has no preferred direction so it can align perfectly to any external magnetic field. When the same atom belongs to a surface, its *d* orbitals hybridize with the neighboring atoms.

This interaction with the crystal field allows magnetization on specific directions and thus the magnetocrystalline anisotropy rises. Another type of magnetic anisotropy is the shape anisotropy. Shape anisotropy describes how the sample geometry can lead to the existence of preferred directions. The surface divergence of the magnetization gives rise to a demagnetization field which is the origin of the shape anisotropy. The long-range dipolar interactions depend on the relative orientation of the magnetic moments. This causes for example, the magnetic moments to lie within a planar sample or to align along the long axis of a magnetic rod. Shape and magnetocrystalline anisotropy may reinforce each other or compete depending on the system considered.

### 2.1.3 Magnetization Reversal

Magnetization reversal, refers to the process of magnetization inversion from positive magnetic saturation to negative magnetic saturation or vice versa. This occurs either when sweeping an external applied field with sufficient strength in order to align the magnetization uniformly with the field direction or when the thermal energy is large enough that causes the magnetization to reverse randomly. Mainly there are two mechanisms for magnetization reversal: the coherent rotation (CR) and the domain wall nucleation and propagation (DW).

#### Coherent Rotation (Stoner - Wohlfarth Model)

In this model, the magnetic moments of the particle respond simultaneously to the field and thus, the reversal process can be treated as the rotation of a single “macrospin” [71]. In the case of particles with uniaxial anisotropy, the magnetization reversal is described by the Stoner - Wohlfarth model. In presence of an external field  $\vec{H}$  the angular dependence of the total energy is given by  $E_{CR} = KV \sin^2 \phi + \mu_0 MH \cos \theta$ . Two minima exist,  $\theta = 0$  and  $\theta = 180^\circ$ , corresponding to the two opposite directions of the magnetization. In the absence of magnetic field the energy barrier separating these two minima is equal to the MAE,  $KV$  and represents the barrier that must be overcome for thermally magnetization reversal.

#### Domain Wall Nucleation and Propagation

The domain walls developing inside a magnetic material, are the result of the competition among anisotropy, exchange and magnetostatic energy terms. A domain wall mostly nucleates at the edge, but also inside a nanostructure by either an external magnetic field or by large enough thermal fluctuations. Braun has demonstrated that in 1D systems, the lowest energy excitation is an untwisted domain wall pair that, once created, can propagate without any additional energy cost [72]. This indicates that nanostructures promoted with a DW magnetization reversal mode need less magnetic energy to switch

their orientation than the ones of similar size reversing with CR mode. The energy cost of magnetization reversal, with a small external field ( $H < 2K/M$ ), is  $E_{\text{DW}} = 8W_z\sqrt{JK}$ , where  $W_z$  is the cross-section of the particle and  $K$  is the anisotropy energy consisting of the magnetocrystalline and the shape anisotropy..

As the particle length increases, while the other dimensions remain constant, one can estimate a critical length  $l_{cr}$  at which  $E_{\text{DW}} < E_{\text{CR}}$  meaning that the nucleation and propagation of a domain wall becomes energetically favorable. By comparing the expression for  $E_{\text{DW}}$  and  $E_{\text{CR}}$ , one derives  $l_{cr} = 4\sqrt{J/K}$ . For example oblong Fe islands on Mo(110) with sizes between 250 and 450 atoms have been reported to switch faster than the circular ones [73]. This is attributed to the reversal mechanism by DW vs CR. The critical island length in this study was found  $l_{cr} = (9.1 \pm 0.3)$  nm. A similar critical length was also measured recently in a study of the magnetization reversal of compact and ramified Co islands [74]. The critical length between the two types of islands sets at  $(9 \pm 2)$  nm for island average size of 600 atoms, in excellent agreement with the aforementioned expression and the previous study. Another recent study of trigonal Co bilayer islands on Cu(111) by the means of spin-polarized STM finds an island crossover size between the two reversal mechanisms [75]. More specifically, the islands reverse by CR mechanism for sizes up to 7500 atoms and from there the magnetization reversal switches by DW.

### 2.1.4 Superparamagnetism

Let us consider an ensemble of single-domain nanoparticles with uniaxial magnetic anisotropy. The smaller the nanoparticles are, the stronger the influence of the thermal energy on them is. Since the ratio of surface to bulk atoms increases, surface contribution to magnetization becomes significant and the magnetization of nanoparticles is dominated by finite size and surface effects [76]. If the thermal energy is lower than the anisotropy energy, magnetization is fixed along the easy axis and the nanoparticles are thermally-blocked in one of the two minima. When the thermal energy of the particles becomes comparable to the anisotropy energy then the magnetization direction can be easily switched by a small external field, indicating the onset of the superparamagnetic state. In this state, each nanoparticle behaves like a paramagnet with the exception that their magnetic susceptibility is much larger because all the atomic moments in the nanoparticle behave coherently as a giant magnetic moment (macrospin).

In zero-field, at a certain temperature, after setting a magnetic state, the net magnetization of a particle ensemble bears an exponential decay over time, which is called magnetic relaxation. Hence, the maximum time a magnetic state remains constant between two measurements is called Néel relaxation time which comes from the Néel-Brown model [77, 78] and offers a probabilistic description for thermally activated stochastic

events:

$$\tau_N = \tau_0 \exp\left(\frac{E_b}{k_B T}\right) \quad (2.7)$$

where  $\tau_0 \approx 10^{-10}$  s and  $E_b$  the barrier energy. The observed magnetic behavior depends on the measured time  $\tau_m$ . If  $\tau_m > \tau_N$  the macrospin will flip several times during the measurement so that the net magnetization averages to zero (superparamagnetic regime). If  $\tau_m < \tau_N$  each macrospin stays in its initial configuration during the measurement (blocked regime). The transition between the blocked state to the superparamagnetic state occurs as a function of temperature. The temperature at which  $\tau_m \approx \tau_N$  is called the blocking temperature  $T_b$ . It is straightforward to say that because of the anisotropy energy ( $E_b = KV$ ) one needs materials with higher magnetic anisotropy to fabricate smaller nanostructures for HDD or non-volatile magnetic memories that can achieve a  $T_b$  higher than room temperature and a magnetization lifetime longer than the 10-year standard. The  $T_b$  of an ensemble of nanoparticles can be found by measuring the zero-field

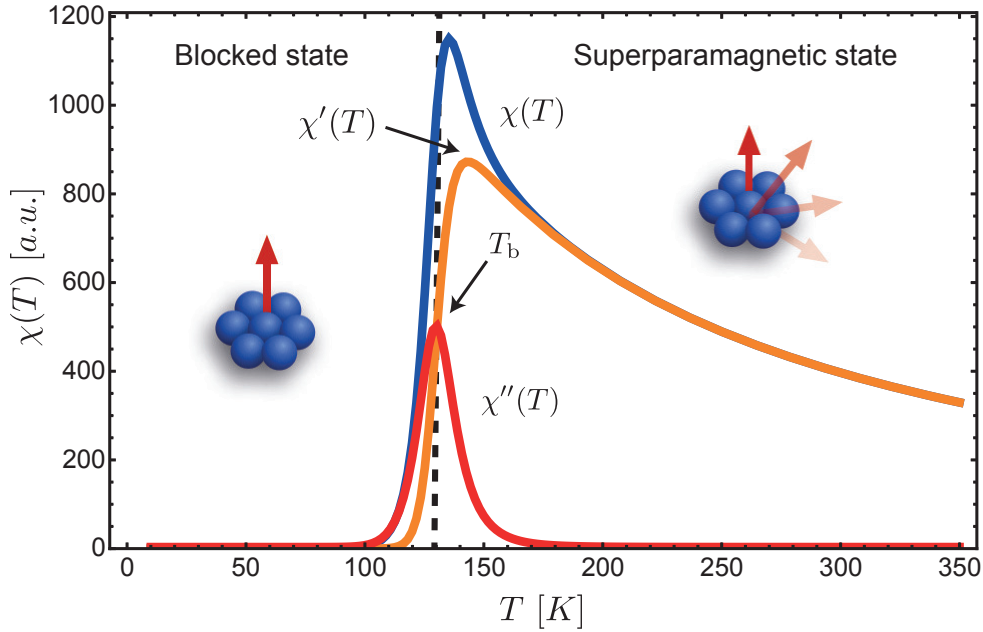


Figure 2.1 – Zero-field susceptibility for a particle with uniaxial anisotropy.  $\chi(T)$  and the two components  $\chi'(T)$  and  $\chi''(T)$  are shown in blue, orange and red, respectively. The  $T_b \approx 130$  K is indicating the transition between the superparamagnetic state and the blocked state.  $E_b = 233$  meV,  $M = 930$  atoms  $\times \mu_B$  and a triangular sweeping field of 10 mT at  $\nu = 9$  Hz is applied.

AC susceptibility with an experimental setup as MOKE (see Chapter 3). The zero-field AC susceptibility  $\chi(T) = \chi'(T) + i\chi''(T)$  consists of two parts, the in-phase part (the



real part  $\chi'(T)$ ) and the out-of-phase part (the imaginary part  $\chi''(T)$ ) where:

$$\chi'(T) = \chi_{eq}(T) \frac{1}{1 + \omega^2 \tau_N^2} \quad (2.8)$$

$$\chi''(T) = \chi_{eq}(T) \frac{\omega \tau}{1 + \omega^2 \tau_N^2} \quad (2.9)$$

and  $\chi_{eq}(T)$  is the static or the zero-field susceptibility component at thermodynamic equilibrium [79, 80]:

$$\chi_{eq}(T) = M^2 \left[ \frac{\exp(E_b/k_B T)}{\sqrt{\pi E_b k_B T} \operatorname{Erfi} \sqrt{(E_b/k_B T)}} - \frac{1}{2E_b} \right] \quad (2.10)$$

where  $\operatorname{Erfi}$  is the imaginary error function described as  $\operatorname{Erfi}(x) = \frac{2}{\sqrt{\pi}} \int_0^x e^{t^2} dt$ .

In the AC susceptibility, the real component is the slope of the  $M(H)$  curve acquired by a DC susceptibility measurement and the imaginary component arises from the dissipative processes in the sample that induce a delay in the measurement, as the transition of a magnetic moment from the easy axis to the hard axis.  $\chi(T)$  and the two components  $\chi'(T)$  and  $\chi''(T)$  are represented in Fig. 2.1 for an ensemble of monodisperse particles with uniaxial anisotropy. The right-hand side of  $\chi'(T)$  after the peak and also the  $\chi_{eq}(T)$  (not shown) decay with a rate proportional to  $1/T$ . As the temperature increases, the magnetization of the macrospin becomes more erratic due to the larger thermal fluctuations and thus it is less sensitive to the aligning force generated by the field.  $T_b$  is defined as the temperature at which the peak in  $\chi''(T)$  occurs.

Usually susceptibility experiments deal with ensembles of magnetic nanoparticles with a certain size distribution. Particles with different size have different MAE and consequently the nanoparticle size distribution induces a magnetic energy barrier distribution for magnetization reversal. The larger the particle, the larger is the magnetic moments and the magnetic anisotropy. As the AC susceptibility is sensitive to the square of the magnetization (see eq. 2.10), the larger particles with higher anisotropy are those which contribute the most to the overall signal. For this reason the signal acquired from an ensemble of non-interacting particles gives a wider peak in  $\chi''(T)$  and a decay which diverges from  $1/T$  in  $\chi_{eq}(T)$ . When interparticle interactions play an important role in the ensemble the curve of  $\chi''(T)$  becomes asymmetric and wider and the  $\chi_{eq}(T)$  decays slower than the  $1/T$  at higher temperatures [81].

## 2.2 Nucleation and Growth

Submonolayer deposition for thin film growth is used in fundamental research but also increasingly in technological applications, as in microelectronics. When the deposition is realized on a crystalline substrate it is called epitaxial growth. The word comes from two connected Greek words where *epi* means on or upon and *taxis* means spatial arrangement (in Ancient Greek: ἐπί + τάξις = ἐπίταξις). If the adsorbed atoms and the supporting substrate are of the same material the process is called homoepitaxy while if they are different, the process is called heteroepitaxy. By principle, atoms are deposited from gas phase on a substrate with a flux  $F$  which determines the monolayer per second rate (with rates mostly between  $10^{-4}$  to  $10^{-1}$  ML/s). A monolayer is defined as one atom of the deposited species for substrate unit cell. For realizing a clean deposition process, UHV conditions are needed (pressure  $< 10^{-10}$  mbar) in order to prevent the atoms to chemically interact with molecules from the residual gas both during their path towards the surface and during the diffusion on the surface. UHV conditions are needed also in our experiments in order to prevent the magnetic nanostructures to alter their magnetic properties by residual gases during measurements.

### 2.2.1 Processes in Epitaxial Growth

Several competing processes are realized simultaneously during atom deposition in epitaxial growth. The outcome of this competition depends on intrinsic factors of the system as the surface symmetry, the nature of substrate and deposited atoms and on extrinsic factors as the sample temperature and the deposition flux. The morphology of self assembled nanostructures can be completely different from the ones obtained by thermodynamic equilibrium conditions. After landing, the adatom instantaneously thermalize to the substrate temperature and starts diffusing randomly along the surface (terrace diffusion). The adatom, to diffuse on the terrace needs to overcome the energy migration barrier ( $E_m$ ) separating adjacent sites. Atoms in their random walk on the terrace, may encounter another diffusing monomer to form a dimer or a step edge or a preexisting island and incorporate. Other general processes are the realization of an interlayer jump and the diffusion along an edge. These elementary processes in epitaxial growth are characterized by proper energy barriers and thus get activated at different substrate temperatures. As an example, the cluster dissociation. At high temperature the atoms detach from islands and diffuse on the adjacent area and re-condense either to the same island or to a neighbor one. In Ostwald ripening, smaller clusters are more prone to dissociate due to larger perimeter to surface ratio, and as a consequence, smaller islands dissociate earlier in favor of the larger ones. If in a specific system, the dissociation barrier is lower than the diffusion barrier for dimers, they are expected to break and migrate to other stable islands. In Fig. 2.2 are represented examples of the most important elementary processes.

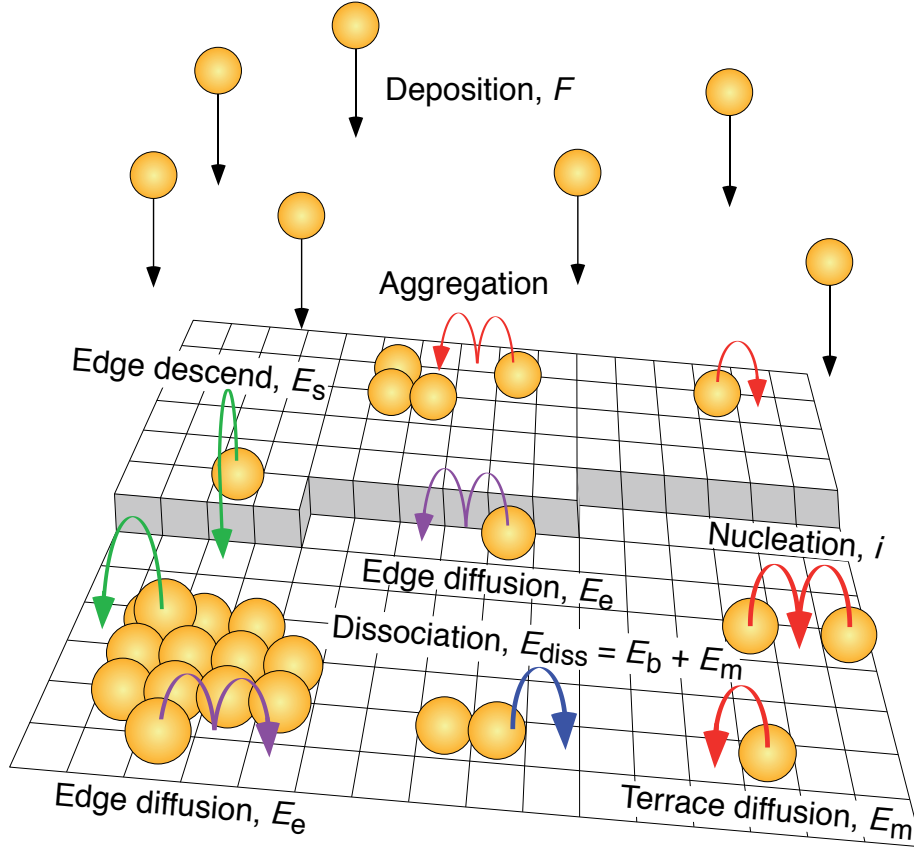


Figure 2.2 – Graphical representation of atomic elementary processes during epitaxial nanostructure growth [82].

When an atom lands directly on an existing island it can descend only if it has sufficient energy to overcome an extra barrier in addition to  $E_m$ . This barrier is called the Ehrlich-Schwöbel barrier (ES),  $E_s$  [83, 84]. The ES barrier is also responsible for the wedding cake morphology which occurs usually in low temperature epitaxial growth as it suppresses completely the interlayer transport and consequently, nucleation on the second layer occurs well before the first layer is completed. The repetition of this process for subsequent layers gives rise to wedding-cake island morphology. The differences in coverages between two subsequent layers are described by the Poisson distribution [85].

### 2.2.2 Rate Equations and Scaling Laws

Upon deposition, the adsorbed atoms (or adatoms), start diffusing randomly on the surface via a hopping motion between neighboring adsorption sites with a hopping frequency  $\nu$ . The hopping frequency is described by the Boltzmann statistics with the

following equation:

$$\nu = \nu_0 \exp\left(\frac{-E}{k_B T}\right) \quad (2.11)$$

where  $E$  is the diffusion energy barrier,  $\nu_0$  is the attempt frequency prefactor, typically being in the range of the Debye frequencies of  $10^{12} - 10^{13}$  Hz,  $k_B$  is the Boltzmann constant and  $T$  the substrate temperature. An adatom during random walk may encounter another atom and form a dimer, which can be immobile or mobile with a different energy barrier, or could meet and attach to a preexisting island. One can define a critical cluster size  $i$ , which refers to the island size in atoms that becomes immobile upon incorporation of one additional adatom. In the mean-field nucleation theory, a computational method used to simulate the above processes is the mean-field approximation. In this approximation, the exact location of the atoms on the surface is replaced by the average effect on the system, without taking into account the stochastic mechanism of the growth process. The mean-field approximation which explains quite accurately the growth in our experimental results, is the one developed by Zinsmeister [86, 87] and Venables [88]. The differential equations in this model describe the time evolution of mean-field quantities such as the island densities  $n_s$  of clusters with size  $s$ . The density of monomers and stable islands can be expressed by the following equations:

$$\frac{dn_1}{dt} = F - 2\sigma_1 D n_1^2 - \sigma_x D n_1 n_x \quad (2.12)$$

$$\frac{dn_x}{dt} = \sigma_1 D n_1^2 \quad (2.13)$$

where  $F$  is the deposition flux and  $D$  is the adatom diffusion coefficient describing the mean square displacement of the adatom per unit time,  $n_x$  is the stable island density,  $\sigma_1$  the capture efficiency of a monomer to merge with another monomer and  $\sigma_x$  the capture efficiency of a monomer to incorporate to a stable island. The adatom diffusion can be written in terms of the hopping frequency  $\nu$  via the Einstein relation [89]:

$$D = \frac{1}{4} \nu \alpha^2 = \frac{1}{4} \nu_0 \exp\left(\frac{-E}{k_B T}\right) \alpha^2 = D_0 \exp\left(\frac{-E}{k_B T}\right) \alpha^2 \quad (2.14)$$

where  $\alpha$  is the lattice constant of the crystal surface and  $D_0 = \frac{1}{4} \nu_0$  with  $\frac{1}{4}$  valid for 2D diffusion on a square lattice. The terms on the right hand side of equation 2.12 describe the increase or decrease of monomer density. The first term is the deposition flux, the second term describes the monomer decrease due to the merging with another monomer into a stable dimer and the third one describes the decrease due to the loss of monomers which attach to stable islands. The number of monomers which land directly on the stable islands is neglected in this model. The equation 2.13 describes the growth rate of stable islands formed by the binding of two monomers to form a dimer. This simplified

approach can be extended to include critical cluster sizes greater than  $i=1$ , so other temperature regimes can be studied, where dimers, trimer etc are not stable. This leads to one general equation, describing the steady state regime of stable islands with density  $n_x$ :

$$n_x = \eta(\Theta, i) \left(\frac{D}{F}\right)^{-\chi} \exp\left(\frac{-E_i}{k_B T(i+2)}\right) \quad (2.15)$$

where  $\chi = i/(i+2)$  is the scaling exponent and  $E_i$  describes the binding energy of the critical cluster size. For  $i = 1$  ( $E_1 = 0$ ) the equation 2.15 reduces to  $n_x = \eta(\Theta, 1) (D/F)^{-1/3}$ . The factor  $\eta$  is slowly varying with the coverage as  $\eta \propto \Theta^{1/(i+2)}$  and thus, it can be found by approximation at  $\eta = 0.25$  in Fig.6c of Ref. [90] for island coverages in the saturation regime, as we see next.

### 2.2.3 Growth Regimes

In nonequilibrium crystal growth some different regimes are identified as a function of the coverage. The simplest case, is represented by the monomers mobile and the dimers stable and immobile ( $i = 1$ ). In the beginning of the deposition, the adatoms land with a rate  $F$  and diffuse on the surface with a rate  $D$ , until they meet another diffusing atom and nucleate (form a dimer). As the deposition continues, the number of dimers increases almost linearly until it reaches a density  $n_2$  similar to  $n_1$  [91]. From that point on, the probability for a new adatom to reach another monomer or an existing cluster becomes comparable and therefore, the cluster growth begins to compete with the nucleation of new ones. As a result, the density of stable clusters increases until it saturates to a coverage of  $\Theta_{sat} \approx 0.15$  ML. This threshold is called the irreversible growth regime as all formed islands are stable and immobile. At the onset of this saturation regime the mean-free path of the diffusing atoms is equal to the mean island interdistance and thus, all adatoms reaching the surface, will diffuse and attach to a stable island. This regime extends up to the point the islands grow enough to touch, at typically  $\Theta_{sat} \approx 0.35$  ML, where coalescence begins. Islands continue to extend until a film percolates at about  $\Theta = 0.55$  ML. These typical values for  $\Theta$  depend on the  $D/F$  ratio (see Fig. 2.3 a) and partially also on the island shape. For scaling regimes  $D/F \leq 10^5$  the monomers diffuse too slowly to reach each other during deposition but they continue to diffuse after the deposition stops until they nucleate. For low temperatures where the monomers are stable nuclei ( $i = 0$ ) the process cannot be described by the eq. 2.15, and the density  $n_x$  becomes independent of deposition temperature.

### 2.2.4 Island Shapes

The stable islands on hexagonal close-packed substrates have two prominent shapes: fractal and compact. The simplest case for fractal island formation is when atoms diffuse

to the cluster edge and stop upon attachment forming diffusion-limited aggregation (DLA) islands [92]. This leads to monoatomic-wide branches that extend in random directions. As the edge diffusion sets in, ramification occurs and thicker branches are formed. As the deposition proceeds, if the edge diffusion is low enough, an atom slowly diffusing along the island edges can be stopped by incorporation of another diffusing monomer and a new branch starts. This limited edge diffusion when increases causes dendritic shaped islands which follow a specific orientation of the substrate. Dendrites have trigonal symmetry and their branches are at least two to three atoms wide, an example is shown in Fig. 2.3 b. With increasing the temperature, the corner diffusion becomes activated, enabling the adatoms to migrate from a onefold to a twofold coordinated site (from a corner site to an edge site).

Once corner crossing is enabled, compact islands grow, with a preferred growth direction due to asymmetrical diffusion across the island edges [93, 94]. This can be explained by the two different microfacets of the hexagonal substrate that the islands are bound. The two distinguished facets are: the closed packed  $\{111\}$ -faceted B steps and the more open  $\{100\}$ -faceted A steps which have an orientation difference of  $60^\circ$ . The hcp sites in A steps are in the right distance from the corner but in the B steps there is either an on-top site or the hcp site sits much closer than it should to the island edge. The diffusion realized from a corner favors the migration to an A step as it has a barrier close to  $E_m$ , whereas the crossing to a B step costs five times more energy. This mechanism is already verified by effective medium theory [95, 96] and also explains why in some systems dendrite branches grow wider before turning into compact islands [97]. At higher depositing temperatures the corner diffusion anisotropy is found to be responsible for the shape orientation of compact islands [98].

### 2.2.5 Island Size Distribution

In submonolayer epitaxial growth atoms are deposited onto a substrate where they diffuse, aggregate and form a distribution of different island sizes. The island size distribution is an essential tool in nucleation theory, because its shape identifies the critical cluster size of the system (see Fig. 2.4 a). For  $i = 0$  ( $D/F \leq 10^5$ ) the size distribution is expressed by a linear decay with increasing the island size, as the immobile monomers dominate the cluster population. For the scaling regime  $10^5 \leq D/F \leq 10^9$  and  $i \geq 1$ , the island size distribution  $N_s(\Theta)$  for a coverage  $\Theta$  can be described by the following scaling form [100–103]:

$$N_s(\Theta) = \frac{\Theta}{S(\Theta)} f_i\left(\frac{s}{S(\Theta)}\right) \quad (2.16)$$

where  $N_s(\Theta)$  is the number of island with size  $s$ ,  $S(\Theta)$  is the average island size and the scaling function  $f_i(u)$  satisfies the normalization condition:  $\int_0^\infty f_i(u) du = \int_0^\infty u f_i(u) du = 1$ . Amar and Family [104] proposed an analytic expression for the scaled island size

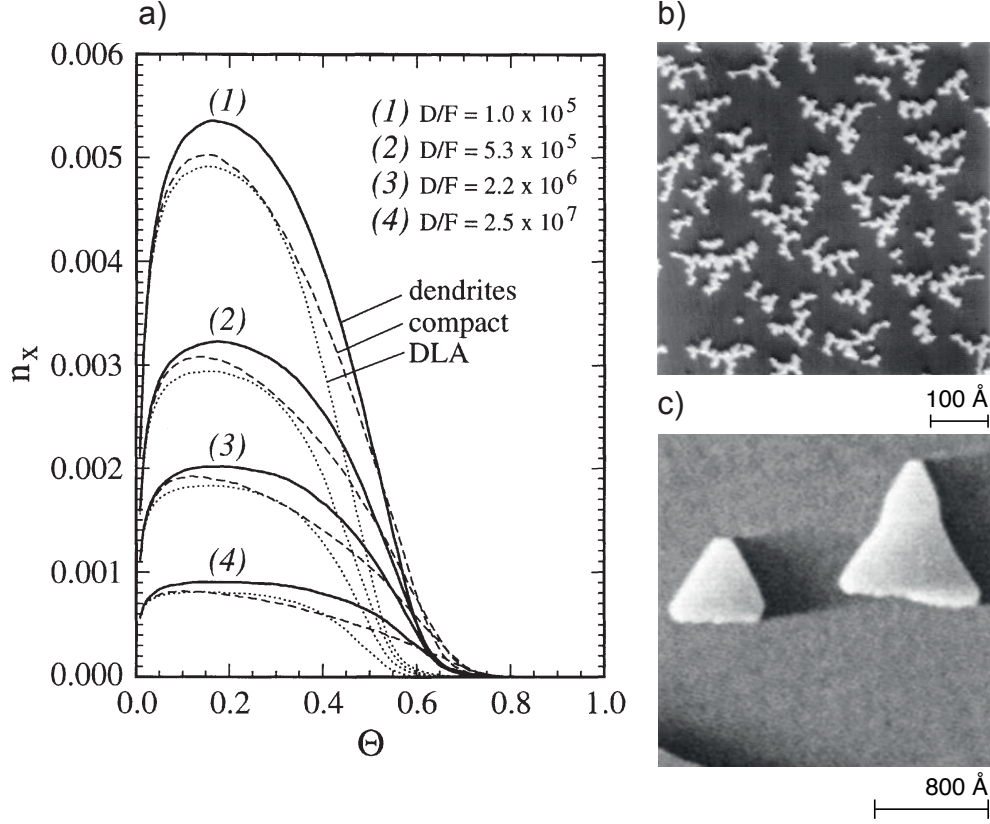


Figure 2.3 – a) Kinetic Monte Carlo simulations for three island shapes that can be realized on hexagonal lattices for four different  $D/F$  rates, adapted from [91]. b) Dendritic shaped islands for Pt/Pt(111) homoepitaxy at 180 K ( $\Theta = 0.094$  ML), from [94]. c) Trigonal compact islands of homoepitaxy on Pt(111) after deposition at  $T_{\text{dep}} = 640$  K,  $F = 1 \times 10^{-2}$  ML/s,  $\Theta = 0.15$  ML, adapted from [99].

distribution as a function of the critical cluster size. The quantitative formula proposed,  $f_i(u) = C_i u^i \exp(-i a_i u^{1/a_i})$  with  $C_i$  and  $a_i$  deriving from normalization parameters so to maximize at  $u = 1$ , was able to determine the theoretical transition temperature for the change in the critical island size which verified later in the cases in experiments on Fe/Fe(100) [105], Fe/Cu(100) [106] and Ag/Pt(111) [107].

Scaled island size distributions are sensitive tools to detect 2D Ostwald ripening from dimer and in general from cluster dissociation. While working outside the regime of irreversible growth (e.g.  $i = 1$ ) in thermal annealing experiments, the nucleation density can be affected either by dimer diffusion or by dimer dissociation. In most surfaces with hexagonal symmetry, dimers prefer first to diffuse than to dissociate, therefore, dimer diffusion is not foreseen to change the island density scaling before dimer dissociation [109]. On the other hand, when dimer dissociation occurs [108], a sharp transition is observed in the scaled island size distribution as exemplified in Fig. 2.4.



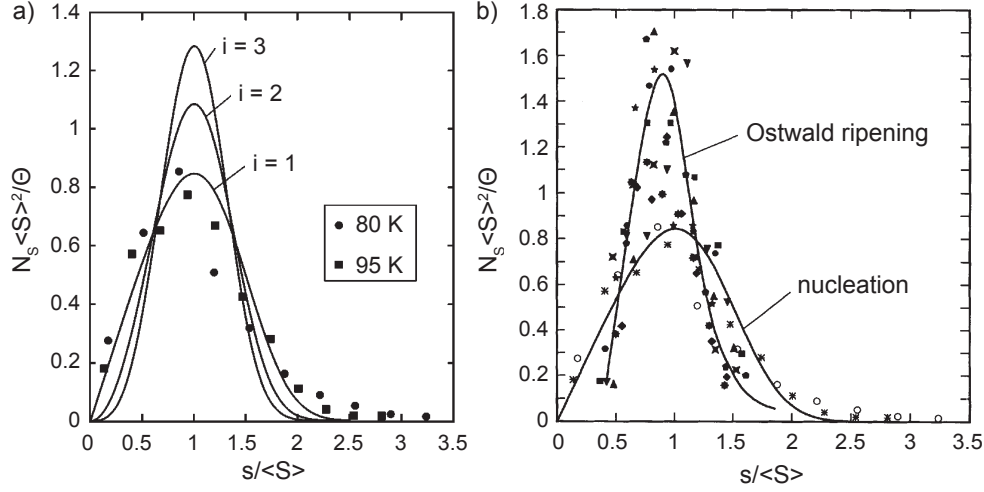


Figure 2.4 – a) Scaled island size distribution for 0.12 ML Ag/Pt(111) [107] (circles and squares) in comparison with the theoretical curves developed by Amar and Family for  $i = 1, 2, 3$  [104]. b) The onset of Ostwald ripening is marked by a sharp transition of constant ( $i = 1$ ) to exponentially increasing island sizes as a function of annealing temperature, from [108].

## 2.3 Graphene

Graphene (gr) is a planar monolayer structure of carbon atoms arranged into a two-dimensional honeycomb lattice, with a lattice constant of  $\alpha_{gr} = 2.46 \text{ \AA}$  (see Fig. 2.5 a). gr can be found in graphite as the periodic stacking layer, it has a high crystallographic quality and it is stable under ambient conditions. It was isolated for the first time in 2004 [110] and since then it has attracted a tremendous interest in many fields due to its exceptional electrical [110, 111], thermal [112] and mechanical properties [113]. gr can be obtained by exfoliation from graphite flat surfaces (also called “Scotch tape” or “Peel-off” method) yielding only micrometer-sized flakes. It can be made also by thermal annealing of SiC, or hydrocarbon decomposition on polycrystalline copper foils and on single-crystall surfaces as, in our case, gr/Ir(111) [114] producing high quality millimeter-sized films.

The exotic properties of gr are exploited already in a large variety of applications. With physical and/or chemical modification, gr is capable of detecting many types of molecules and ions realizing ultra sensitive chemical and bio-sensors [115–119]. Moreover, its intrinsic low electrical noise is very promising to achieve ultra low detection limits up to a few molecules [120, 121]. Due to its sound mechanical properties gr it can be converted as a multi-application strain sensor with a wide range of stretchability and sensitivity compared to existing metallic or semiconductive microdevices [122]. For example as in the cases of wearable strain sensor cabs which detect human body gestures and small



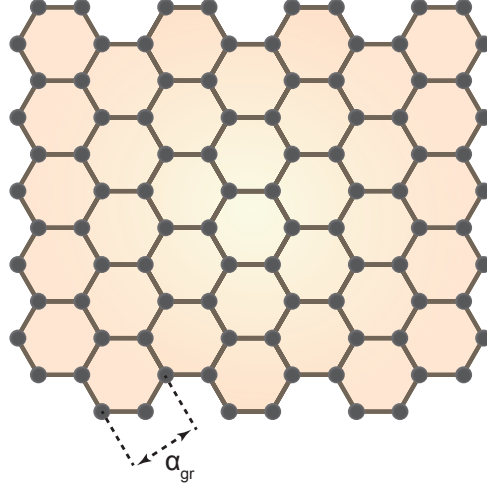


Figure 2.5 – Crystal structure of gr, the lattice constant is  $\alpha_{\text{gr}} = 2.46 \text{ \AA}$ .

scale motions like breathing and speaking [123]. Finally, gr is a promising candidate for spintronic devices by functionalizing a single magnetic molecule on its surface in order to detect electrically the magnetization reversal of other molecules in its proximity [124].

### 2.3.1 Growth and Structure of Graphene on Ir(111)

Epitaxial gr layer on Ir(111) can be prepared by chemical vapor deposition (CVD) of hydrocarbon gas directly on its surface. In the CVD method, mainly ethylene is used (also heavier molecules as benzene, toluene and cyclohexane give equivalent results) which is either adsorbed by exposing the surface at room temperature and subsequently annealing at high temperatures to decompose the molecules to desorb the hydrogen, or by directly exposing the surface at high temperature. In the former case, which is called temperature programmed growth (TPG), graphene starts to grow from small flakes on the surface and about four cycles are needed for the layer to be completed [45]. In the latter case, carbon precursors are adsorbed until the layer is assembled. In both cases the growth is self-limiting and only a single graphene layer forms at the end of the process. This saturation behavior can be understood from the fact that the process, requires the chemical reactivity of the metal surface, while it is inhibited once a single layer of gr is completed due to its much lower reactivity and solubility of C inside the surface.

The binding distance between the gr and Ir surface is  $3.77 \text{ \AA}$  [45] indicating a physisorbed binding character. The dominant interactions between the C atoms and the substrate are the van der Waals. Upon growth, gr forms large isotropical films like a carpet-growth over the atomic steps. Depending on the growth temperature, several domains with specific orientation appear. The preferred domain aligns the rows of densely packed carbon atoms with the densely packed rows of the Ir(111) underlying surface, referred in

literature as  $R0^\circ$  [125, 126]. Except this domain, also others exist with rotational angles of  $R30^\circ$ ,  $R18.5^\circ$  and  $R14^\circ$  [127]. Note that the domain boundaries of the misoriented graphene domains are not determined by the atomic steps, but run across the steps. The domains are separated by boundaries with small angle misorientations, which consist of edge dislocations of pairs of pentagons and heptagons. For growth temperatures below 1200 K gr is highly disordered, at 1350 K randomly oriented domains are produced, with dominant the  $R30^\circ$  [128]. At 1400 K only single  $R0^\circ$  domains are formed, giving the most uniform film yet reported [129].

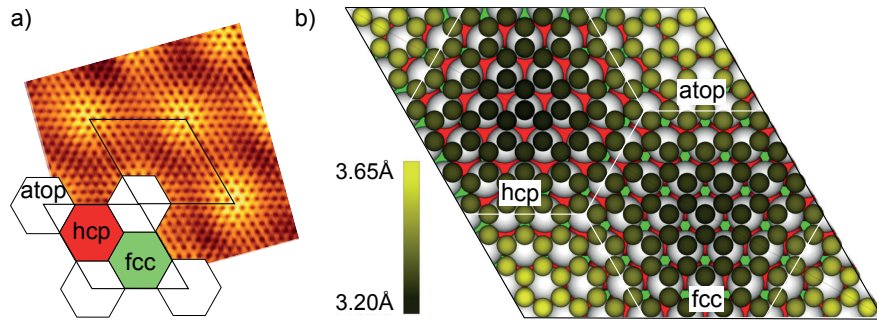


Figure 2.6 – a) STM topography of gr/Ir(111), image size is  $6 \times 6$  nm,  $V_t = 1$  V,  $I_t = 7$  nA. The drawing indicates the different areas within the moiré structure (atop, hcp, fcc), image adapted from [130]. b) Graphical representation of the moiré cell from van der Waals - Density Function Theory calculations, representation adapted from [131].

The gr moiré mesh on Ir(111) consists of  $(10.32 \times 10.32)$  gr unit cells over  $(9.32 \times 9.32)$  iridium sites giving a periodicity of 2.53 nm [125]. Three high symmetry subconfigurations in the moiré mesh are identified, namely the fcc, the hpc, and the atop characterized by a different stacking of the C atoms with respect to the iridium surface sites (see Fig. 2.6). In the fcc region the center of the C honeycomb ring is located over an iridium face-centered cubic (fcc) site, whereas in the hexagonal close-packed (hcp) the center of the honeycomb is above an hcp site located in the second iridium layer. In contrast, in the atop region, an iridium atom lies below the center of the C ring. The combination of this extreme uniformity of the moiré structure with the great homogeneity of the gr layer over Ir surface, offers an ideal template for cluster superlattice growth by self-assembly.

### 2.3.2 Graphene on Ir(111) as Template for Cluster Superlattice Growth

Clusters due to their reduced size, often show different properties from the bulk [61]. Cluster superlattices are very useful for the study of these properties as they provide equal interdistances and area for each cluster, and frequently narrow size distribution. In such cluster arrays, one can study either the properties of each cluster individually i.e. for magnetic storage media or collectively as in model catalysis.

The gr/Ir(111) moiré template is already one of the well studied systems to date with

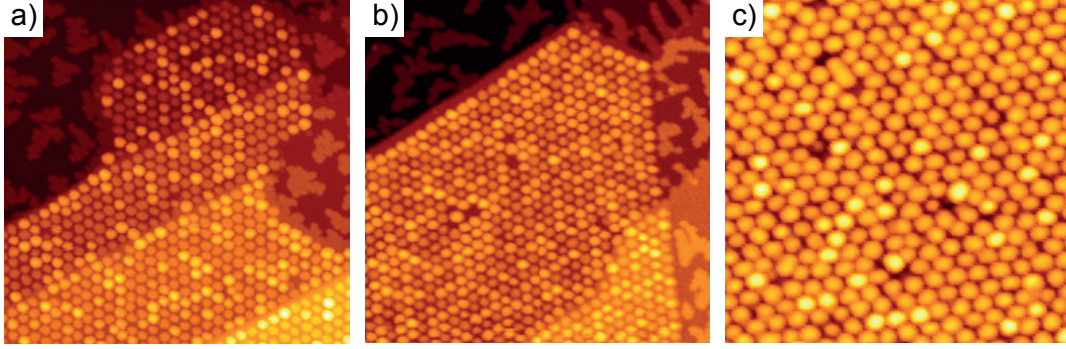


Figure 2.7 – STM topographs of graphene flakes on Ir(111) after deposition of a)  $\Theta = 0.2$  ML of Ir at  $T_{\text{dep}} = 300$  K, image size  $70 \times 70$  nm from [48], b)  $\Theta = 0.25$  ML of Pt at  $T_{\text{dep}} = 300$  K, image size  $70 \times 70$  nm [48] and c)  $\Theta = 0.18$  ML of Rh at  $T_{\text{dep}} = 130$  K and annealed to 400 K, image size  $40 \times 40$  nm adapted from [47].

many excellent paradigms of superlattices made of Ir, Pt, W and Rh clusters grown by ABE (see Fig. 2.7) [45–48, 132]. Atoms arrive from gas phase on the gr surface, diffuse in moiré mesh and nucleate to the region where the absorption energy is minimum forming clusters. Transition metals adsorb on the hcp region [45], while adsorption on the atop region was reported for Dy atoms [60]. The mechanism of cluster binding on gr/Ir(111) is realized either by covalent bonds or by van der Waals forces. The first mechanism induces a strong binding of C atoms with the clusters and also with the Ir atoms on the surface. This is attributed to the rehybridization of the C-C bonds of gr from  $sp^2$  to  $sp^3$  in the area of the clusters. The covalent bonds cause a “pinning” of gr to the substrate and also greater thermal cluster stability at high temperatures [133, 134]. The second mechanism implies a weak binding between gr and clusters leading to an earlier cluster diffusion as the temperature increases. For example, chemisorbed Ir clusters grow in registry with the template at room temperature and are thermally stable up to 550 K [45], whereas physisorbed Au ordered clusters grow at 100 K and are thermally stable up to 160 K [48]. Well-ordered superlattices from physisorbed clusters, like Au, can grow also at higher temperatures, by using previously small seeding clusters like Ir [48]. Clusters, due to three dimensional growth on the moiré mesh usually exceed the coverage of one monolayer before coalescence sets in. For example, in the case of Ir/gr/Ir(111) clusters start to merge above  $\Theta = 1.5$  ML [45].

The growth of clusters with well defined size, chemistry and long range periodicity is a key challenge in nanomagnetism and also for future technologies as BPMP. The moiré superlattice of gr/Ir(111) is a template for an ultra dense cluster arrays with the density of 115 Tbit/in<sup>2</sup> ideal for cluster arrays that can be seen as media for magnetic recording. One part of this thesis, deals with cluster superlattices made of rare earth on gr/Ir(111). The growth of a rare earth cluster superlattice, as from Sm, could open the possibility

## Chapter 2. Basics of nanomagnetism and nanostructure growth by ABE

---

to grow periodic arrays of bimetallic clusters made of  $4f$ - $3d$  metals that could show equivalent magnetic properties as in bulk. For instance,  $\text{SmCo}_5$  in bulk phase has one of the highest anisotropy energy densities observed to date [135].

## 3 Experimental Methods

In this chapter, the basic concepts of the used experimental techniques are briefly described. These are the Scanning Tunneling Microscopy (STM) and the Magneto-Optical Kerr Effect (MOKE). With the STM we gain insights on the nanostructure morphology down to the atomic level and with the MOKE, we obtain the magnetic properties as a signal coming from a large population of nanostructures. For more detailed information, references to corresponding articles are given each time.

### 3.1 Scanning Tunneling Microscopy

Among the numerous techniques in the field of microscopy, scanning tunneling microscopy is one of the most powerful, as its resolution is set not by the wavelength of a probe beam of photons or electrons, but by the overlap between the quantum mechanical wavefunctions between the last atoms on the tip and the atoms on the sample surface. The method was invented in 1982 by Binnig and Rohrer at the IBM research labs in Switzerland [136]. It was the first method capable of atomic resolution on flat surfaces in real space and only shortly after, in 1986, the two inventors were awarded the Nobel prize in physics.

To acquire an STM image, the surface of interest is scanned with an atomically sharp metal tip kept at a very short distance of typically less than 1 nm, which enables tunneling of electrons from the tip to the sample and vice versa. The lateral and vertical movement of the tip is realized by controlling three piezoelectric transducers. Upon applying a voltage bias, a piezoelectric transducer expands or contracts realizing the scanning movement with picometer accuracy. When the tip and sample are brought close enough for a tunneling current to arise, their Fermi levels on both sides equalize (see Fig. 3.2 a). By applying a bias voltage between tip and sample, a net tunneling current is created, which strongly depends on the distance between them (see Fig. 3.2 b). The tunneling current mostly arises from the highest energy levels at applied bias because

these levels have longer decay into the gap between the tip and the sample. This means that the current is proportional to the local density of states (LDOS) of the sample at the Fermi level.

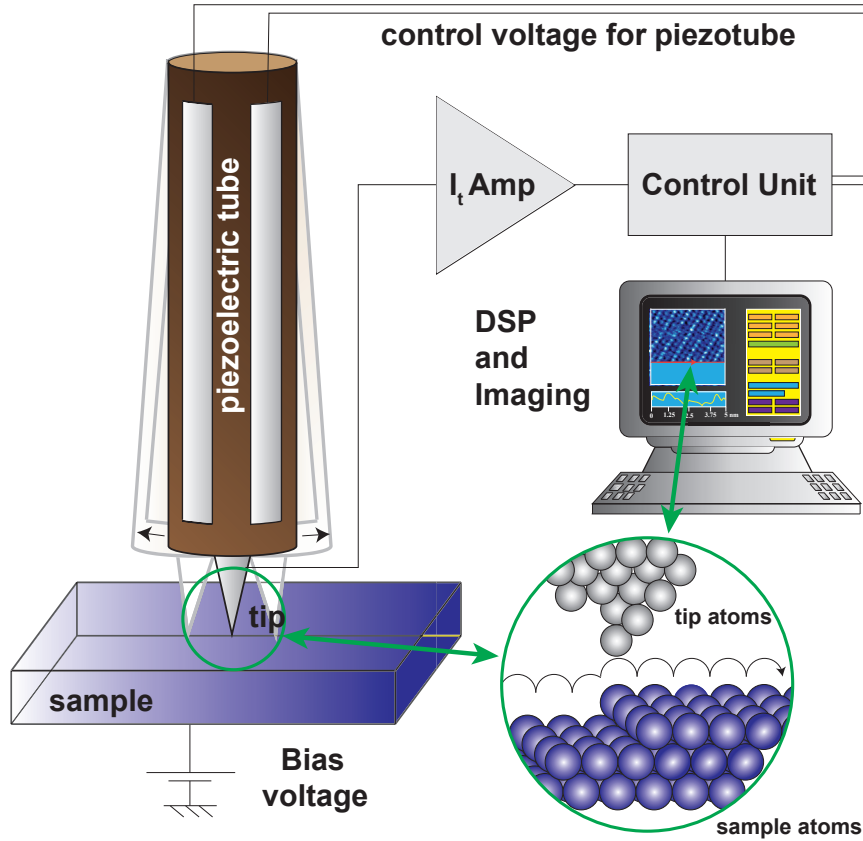


Figure 3.1 – A schematic representation of STM during operation. The metal tip scans the surface, driven by the  $x$  and  $y$  piezoelectric transducers. The tunneling current is amplified and fed back to the control unit. For constant current mode, the input of the current to the control unit sets the change in the vertical piezoelectric element. The difference in height then is recorded by the computer. The outcome of a complete scan of a region is the position of the  $x$  and  $y$  transducers with the apparent vertical variation, image reproduced from [137].

The mode of operation we used in our experiments is constant current imaging. In this mode the tunneling current is kept constant by adjusting the tip sample distance. In this mode the tunneling current is set to typical values, between some tenths of pA and several nA. The current variation produced by the surface roughness is compared to the set current value in a feed-back loop generating a voltage signal applied to the  $z$  piezoelectric transducer in order to move the tip to keep the tunneling current constant.

Already before the construction of the first STM, the phenomenon of tunneling had been subject to both experimental and theoretical investigations. One possible approach was

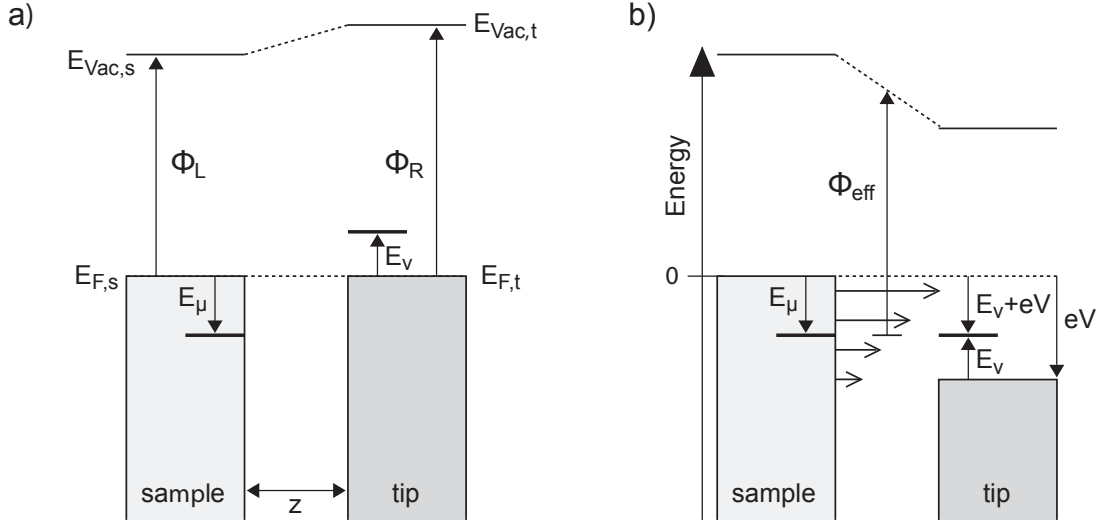


Figure 3.2 – Energy diagram of the tip-sample junction. a) without applied voltage. b) with applied voltage. The horizontal arrows represent the tunneling current. The higher the electron energy the larger the probability an electron to tunnel. Image adapted from [138].

given by the *transfer Hamiltonian theory*, as suggested by J. Bardeen in 1961 [139]. In most practical cases the tunneling barrier is broad enough to assume weak coupling between the two electrodes. In this case, each electrode can be treated separately, with a tunneling Hamiltonian as perturbation. Then, the many-particle tunneling current can be written to first order as

$$I_t = \frac{2\pi e}{\hbar} \sum_{\mu\nu} |M_{\mu\nu}|^2 [f(T, E_\mu) - f(T, E_\nu)] \delta(E_\nu + eV - E_\mu) \quad (3.1)$$

where  $f(T, E)$  is the Fermi function at temperature  $T$ , and  $V$  is the voltage applied between the electrodes. The main obstacle is then to evaluate  $M_{\mu\nu}$ , the matrix element for the transition of an electron in the state  $\psi_\nu$  in one electrode into a state  $\psi_\mu$  in the other electrode. For elastic tunnelling, Bardeen showed that

$$M_{\mu\nu} = \frac{\hbar}{2m} \int (\psi_\mu^* \nabla \psi_\nu - \psi_\nu \nabla \psi_\mu^*) dS. \quad (3.2)$$

The integration surface  $S$  lies in between the two electrodes. In order to further evaluate  $M_{\mu\nu}$  for the case of STM, one has to take into account the particular geometry of the setup. In an ideal STM, the probing electrode would only consist of a single point. As shown by Tersoff and Hamann [140], eq. 3.1 in this case reduces to

$$I_t(V_t) = \frac{2\pi e^2}{\hbar} V_t \sum_{\mu\nu} |M_{\mu\nu}|^2 \delta(E_\mu - E_F) \delta(E_\nu - E_F) \quad (3.3)$$



where  $\psi_{\nu}(\mathbf{r})$  are wave functions in the sample electrode at the lateral position  $\mathbf{r}$  with respect to the probe, and  $\delta(x)$  is the Dirac delta function. Thus, the ideal STM would measure a tunneling current which is proportional to the sample's LDOS at the position of the tunneling tip. The relation 3.3 gives a realistic description if the tip has uniform density of states at the Fermi energy and its wave functions are asymptotically spherical. In addition, the applied voltage should be sufficiently small and the temperature low. In a more realistic case of a tip with a radius  $R$  and position  $\mathbf{r}$ , eq. 3.3 becomes

$$I_t(V_t) \propto \rho_t(E_F) e^{2\kappa R} V_t \sum_{\mu} |\psi_{\mu}(\mathbf{r})|^2 \delta(E_{\mu} - E_F) \quad (3.4)$$

Here,  $\kappa = \sqrt{2m\Phi_{\text{eff}}/\hbar}$  represents the inverse decay length for the wave functions in vacuum.  $\Phi_{\text{eff}}$  is the effective tunneling potential barrier and  $\rho_t(E)$  is the density of states of the tip. Notably, this shows that for a constant tunneling voltage  $V_t$ , the current is proportional to the LDOS of the sample  $\rho_s(\mathbf{r}, E)$  that is

$$I_t \propto \rho_s(\mathbf{r}, E_F) = \sum_{\mu} |\psi_{\mu}(\mathbf{r})|^2 \delta(E_{\mu} - E_F) \quad (3.5)$$

This allows us to interpret constant current STM images as a map of the LDOS at the Fermi level. The exponential decay of the wave functions in the  $z$  direction yields  $|\psi_{\mu}(\mathbf{r})|^2 \propto e^{-2\kappa(d+R)}$  which, when substituted to eq. 3.4 gives

$$I_t \propto e^{-2\kappa d} \quad (3.6)$$

From the eq. 3.6 it is clearly seen that the tunneling current depends exponentially on the tip-sample distance  $d$ , which gives to the STM its outstanding vertical sensitivity.

## 3.2 Magneto-Optical Kerr Effect

The first experimental evidence of an interaction between light and magnetism was reported from M. Faraday in 1845 [141]. The first magneto-optic effect, called “Faraday effect”, refers to the rotation of linearly polarized light passing through a transparent magnetic material placed in between two electromagnetic poles. In 1876 a Scottish physicist, John Kerr discovered the equivalent effect to the Faraday effect, for a polarized reflected light from a magnetic surface [142, 143], the so-called “Surface Magneto-Optical Kerr effect” (MOKE).

There are two different approaches to explain the origin of the MOKE, the macroscopic and the microscopic. From the microscopic point of view MOKE manifests from the spin-orbit coupling between the electric field of the incident light and the wavefunction of the spin electrons in the magnetic material [144]. This coupling induces a change on the polarization of the reflected light that depends on the magnetization of the material. From a macroscopic point of view, the incident light wave causes the electrons present



### 3.2. Magneto-Optical Kerr Effect

in the magnetic material to oscillate in a plane parallel to the polarization plane of the electrons. If there is no magnetization in the sample, the incident light, which can be either linearly  $s$  or  $p$  polarized or circularly polarized light, will have the same polarization as the reflected light. When the sample has a net magnetization, the internal magnetic field acts on the electrons that are being displaced by the electric field of the light. The Lorentz force introduces an additional small oscillating component to the motion of the electrons that is perpendicular to the plane to the magnetization and the electric field vectors. The superposition of both contributions to the electrons in the magnetic material results in a rotated and slightly elliptical reflected light.

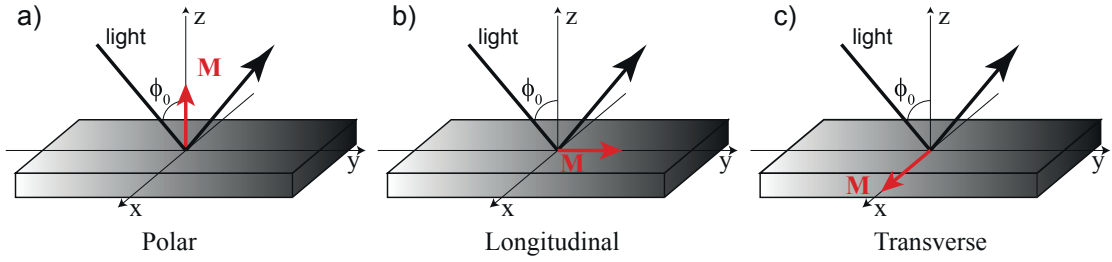


Figure 3.3 – Schematic representation of the different Kerr geometries. In our setup the magnetic field can be applied at any angle in the  $x - y$  plane with  $B_{max} = 312$  mT. The angle  $\phi_0$  is  $62^\circ$ . Image adapted from [145].

The validity of the macroscopic description of the magneto-optical effects may be questioned in the mono- or sub-monolayer regime. However, the magnetic properties for only a few atomic layers rapidly converge to the bulk limit and it is expected the global trend to be reproduced correctly [146, 147]. In order to describe the mechanism responsible for MOKE of a thick magnetic film, one has to employ Fresnel's theory of reflection. The Fresnel reflection matrix  $R$  relates to the incident and reflected light waves through the following relation:

$$\begin{pmatrix} E_p^r \\ E_s^r \end{pmatrix} = R \cdot \begin{pmatrix} E_p^i \\ E_s^i \end{pmatrix} \quad \text{where} \quad R = \begin{pmatrix} r_{pp} & r_{ps} \\ r_{sp} & r_{ss} \end{pmatrix} \quad (3.7)$$

In these equations the indexes  $i$  and  $r$  infer to incident and reflected waves, respectively and the indexes  $p$  and  $s$  define the electric field components parallel and perpendicular to the plane of reflection.  $E^i$  and  $E^r$  are the incident and reflected electric fields and  $r_{ij}$  are the Fresnel coefficients. For a detailed review one can refer to Ref. [148]. In MOKE there are three different configurations: polar, longitudinal and transverse (see Fig. 3.3). For polar and longitudinal geometries, the Kerr rotation  $\theta_K$  and ellipticity  $\eta_K$ , for  $s$  and  $p$  polarized light, can be found by the following expressions using the Fresnel coefficients:

$$\theta_K^p + i\eta_K^p = \frac{r_{sp}}{r_{pp}} \quad (3.8)$$

$$\theta_K^s + i\eta_K^s = \frac{r_{ps}}{r_{ss}} \quad (3.9)$$

In the traverse configuration the Kerr asymmetry, for  $p$  polarized light, can be found by the following expression:

$$A_K = \frac{|r_{pp}(+m_x)|^2 - |r_{pp}(-m_x)|^2}{|r_{pp}(+m_x)|^2 + |r_{pp}(-m_x)|^2} \quad (3.10)$$

The MOKE technique is particularly suited to study magnetization of surfaces. The rotation angle of the polarization is typically in the order of 1 degree for bulk and thick films. For submonolayer nanostructures the rotation angle is typically of a few 1/100th of a degree. From the experimental point of view it is important to note that MOKE is a spatially integrated technique covering areas equivalent to the laser beam spot, and with an depth sensitivity of a few tenths of nanometers. For a complete review of the MOKE theory one can refer to Ref. [149].

In our MOKE setup we measure the magnetization of the sample via the intensity of the reflected light and not directly from  $\theta_K$  or  $\eta_K$ . The intensity of the light is reaching a photodiode after passing through a polarizing filter which serves as an analyzer (see Fig. 4.3 in Chap. 4). The measured intensity is approximately linear with  $\theta_K$ , and consequently linear to  $|M|$ .

## 4 MBE Chamber and Sample Preparation

In this chapter, I introduce the home-made UHV chamber and the setups used for the STM and MOKE experiments. Additionally, I present the methods used for sample preparation, metal deposition with MBE and graphene deposition via CVD.

### 4.1 The Ultra High Vacuum System

The home-build UHV system was particularly designed for *in-situ* sample preparation and characterization by means of variable temperature (VT) STM, MOKE and Auger electron spectroscopy (AES) (see Fig. 4.1). The morphological and magnetic characterization as well as the deposition processes are performed with the sample in the very same position allowing for a full control of the sample temperature and minimal exposure to the residual gas. The samples, carried inside sample holders, can be exchanged by means of a load-lock UHV compatible and the chamber can host overall up to 4 samples in UHV conditions. The sample holder is fastened to the cooling stage by a spring lock mechanism, for easy swap. The sample can be cooled down by a liquid helium flux cryostat reaching a minimum temperature of  $T = 60$  K. The sample stage and the MOKE setup are mounted on a damping assembly consisting of a stacking of five different copper plates connected with viton rubber joints [150] (see in Fig. 4.3). The sample is pressed between two sapphire rings by tungsten leaf springs inside the sample holder (see Fig. 4.2). The sample holder is completely made by molybdenum. Thermocouple type-C wires are directly in contact with the sample and a third wire attached can be used either for applying high voltage during the annealing process or for the STM bias voltage. At the top of the sample holder there is a molybdenum stage with three ramps of helical shape for the coarse approach of the STM tip to the sample surface. A wobble stick can be used to transfer the sample holders between the main position, the load-lock entry, the AES position and the storage bay.

Two metal Omicron e-beam evaporators are constantly mounted. The sample is prepared

## Chapter 4. MBE Chamber and Sample Preparation

by sputtering with  $\text{Ar}^+$  ions and can be annealed by a 50 W filament mounted on the back side up to 2000 K by radiation and electron bombardment. Several gases as  $\text{O}_2$ ,  $\text{N}_2$  and  $\text{C}_2\text{H}_4$  (ethylene) can be precisely dosed by means of leak valves. The UHV chamber is equipped also with a quadrupole mass spectrometer (QMS) for monitoring the cleanness of the dosed gas and the chemical composition of the residual gas. The base pressure in the UHV chamber is approximately  $6 \times 10^{-11}$  mbar which is maintained by two in-series turbo molecular pumps, an ion pump and a Ti sublimator.

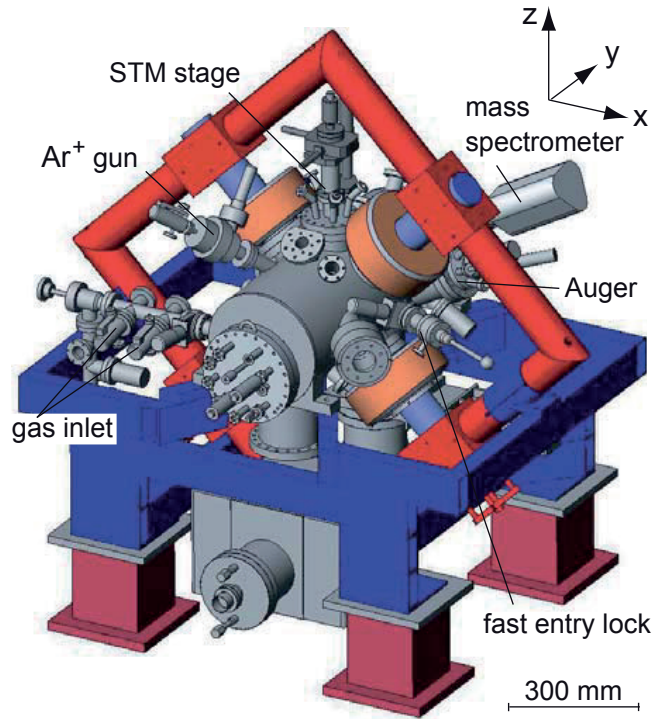


Figure 4.1 – Schematic representation the home-made UHV system. Image from [150].

The STM is a home built beetle type [151] suitable for varying temperature measurements. The internal structure is assembled by a tube with  $x$ ,  $y$ ,  $z$  and a vertical offset piezo elements and three feet where each one has three piezo stacked together. The tip is from tungsten wire prepared by electrochemical etching and fixed to the piezo tube. On the three feet are glued sapphire crystals of half spherical shape which are in contact with the molybdenum sample holder stage when STM is in operation. The coarse movement of the STM head for tip approach or retraction is achieved by the three feet. The lateral movement of the feet for the ascend and descend of the head is realized by stick-slip motion over the ramps. When working in normal sample exchange mode the STM can work optimally down to 80 K.

The MOKE setup was designed to be fully integrated inside the UHV chamber (see Fig. 4.3). The incorporation of all optical components inside the chamber omits the

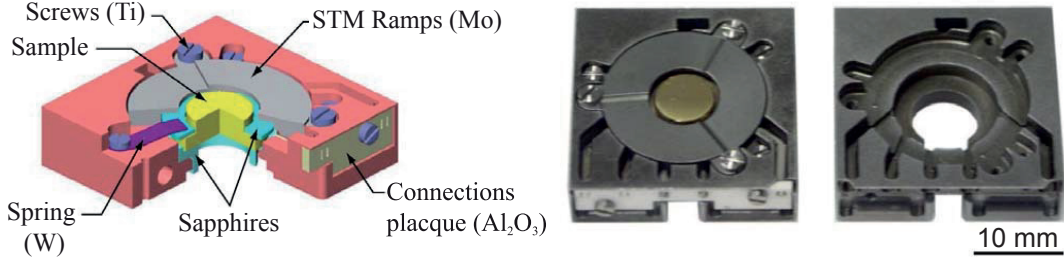


Figure 4.2 – Schematic (left) and images (right) of the home-made sample holder. Image adapted from [152].

additional noise induced by the air and the birefringence from the thick UHV windows. The enhanced sensitivity reduces the detection limit approximately to 0.1 ML and 0.5 ML for polar and transverse MOKE geometries, respectively [153]. To achieve this integration, the laser and the analyser of the setup are mounted on piezo-electric motors (Attocube, ANR100). The motors can rotate  $360^\circ$  with a minimum interval step of  $0.001^\circ$  capable for fine adjustments when setting  $s$  or  $p$  wave and also practical for closing the protecting shutters while preparing the samples. The laser diode is UHV compatible with a  $\lambda = 782$  nm set at 8 mW ( $I = 50$  nA). The laser spot area on the sample surface is approximately  $1 \text{ mm}^2$ . The incidence and reflective angle with respect to the substrate is  $62^\circ$ . The extinction ratio between the analyzer and laser from parallel to perpendicular alignment can exceed 1:40'000 for freshly polished sample surfaces. The magnetic field is driven by a four-pole electromagnet. Four cones are placed inside the vacuum chamber while coils and the soft iron yoke are situated outside. The maximum magnetic field at the sample position along the  $x$  or  $z$  direction is  $B_{\text{max}} = 312$  mT and at  $45^\circ$  the maximum field reaches 222 mT. The chamber and especially all parts on the manipulator are made from non magnetic materials in order to avoid artefacts during the Kerr measurements due to moving part driven by the switching field. Considering the fact that the laser diode is made with microfabrication techniques, it can not withstand temperatures higher than  $120^\circ\text{C}$ , a temperature which cannot be exceeded during the bake-out.

Measurements that are carried out first are always related to magnetism as the sample exposure to the residual gas can modify the magnetic properties of the studied nanostructures. Mainly, zero-field susceptibility measurements and hysteresis curves were acquired in this thesis with the MOKE setup. For a detailed review of this MOKE setup and the UHV chamber, one can refer to Ref. [150].

All the experiments in this thesis were performed in the above-described UHV system, except for a few low temperature STM experiments on the Sm nucleation on gr/Ir(111). Due to the measuring limitation of our system, we completed our experiments of this project using another UHV system in our group that can go down to 4 K and is equipped with a low temperature STM. For further information about the second UHV system used, one can refer to Ref. [154].

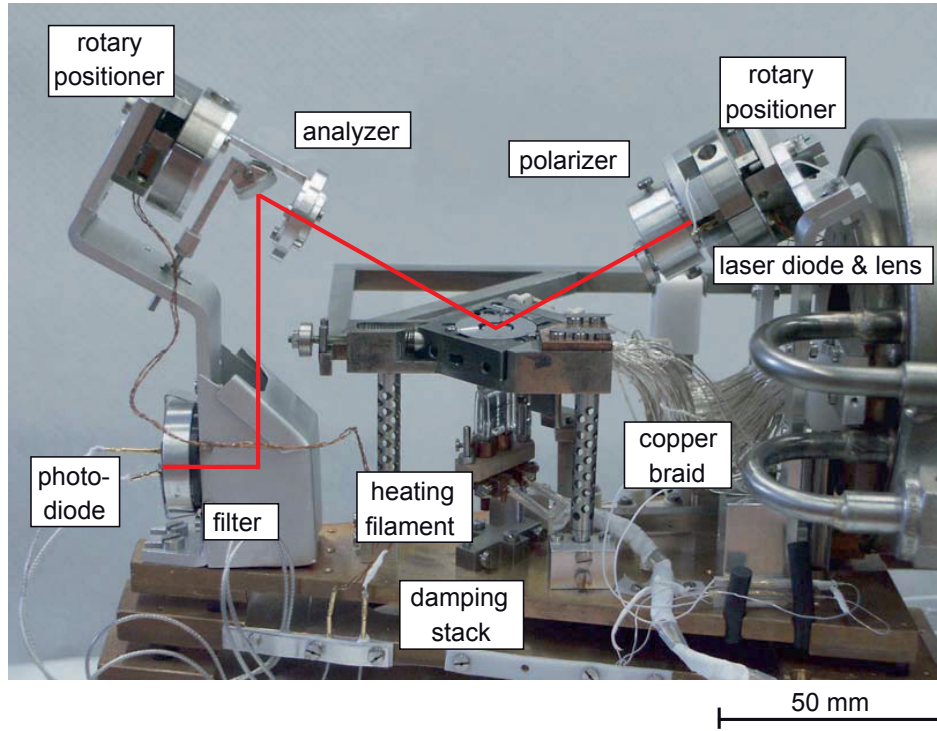


Figure 4.3 – Image of the manipulator with the *in-situ* combined UHV-compatible MOKE setup placed on a damping stage. Specific parts are indicated in the image. From [150].

## 4.2 Sample Preparation

The single crystals used in this thesis were Pt(111) and Ir(111). Before each experiment the sample surface has been cleaned by repeated cycles of sputtering and annealing. For Pt(111) crystal we repeated cycles of  $\text{Ar}^+$  ion sputtering at room temperature and at 800 K, subsequent exposure at the latter temperature to  $5 \times 10^{-8}$  mbar  $\text{O}_2$  atmosphere in order to reduce the C impurities and final annealing to 1300 K. The Ir(111) crystal was prepared by cycles of  $\text{Ar}^+$  ion sputtering at room temperature and at 1120 K, followed by annealing to 1500 K.

### 4.2.1 Metal Deposition

High purity rods of transition metals (Co, Ag, Pd, Rh) were sublimated from an Omicron evaporator by electron bombardment. For all depositions with commercial evaporators the pressure remained in the chamber below  $7 \times 10^{-11}$  mbar. Rh was also evaporated via W filament heating. In this occasion the pressure during deposition was approximately  $3 \times 10^{-9}$  mbar. The deposition flux for the transitional metals was  $5 \pm 2 \times 10^{-4}$  ML/s.

Sm and Dy were deposited from high purity rods heated by electron bombardment. The rods have been degassed for about one month to obtain a pressure  $p = 7 \times 10^{-11}$  mbar

during deposition. The deposition flux for Sm was set to  $5.5 \times 10^{-4}$  ML/s for the main UHV set-up and  $2.8 \times 10^{-4}$  ML/s for the second. For Dy, the deposition flux used was  $2.4 \times 10^{-4}$  ML/s for the main system and  $2.7 \times 10^{-5}$  ML/s for the second.

The deposition rate was calibrated by determining the coverage of a submonolayer with the STM. In order to minimize the errors from tip convolution, always the calibration depositions were larger than 0.4 ML. All STM images were recorded in the constant current mode. Samples were cooled down right after each deposition to avoid cluster diffusion while setting up the MOKE or STM. The STM data were processed using a freeware image processing software [155] and our home written software.

### 4.2.2 Graphene Growth

The gr layer was grown on Ir(111) by exposing the crystal surface kept at a temperature of 1400 K to 100 Langmuir of ethylene [114, 125]. At this temperature the hydrocarbons decompose when reaching the surface, leaving only the carbon atoms to form the gr. At the chosen ethylene exposition temperature, the graphene growth is self-limiting and only a single graphene layer forms at the end of the process, like a continuous carpet across the surface steps as checked by STM [114].





## 5 Nucleation of Sm and Dy Clusters on Graphene/Ir(111)

In this chapter we focused on the nucleation of Sm and Dy clusters on graphene (gr). We report the first example of self-assembled rare-earth cluster superlattice. As template, we use the moiré pattern formed by graphene on Ir(111); its lattice constant of 2.53 nm defines the interparticle distance. The samarium (Sm) cluster superlattice forms for substrate temperatures during deposition ranging from 80 to 110 K, and it is stable upon annealing to 140 K. By varying the Sm coverage, the mean cluster size can be increased up to 50 atoms, without affecting the long-range order. The spatial order and the width of the cluster size distribution match the best examples of metal cluster superlattices grown by atomic beam epitaxy on template surfaces. Regarding Dy, we couldn't observe a cluster superlattice formation for all investigated deposition temperatures.

### 5.1 Introduction

The fabrication of nanostructure superlattices has attracted a lot of attention in the last decades. Clusters of nanometric size display unique properties, neither seen in bulk nor in the individual atoms of the respective element [61]. In addition, the ability to create clusters with identical size and shape and to arrange them in ordered arrays has great importance for both fundamental research and applications. For example, equidistant, monodisperse, and equally oriented magnetic clusters have uniform magnetic moments and coercivity, and thus are the best candidates for applications in future magnetic recording media. Similarly, dense arrays of identical clusters are candidates for catalysts with improved performances.

One way of fabricating cluster arrays is the bottom-up approach by Atomic Beam Epitaxy (ABE) in ultra high vacuum (UHV) conditions [91]. Atoms are evaporated onto a template surface, where they diffuse and nucleate clusters on preferential sites. In this way, periodic arrays of seeds form, reproducing the symmetry and the period imposed by the template [15, 44–55]. Cluster size and shape can then be controlled to a certain

extent by varying the amount of deposited atoms (coverage), the substrate temperature during deposition ( $T_{\text{dep}}$ ), and the annealing temperature after deposition ( $T_{\text{ann}}$ ). Long range spatial order and narrow size distribution characterize high quality metal cluster arrays. Well known examples of templates for the assembly of metal cluster superlattices are the dislocation network that two layers of Ag form on Pt(111) to release the stress generated by the lattice mismatch [156], the reconstruction forming at the surface of Si(111) [157–159], Au(111) [160, 161] and vicinal Au surfaces [49], the moiré patterns observed for graphene [45, 162, 163] and hexagonal BN (*h*-BN) [145, 164] grown on mismatched transition metal substrates, or the hexagonal array of holes in the alumina bilayer formed by high temperature oxidation of Ni<sub>3</sub>Al(111) [53, 165].

So far, only clusters made of transition metals have been grown on such templates, while rare earths have been neglected despite their potential in magnetic and catalytic applications. The large spin-orbit coupling of the highly localized *4f* orbitals of rare earths can lead to large magnetic anisotropy [56, 57] overcoming the values observed in *3d* metals [166, 167], thus allowing for magnetic remanence in very small clusters. For example, magnetic remanence has been recently reported for Er trimers at 3 K [58], while trimers made of *3d* elements (Fe) exhibit magnetic bistability only at 0.3 K [59]. Moreover, bimetallic clusters made of *4f-3d* metals may well show very large coercive field similarly to what is observed in bulk [168]. In catalysis, rare earth oxides show high selectivity in the formation or decomposition of numerous chemical compounds [169–173].

Here we demonstrate the self-assembly of a rare earth cluster superlattice by ABE using the graphene moiré pattern formed on Ir(111) as template. Sm atoms order in cluster superlattices for deposition temperatures ranging from 80 K to 110 K. The interparticle distance of 2.53 nm is defined by the moiré period, with a single Sm cluster nucleated per moiré unit cell. The spatial order is preserved up to the Sm coverage yielding a mean cluster size of 50 atoms. The long range order and the width of the cluster size distribution set the Sm superlattice among the best examples of cluster arrays grown by ABE on template surfaces.

A similar study carried out with Dy reveals the absence of order. The observed cluster densities as a function of deposition temperature suggest that the adatom diffusion barrier of Dy is lower than that of Sm, in agreement with calculations of diffusion barriers on free standing graphene [174]. We attribute the formation (lack) of the Sm (Dy) superlattice to the delicate balance among the adatom diffusion barrier, the differences in adatom binding energies on the graphene moiré, and the Coulomb repulsion between the adatoms induced by charge transfer from rare earth to graphene.

## 5.2 Sm/gr/Ir(111)

We investigated the nucleation of Sm on gr/Ir(111) by measuring the island density as a function of deposition temperature  $T_{\text{dep}}$  for a Sm coverage  $\Theta_{\text{Sm}} = 0.08$  ML, with one monolayer (ML) corresponding to one rare earth atom per Ir(111) unit cell. Immediately after deposition, the sample temperature has been lowered to 80% of the deposition temperature in order to freeze surface diffusion and avoid post-deposition effects [175]. The sample morphology has been characterized by Scanning Tunnelling Microscopy (STM), for more information see the Chap. 4 . The cluster density  $n_x$ , expressed in ML, is the number of islands per Ir(111) unit cell, and is shown in the Arrhenius plot in Figure 5.1a. Since the moiré pattern is a  $(9.32 \times 9.32)$  superstructure with respect to Ir(111) [125], one cluster per moiré unit cell corresponds to  $n_x = 1.15 \times 10^{-2}$  ML, or  $\log n_x = -1.94$ .

Comparing with the STM images shown in Figs. 5.1(b - f) one can distinguish four regimes. The first starts at the lowest investigated  $T_{\text{dep}}$  of 56 K and goes up to 78 K. The clusters are disordered (see Figure 5.1b) and their density is higher than the moiré cell density. The second regime, ranging from 80 K up to 110 K, exhibits excellent order with one cluster per unit cell and these clusters are placed at identical site within the moiré unit cell, see Figure 5.1c. We attribute the fact that  $n_x$  is slightly smaller than one island per moiré unit cell to graphene defects that give rise to empty cells which can also be identified in Figure 5.1c. Above 110 K we enter in a third regime where the order is lost but the mean density stays around one island per moiré unit cell (Figure 5.1d). Above 130 K, the density sharply decreases and then reaches another stationary value for  $T_{\text{dep}}$  up to 200 K (Figure 5.1e). Finally, the fourth regime is characterized by progressive Sm intercalation with almost full intercalation taking place for  $T_{\text{dep}} = 280$  K, see Figure 5.1f. At this temperature the intercalated atoms move over large distances to form extended islands as for Eu on gr/Ir(111) [132].

To quantify the degree of spatial order and characterize the order-disorder transitions as a function of the deposition temperature, we use a procedure proposed for superlattices of 3D nanocrystals [176]. It is based on the quantitative analysis of the radial decay of the 2D-autocorrelation function (2D-ACF) derived from TEM and in the present case STM images. As we will see below, this allows to quantify differences between superlattices that appear of very similar quality to the eye. The 2D-ACF exhibits its global maximum in the image center ( $r = 0$ ) and, for ordered systems, satellite maxima which lie along the high symmetry directions of the superlattice. The position of these satellite maxima corresponds to the superlattice period. Their intensity is correlated with the degree of order including periodicity of the unit cells as well as uniformity of the shape and center of mass of the motif. Figure. 5.2b shows the radial profile of the 2D-ACF for a Sm cluster

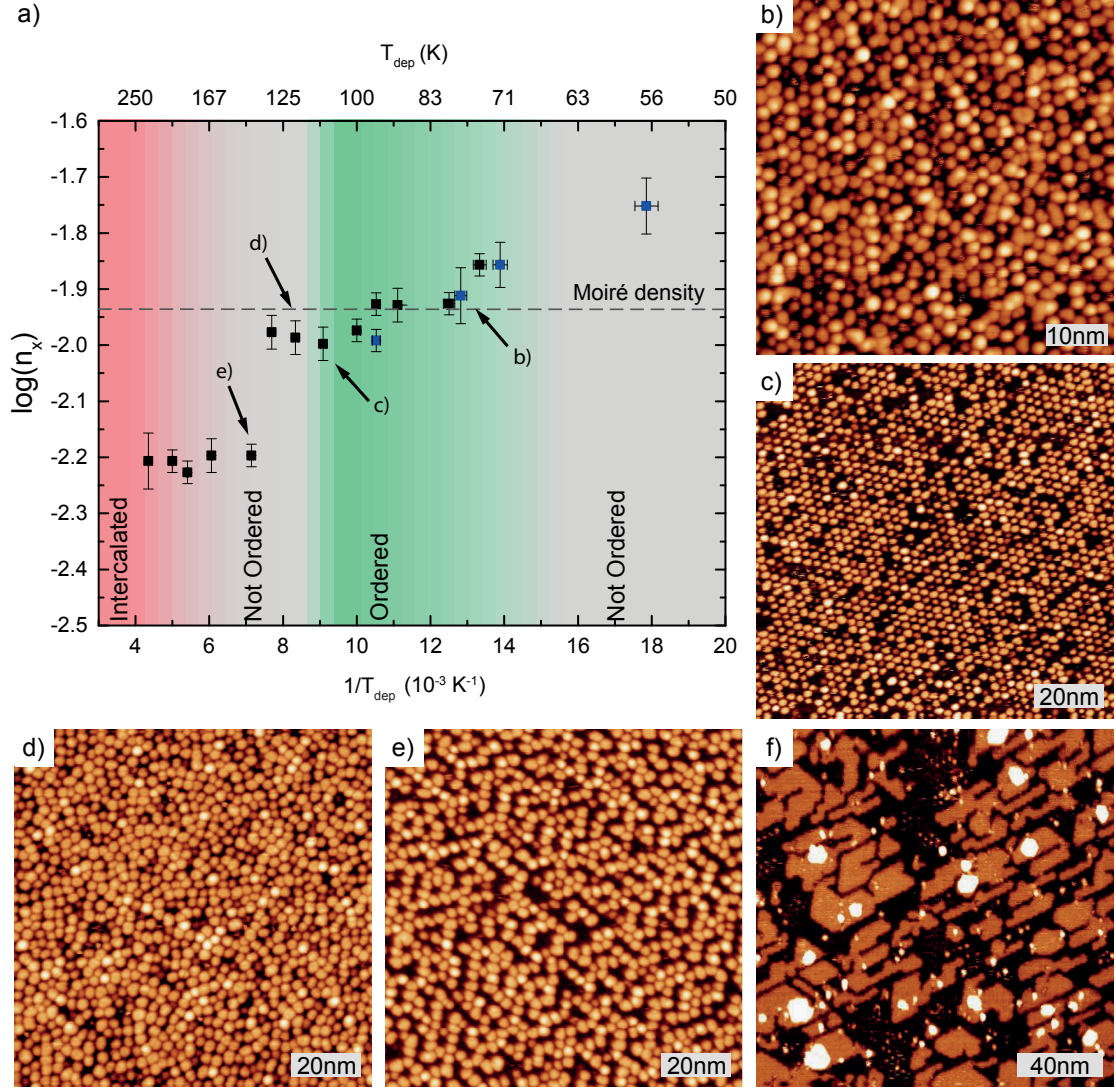


Figure 5.1 – (a) Arrhenius plot of the Sm cluster density as a function of  $T_{\text{dep}}$ . Black squares indicate VT-STM measurements and blue ones data taken with a 4 K STM (see Chap. 4). (b-e) STM images of Sm clusters on gr/Ir(111) for  $\Theta_{\text{Sm}} = 0.08 \text{ ML}$ . (b)  $T_{\text{dep}} = 78 \text{ K}$ , disordered regime ( $V_t = +1.0 \text{ V}$ ,  $I_t = 50 \text{ pA}$ ). (c)  $T_{\text{dep}} = 110 \text{ K}$ , one cluster per moiré unit cell and these clusters are situated at identical positions within the moiré, gr defects are causing some empty cells ( $V_t = -1.3 \text{ V}$ ,  $I_t = 75 \text{ pA}$ ). (d)  $T_{\text{dep}} = 120 \text{ K}$ , the density stays constant but the order is lost ( $V_t = -0.7 \text{ V}$ ,  $I_t = 50 \text{ pA}$ ). (e)  $T_{\text{dep}} = 140 \text{ K}$ , density is below one island per moiré unit cell ( $V_t = -0.6 \text{ V}$ ,  $I_t = 50 \text{ pA}$ ). (f)  $T_{\text{dep}} = 280 \text{ K}$ ,  $\Theta_{\text{Sm}} = 0.16 \text{ ML}$ , intercalated islands, appearance of clusters and islands in the second layer ( $V_t = -1.1 \text{ V}$ ,  $I_t = 60 \text{ pA}$ ).

superlattice grown at 100 K. Its envelope is fitted by the following function:

$$\text{env}(r) = A_{\infty} + f_0 \exp\left(-\frac{1}{2}(r/\sigma_0)^2\right) + f \exp\left(-\frac{1}{2}(r/\sigma)^2\right). \quad (5.1)$$



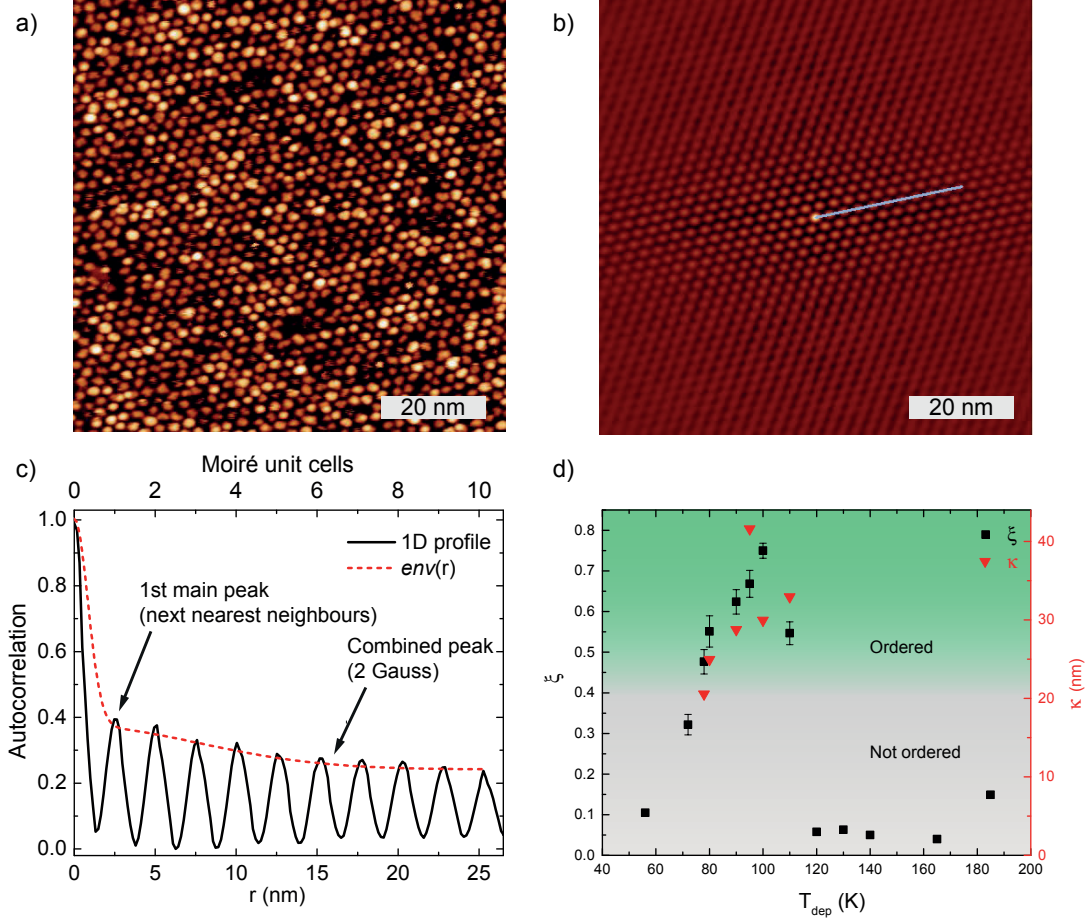


Figure 5.2 – (a) STM image of Sm clusters grown at  $T_{\text{dep}} = 100$  K ( $V_t = -1.1$  V,  $I_t = 60$  pA). (b) 2D-ACF of the image (a); the vertical direction is the slow scan direction and exhibits less order as it is more affected by distortions due to thermal drift. (c) Line-profile along a high symmetry direction of the 2D-ACF in (b) and of the envelope fit with eq 5.1 (dashed red line). (d) Figures of merit  $\xi$  and  $\kappa$  characterizing the order as function of deposition temperature.

$A_\infty$  is the asymptotic height of the satellite peaks as  $r$  goes to infinity. The first Gaussian term describes the central peak of the 2D-ACF. The height  $f_0$  of this peak is related to the sample roughness [177–179] and thus is sensitive to non-uniformities in cluster shape and height, and random voids, such as empty cells in our case. Apparent height variations due to modifications of the tip shape from image to image also contribute to the spreading of the  $f_0$  values. The width  $\sigma_0$  is usually set to one third of the mean interparticle distance [176], in our case  $\sigma_0 = 0.83$  nm.  $f$  and  $\sigma$  in the second Gaussian, together with  $A_\infty$ , are the parameters characterizing the long-range order of the superlattice. Small  $f$  and high  $A_\infty$  values indicate good long-range order. Two figures of merit,  $\xi$  and  $\kappa$ , have

been introduced to quantify the superlattice quality: [176]

$$\xi = \frac{A_{\infty}}{f + A_{\infty}} \quad (5.2)$$

$$\kappa = \frac{\sigma(f + A_{\infty})}{f} \quad (5.3)$$

$\xi$ , ranging from 1 for perfect superlattices to 0 for completely disordered systems, expresses the degree of long-range order by quantifying the decay of  $env(r)$  amplitude.  $\kappa$  indicates over which distance this decay takes place as it contains the width of the second Gaussian. However, this parameter gives useful information in addition to  $\xi$  only for ordered systems, since  $\kappa$  may well be high in disordered samples where both  $f$  and  $A_{\infty}$  are small (see example in A.1).

For the Sm superlattice, long-range order is observed for  $T_{\text{dep}}$  ranging between 80 K and 110 K, with 100 K giving the highest value of  $\xi = 0.75$ , as shown in Figure 5.2d. In this regime,  $\kappa$  is larger than 30 nm. From the 1D profile of the ACF we deduce an interparticle distance of  $(2.53 \pm 0.02)$  nm, demonstrating that the clusters nucleate in registry with the moiré pattern. The main source of disorder are the vacancies, their number is  $12 \pm 2\%$  of the moiré cells. Outside the 80 K - 110 K temperature range,  $\xi$  decreases to below 0.2.

Having introduced the above figures of merit, in Table 5.1 we compare the degree of long-range order of the Sm cluster superlattice with self-assembled island superlattices reported in literature. With  $\xi = 0.75$ , Sm/gr/Ir(111) is among the ones with the best long-range order. The only other system implying rare-earth atoms are Eu clusters on gr/Ir(111) [132]. It is characterized by  $\xi = 0.32$  and thus its long-range order is significantly lower. We underline that some superlattices characterized by uniform island size show low  $\xi$  owing to irregular island shape and to randomly shifted position of the island center of mass with respect to a defined location in the cell.

The long-range order of the Sm cluster superlattice is preserved up to a coverage of about  $\Theta_{\text{Sm}} = 0.5$  ML. For samples grown at  $T_{\text{dep}} = 90$  K,  $\xi$  only slightly decreases from 0.62 ( $\Theta_{\text{Sm}} = 0.08$  ML) to 0.56 ( $\Theta_{\text{Sm}} = 0.5$  ML) and  $\kappa$  from 30.6 to 18.4 nm, respectively. For coverages above 0.5 ML the clusters start to coalesce. For comparison, Ir clusters on gr/Ir(111) start to coalesce at a much larger coverage of about 1.5 ML. This quite early onset for the Sm cluster coalescence can be explained by the packing of the Sm atoms on the graphene surface. Two main aspects have to be considered. First, DFT calculations [174, 183] and STM measurements [60] indicate that rare earth monomers adsorb on the six-fold symmetrical hollow sites of the hexagonal carbon rings of graphene.

Table 5.1 – Figures of merit characterizing the long-range order for different cluster superlattices grown by ABE on template surfaces.  $\xi$  and  $\kappa$  are calculated from published data.  $\kappa$  in units of the pitch are rounded to the nearest integer. For vicinal surfaces  $\xi$  and  $\kappa$  have been evaluated along and perpendicular to the steps, and for the Au(111)-( $\sqrt{3} \times 22$ ) reconstruction along the  $[1\bar{1}2]$  direction. For superlattices with  $\xi < 0.4$ ,  $\kappa$  is not representative of the long-range order extension.

	System	$\xi$	$\kappa$ (nm)	Pitch (nm)	$\kappa$ (pitch)	$T_{\text{dep}}$ (K)
4f	Sm/gr/Ir(111)*†	0.75	31.8	2.53	13	100
	Eu/gr/Ir(111) <sup>+</sup> [132]	0.32	-	2.53	-	35
	Dy/gr/Ir(111)*†	0.27	-	2.53	-	70
3d	Rh/gr/Ir(111) <sup>+</sup> [47]	0.87	40.4	2.53	16	130
	Co/Au(788) $[\bar{2}11]$ [15]	0.76	55.8	3.5	16	130
	Pt/gr/Ir(111) <sup>+</sup> [48]	0.76	22.3	2.53	9	300
	Ir/gr/Ir(111) <sup>+</sup> [45]	0.75	28.4	2.53	11	300
	Rh/gr/Ir(111)*‡	0.73	39.7	2.53	16	110
	Fe/2 ML Cu/Pt(111) [50]	0.73	24.6	4.8	5	250
	Al/Si(111) <sup>×</sup> [158]	0.73	21.8	2.69	8	473
	Ir/gr/Ir(111)* [46]	0.67	12.1	2.53	5	300
	Co/GdAu <sub>2</sub> /Au(111) [51]	0.62	19.1	3.8	5	300
	Mn/Si(111) [159]	0.61	26.6	2.69	10	353
	Co/Au(11,12,12) $[01\bar{1}]$ [49]	0.61	20.2	7.2	3	300
	Co/Au(788) $[01\bar{1}]$ [15]	0.51	32.4	7.2	5	130
	Ag/2 ML Ag/Pt(111) [50]	0.46	17.7	7.0	3	110
	Co/ <i>h</i> -BN/Rh(111) [52]	0.46	11.6	3.2	4	4.2
	Pd/Al <sub>2</sub> O <sub>3</sub> /Ni <sub>3</sub> Al(111) [53]	0.44	26.7	4.5	6	300
	Fe/(NC-Ph <sub>5</sub> -CN) <sub>3</sub> Cu <sub>2</sub> /Cu(111) [54]	0.43	43.8	5.0	9	10+ann.
	Fe/Au(111) $[1\bar{1}2]$ [180]	0.37	-	7.3	-	300
	Co/Au(111) $[1\bar{1}2]$ [44]	0.35	-	7.3	-	300
	Ni/Au(111) $[1\bar{1}2]$ [181]	0.32	-	7.3	-	300

\* Full graphene layer

<sup>+</sup> Graphene patches

<sup>×</sup> Honeycomb lattice

† Present work

‡ Unpublished results (see in A.1)

We assume that this is also the preferred adsorption site for rare earth atoms forming clusters. Second, bulk Sm has a rhombohedral unit cell in which the Sm atoms have six nearest neighbors at a distance of about 3.6 Å in each close-packed layer [182]. However, bulk Sm is trivalent, while it becomes divalent in systems with reduced coordination, such as small clusters or monolayer films [184–186]. This change in valence has strong effects on the epitaxial growth as the radius of the divalent atom is significantly larger than that of the trivalent one. For example, a 22% expansion of the atomic radius has been measured for the divalent Sm atoms on the topmost monolayer of a Sm(0001) single

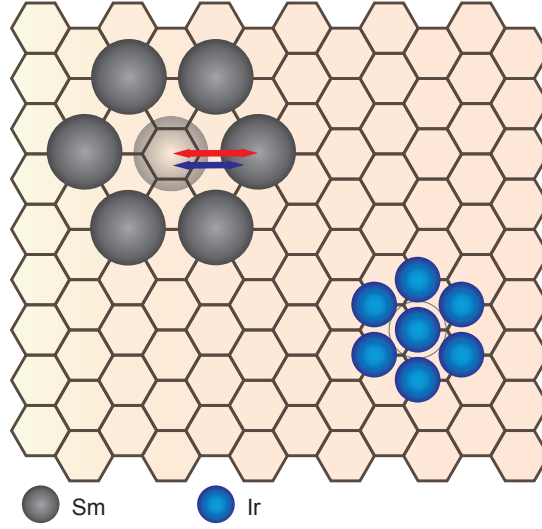


Figure 5.3 – Sketch for the packing of Sm (gray) and Ir adatoms (blue) on graphene. Sm adsorbs on hollow sites, while Ir adsorbs on C atoms sitting in fcc threefold hollow sites of Ir(111) (Ir substrate not shown). The red arrow shows the distance between two next nearest graphene hollow sites ( $4.26 \text{ \AA}$ ) and the blue arrow shows the bulk Sm-Sm distance ( $3.63 \text{ \AA}$  [182]). The radius of the spheres corresponds to the atomic radius. The radius of Ir atoms has been reduced by 20% for clarity of representation (the circle in the centre of the Ir heptamer shows the actual Ir radius).

crystal [187]. Reconciliation of these two aspects results in the sketch shown in Fig. 5.3 for the stacking of a Sm cluster on graphene. The distance between the central Sm atom, sitting on a graphene hollow site, and the nearest neighbor Sm atom, sitting on the next nearest neighbor gr site, amounts to  $4.26 \text{ \AA}$  which corresponds to an expansion of about 18% in the Sm atomic radius. This implies that the area occupied by a Sm atom is  $15.72 \text{ \AA}^2$ . By comparison, Ir atoms on gr/Ir(111) adsorb atop C atoms in fcc threefold hollow sites of the Ir(111), corresponding to an area of  $5.24 \text{ \AA}^2$  per Ir atom [134]. On the basis of these simple arguments we can expect an onset coverage for coalescence roughly three times smaller for Sm than for Ir, in agreement with our experimental observation.

In addition to the long-range order, a second parameter defining the quality of a cluster superlattice is the width of the cluster size distribution. For 0.08 ML of Sm deposited at 110 K, this distribution is shown in Figure 5.4b together with a Gaussian fit. The half width at half maximum (HWHM) of the size distribution is  $\sigma_{SD} = 0.31 \pm 0.01$ . This value is roughly half the one  $\sigma_{SD} = 0.59$  expected for homogeneous nucleation [91], equals the widths observed for several superlattices grown on template surfaces [45, 51, 150, 188–191], and is very close to the best result of  $\sigma_{SD} = 0.20$  [15, 50]. For the present system, two main factors contribute to the width of the size ( $s$ ) distribution. The first is the cluster coalescence which takes place above  $s/S = 3.2$ , with  $S$  the mean island size, and affects  $4 \pm 1\%$  of the islands. The second is the non uniform island height, with  $90 \pm 2\%$  of the islands being mono-layer and the remaining ones being bi-layer.



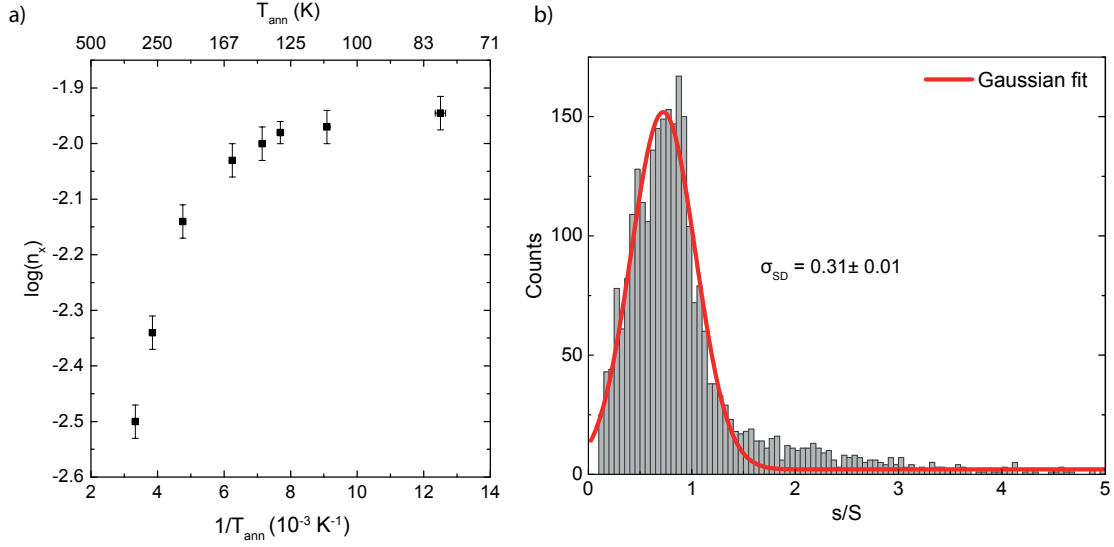


Figure 5.4 – a) Arrhenius plot of the cluster density  $n_x$  as a function of  $T_{\text{ann}}$  after depositing  $\Theta_{\text{Sm}} = 0.08 \text{ ML}$  at  $T_{\text{dep}} = 80 \text{ K}$ . b) Sm cluster size ( $s$ ) distribution for the as grown sample at  $T_{\text{dep}} = 110 \text{ K}$ . The average cluster size is  $S = 9$  atoms.

We investigated the thermal stability of the Sm superlattice by measuring the cluster density as a function of the annealing temperature  $T_{\text{ann}}$  (see Figure 5.4). The density remains constant up to 140 K from where on it reduces exponentially, leading to a progressive loss of order. This onset temperature can be related to the cluster-graphene interaction. On gr/Ir(111) clusters of similar sizes (coverage  $< 0.25 \text{ ML}$ ) show an onset temperature for coarsening of 160 K for Au, and of 550 K for Pt and Ir [48]. The high thermal stability observed for Pt and Ir is a consequence of the covalent bonds formed between the atoms in the cluster and the graphene layer, forcing an  $sp^2$  to  $sp^3$  re-hybridization of C [130], while a weaker bond is expected for Au due to its completely filled 5d-shell [48]. The low onset temperature observed for Sm, even lower than for Au, suggests then a weak Sm-graphene bond.

### 5.3 Dy/gr/Ir(111)

In order to investigate whether the superlattice formation is a general property of rare earth elements on graphene/Ir(111) or specific to Sm, we carried out similar experiments with Dy. For deposition temperatures ranging from 47 K to 210 K ( $\Theta_{\text{Dy}} = 0.07 \text{ ML}$ ) we did not observe the formation of cluster arrays. A cluster density close to the graphene moiré density is found for  $T_{\text{dep}} = 70 \text{ K}$  (see Figure 5.5a), lower than the 80 K measured for Sm. This observation suggests a lower diffusion barrier for Dy compared to Sm, in agreement with theoretical calculations on free-standing graphene [174] which represent a good approximation given the weak interaction between graphene and Ir(111) [131]. Additionally, we observe that intercalation starts at a temperature lower than for Sm,

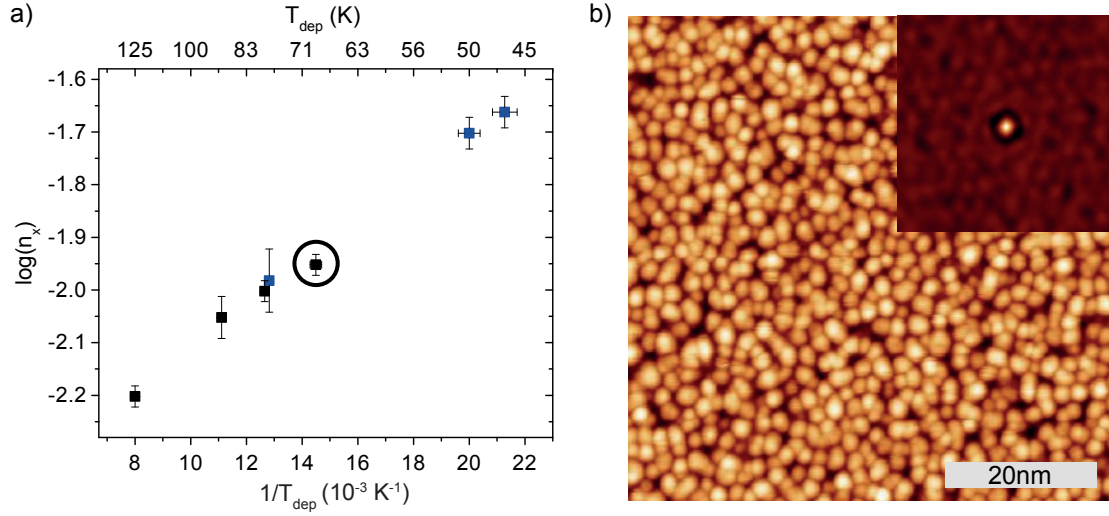


Figure 5.5 – (a) Arrhenius plot of Dy cluster density  $n_x$  for  $\Theta_{\text{Dy}} = 0.07$  ML as a function of  $T_{\text{dep}}$ . (b) STM image for  $T_{\text{dep}} = 70$  K ( $V_t = +1.0$  V,  $I_t = 100$  pA). At this deposition temperature the cluster density is close to the moiré cell density. Inset: 2D-ACF of the image in b), indicating short-range order.

namely at about 210 K. Figure 5.5b shows an STM image and the corresponding 2D-ACF of a sample grown at 70 K. The quantitative analysis gives  $\xi = 0.27$ . The absence of order suggests that the adatom diffusion barrier and the corrugation of the graphene moiré potential are not the only parameters responsible for the superlattice formation. A third ingredient is the Coulomb repulsion between rare earth adatoms induced by the charge transfer from adatoms to graphene [132, 174, 183]. Depending on the temperature, this repulsion hampers nucleation and leads to the formation of a 2D adatom gas from which clusters may nucleate by direct impingement of the incoming atoms on top of the adatoms. This nucleation channel competing with lateral attachment leads to disorder. This suggests that a certain balance between adatom diffusion barrier, graphene moiré potential, and adatom-adatom Coulomb repulsion is required for the superlattice formation.

## 5.4 Conclusions

We have studied the nucleation of Sm and Dy on the moiré pattern formed by gr/Ir(111). We observe the formation of a cluster superlattice for Sm deposition between 80 K and 110 K, whereas Dy clusters are disordered for all investigated deposition temperatures. The long-range order of the Sm superlattice has been evaluated in comparison with examples of transition metal cluster arrays from the literature. The present case is the first well ordered self-assembled superlattice for a  $4f$  element. Its long range order is competitive to the best results obtained for transition metals. The Sm cluster size distribution has a Gaussian shape with  $\sigma_{\text{SD}} = 0.31 \pm 0.01$  nm. Superlattices of Sm

clusters with an average size of 9 atoms loose the order by annealing at 140 K, suggesting a weak Sm-graphene bonding. The Sm superlattice formation opens the possibility to grow periodic arrays of two-element clusters, for example  $\text{SmCo}_5$  which is one of the strongest magnets discovered so far, without the need of an additional seeding element.



## 6 Tuning the MAE of Bimetallic Nanostructures

The continuous miniaturization of magnetic nanostructures has successfully led the magnetic recording media to recent areal densities of about 1 Tbit/in<sup>2</sup>. To further increase this density, the barrier known as the superparamagnetic limit has to be encountered. Future technologies, as HAMR, will require nanoparticles whose magnetization direction must be resistant to thermal fluctuations at higher temperatures than that of the current magnetic media and simultaneously, smaller in size [192]. Particles made of transition metal alloys such as FePt in the L1<sub>0</sub> phase demonstrate magnetization thermal stability at room temperature down to a diameter of 3 nm [135]. Below this threshold it is extremely challenging to engineer homogeneous alloy able to retain magnetic remanence above room temperature. As the particle size reduces, the surface to volume ratio increases and therefore, low coordinated atoms at interface or in the perimeter, give a significant contribution to the magnetic anisotropy energy (MAE) of the particles [62, 63, 193]. Bimetallic interfaces or interlines in such nanostructures can show larger MAE/atom and consequently higher anisotropies than the equivalent homogeneous alloys [63]. Therefore, nanostructures made of bimetallic interfaces and/or interlines can exhibit magnetic remanence at room temperature while consisting of fewer atoms than the smallest stable particles made of homogeneous alloys.

The aim of this chapter is to study an alternative approach to homogeneous alloy clusters to produce nanoparticles with high MAE leading to a stable magnetization at room temperature. The method consists in the enhancement of the magnetic hardness of 2D Co nanostructures, grown on Pt(111) by ABE, by tailoring the MAE with atomically sharp bimetallic interlines, at the island edges, and interfaces, at the top island surface (see schematic in Fig. 6.1). The interlines and interfaces consists of Co facing a *4d* metal. The *4d* elements used to this purpose were Rh ([Kr] 4d<sup>8</sup>5s<sup>1</sup>), Pd ([Kr] 4d<sup>10</sup>) and Ag ([Kr] 4d<sup>10</sup>5s<sup>1</sup>), three consecutive elements in the same row in the periodic table, thus with orbital occupation differing by one electron with respect to the neighbors. The slight different electronic structure induces different degree of magnetic polarization when these elements hybridize with a ferromagnetic material. Rh and Pd are considered

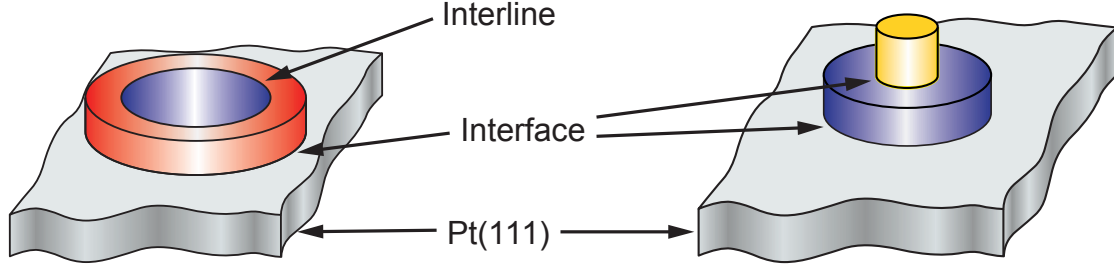


Figure 6.1 – Schematic representation of interfaces and interlines in Co island (blue) on Pt(111) surface (gray) generated by decoration with different elements (red and yellow), adapted from [63].

as highly polarizable elements [194, 195] therefore, their hybridization at the interface or interline in islands with a magnetic core should result in large induced magnetic moment and contribute to the particle MAE [146]. On the other hand, Ag usually shows very small polarization at the interface with a ferromagnetic element [196–199]. Hence, it is interesting to investigate whether an Ag interline (or interface) contributes to the MAE or it simply acts as a passivating and protecting shell for the Co core. A passivating layer is attractive when used in combination with a third material producing a MAE enhancement while facing the edge or the surface and a MAE reduction in the other case. In this situation, the passivating element can be used to suppress the MAE reduction at the interface/interline in order to only profit of the other positive contribution. A prominent example of such a situation is the capping of pure Co islands with Pd. During full capping, the Pd adatoms also attach to the edges of the Co cores forming interlines. This Co/Pd interline reduces the island MAE and thus works against the MAE enhancement produced by the Co/Pd interface [63]. A passivating edge shell with a low-polarizable material will beneficially wipe out the Pd interline negative effect, and will allow to maximize the island blocking temperature.

Our approach is based on the experimental measurement of the island magnetic susceptibility  $\chi(T)$  and morphology by means of MOKE and STM, respectively, combined with magnetic simulation analysis in order to quantify the different contributions to the island anisotropy. The evaluation of these contributions to the total MAE in such nanostructures is of key importance for gaining the ability to engineer islands with enhanced MAE. The monolayer capping for all studied elements has been found to contribute positively to the out-of-plane MAE of Co islands, with Pd giving the largest increase in the magnetic hardness. However, the lateral decoration of Co islands with all elements contributes negatively to MAE, with the Co/Pd shell giving the smallest effect and Rh the largest. Simulations of the magnetization reversal process by using CR and/or DW reversal models including different contributions to the MAE for atoms located at the interface ( $K_s$ ) and at interline ( $K_p$ ) and an exchange interaction between Co and  $4d$  transition metals have reproduced the experimental  $\chi'(T)$  and  $\chi''(T)$  curves. The Co/Ag interface contributes positively to the MAE with  $K_{s,Ag} = 0.16 \pm 0.02$  meV/atom

in agreement with previous studies [196, 198, 199] while the Co/Ag interline produces a negative MAE of  $K_{p,Ag} = -0.12 \pm 0.03$  meV/atom. Due to the low spin polarizability of the Ag we fixed the exchange stiffness  $A_{Co-Ag}$  to zero in the simulations. For Pd, we report  $K_{s,Pd} = 0.75$  meV/atom roughly double the value reported for Co/Pd thin film multilayers [200, 201], for the Co/Pd interface,  $K_{p,Pd} = 0.5$  meV/atom for Co/Pd interline and exchange stiffness  $A_{Co-Pd} = 3$  pJ/m. The Co/Rh interface exhibits  $K_{s,Rh} = 0.08$  meV/atom, almost an order of magnitude larger than previously reported [202],  $A_{Co-Rh} = 1.5$  pJ/m and  $K_{p,Rh} = -0.3$  meV/atom. Finally, a study of  $T_b$  as a function of the number of Pd capping layers reveals that the maximum MAE is achieved at about 2 monolayers of Pd, in agreement with previous studies on thin films [203, 204].

## 6.1 From Thin Films to 2D Nanostructures

The study of artificial materials, as two transition metal multilayers of which one constituent element is a ferromagnet, has attracted a lot of attention in the past both for fundamental research interest and for technological applications. The hybridization at interfaces between magnetic and non-magnetic in bulk elements has shown numerous examples of magnetization reorientation transitions or enhancement of the magnetocrystalline anisotropy [203, 205–207]. Remarkably, hybridization and reduced coordination at interface, has been predicted to lead to the onset of magnetism in thin films solely made of materials that are non-magnetic in the bulk [208–211]. The capping of thin ferromagnetic  $3d$  films by a non-magnetic transition metal may enhance (or contribute to) the MAE via the interface hybridization both because of the large spin-orbit coupling (SOC) of the  $d$  states as in the case of Co/Pt(111) [212–214] and the induced spin polarization as in the cases of Co/Rh(111) [194, 215] and Co/Pd(111) [200, 203]. Specifically, the  $4d$  transition metals are great candidates to enhance the MAE when form bimetallic interfaces with  $3d$  elements for two reasons. i) Their narrower  $d$ -band width compared to the  $5d$  metals explains why for example, Ru ([Kr]  $4d^7 5s^1$ ) and Rh ([Kr]  $4d^8 5s^1$ ), are closer to the onset of magnetism with respect to other transition metals with similar electronic  $d$ -band occupation as Pt ([Xe]  $4f^{14} 5d^9 6s^1$ ) and Ir ([Xe]  $4f^{14} 5d^7 6s^2$ ). This also implies that large magnetic moments up to  $m = 1\mu_B$ , can be induced in  $4d$  transition metals [215–217]. ii) Their SOC is more than double the value shown by the  $3d$  elements [218] which justifies their large contribution to MAE in cases where strong spin polarization occurs [211, 215]. In bimetallic  $3d$  -  $5d$  thin films, where large anisotropy manifests due to strong SOC at interface [219], an additional  $3d$  -  $4d$  interface is expected to increase the MAE even further.

From the growth of multilayers, research has focused on monolayer-high magnetic islands where, due to reduced coordination, atoms at the perimeter play also significant role to the MAE [62]. Conversely, interfaces and interlines of the same elements do not always contribute to magnetic anisotropy in the same way. For example, the capping with Pd of

Co islands grown on Pt(111) increases the magnetic hardness whereas, an interline of Co/Pd decreases the out-of-plane MAE of the edge Co atoms [63]. The use of interfaces and interlines made of different elements can optimally enhance the MAE of magnetic nanostructures.

### 6.2 Engineering Sharp Interlines and Interfaces

Magnetic nanoclusters have been grown on Pt(111) surface by ABE in UHV conditions ( $p_b \leq 6 \times 10^{-11}$  mbar). The sample surface was prepared by cleaning cycles and the transition metals were evaporated by electron bombardment as described in Chap. 4. The morphological and magnetic properties of the island ensembles were studied by means of STM and MOKE, respectively. The zero-field susceptibility signal was measured by generating a triangular sweeping field having an amplitude of 10 mT and oscillating at  $\nu = 9$  Hz. For further details regarding the UHV chamber one can refer to Chap. 4 or to Ref. [150].

Islands with defined densities and morphologies, have been produced by kinetic growth, away from thermodynamic equilibrium [91]. This is accomplished by performing growth steps with the precise selection of external parameters as: the deposition flux  $F$ , the sample deposition temperature  $T_{\text{dep}}$  and the sample annealing temperature  $T_{\text{ann}}$ . The core islands selected for this study are single layer, compact in shape in order to form sharp atomic interlines, made of Co and with a mean size of about 1200 atoms. The growth of the desired Co islands in our experiments was realized in two steps. First  $\Theta = 0.1$  ML was deposited at  $T_{\text{dep}} = 130$  K with  $F = 1 \times 10^{-3}$  ML/s which resulted in islands with density  $n_x = 4 \times 10^{-4}$  ML [145]. At this step the island density is set. The corresponding graphical sketch can be seen in Fig.6.2a. The islands grown at this deposition temperature are ramified due to the partially frozen edge diffusion [145]. By annealing the sample at  $T_{\text{ann}} = 280$  K for 300 s, edge diffusion and corner crossing become activated and thus, islands take compact shape (see Fig. 6.13a). At this temperature we deposit extra Co with a coverage varying, depending on the experiment, from 0.04 to 0.2 ML to produce larger islands of compact shape (see the sketch Fig. 6.2b).

In general different elements possess different diffusion barriers ( $E_b$ ) and attempt frequencies ( $\nu_0$ ) when deposited on the same crystal surface. For a successful island lateral decoration, adatoms of different elements landing on the crystal surface must be able to diffuse and reach the island edges. For this reason  $E_b$  and  $\nu_0$  for all studied elements must be known from literature or determined with preliminary experiments focused on the measurement of the island density as a function of the deposition temperature. For the formation of interlines one has also to consider that the growth of a second layer on top of the Co islands should be avoided. In the cases where an overlayer is observed,  $T_{\text{dep}}$  can be increased. This way the adatoms can overcome the ES barrier, descend the island and diffuse along the island edges. However, when the islands are large enough,



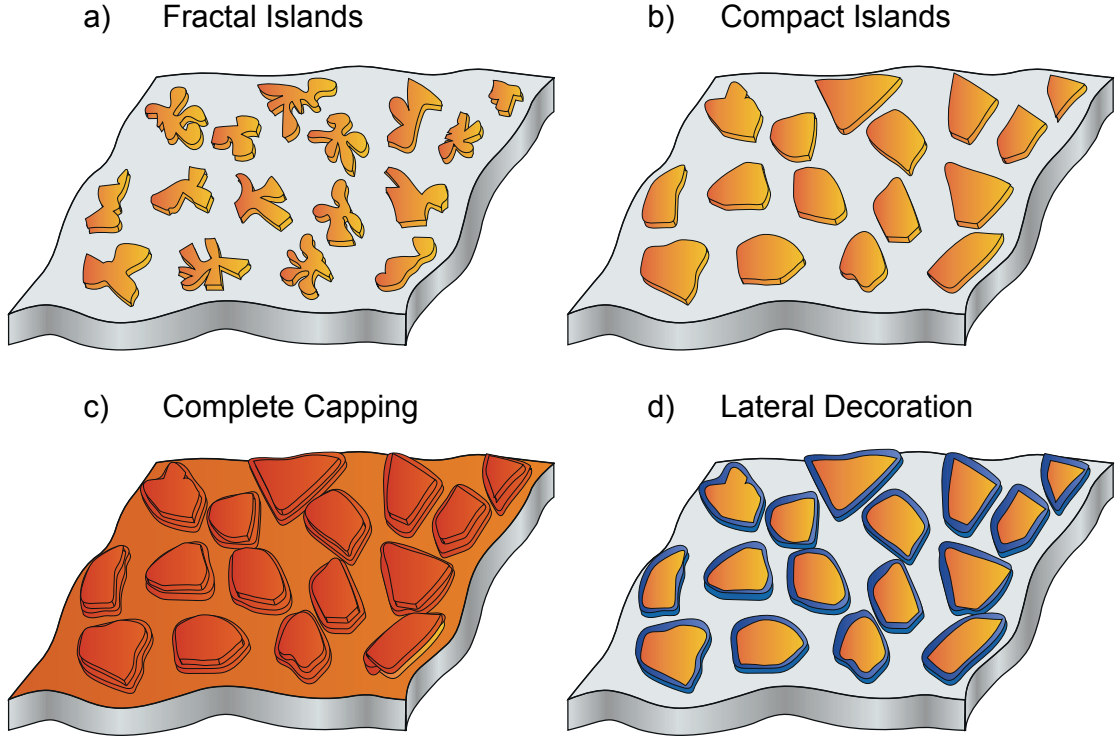


Figure 6.2 – Schematic representation of the growth of a) fractal islands: 0.1 ML Co at  $T_{\text{dep}} = 130$  K, at this temperature in the recipe the island density is set. b) Subsequent annealing at  $T_{\text{ann}} = 280$  K, islands become of compact shape and at this temperature additional Co is deposited to set the island size. c) Complete capping with a  $4d$  element. d) Lateral decoration of Co islands with a  $4d$  element.

increasing  $T_{\text{dep}}$  is not enough to avoid cluster nucleation on the second layer. In this case the adatoms should have sufficient energy to overcome the ES barrier (higher  $T_{\text{dep}}$ ) and at the same time smaller probability to collide and nucleate on top of the island. This can be achieved by reducing  $F$  (see Eq. 2.15). For example, in the case of Ag decoration at  $T_{\text{dep}} = 110$  K and  $F = 3 \times 10^{-4}$  ML/s [107] the Ag adatoms are mobile enough to reach the preexisting Co islands. However, to avoid the formation of a Ag overlayer  $T_{\text{dep}}$  was raised to 240 K and  $F$  set to a low value of  $F = 1 \times 10^{-4}$ . For Rh/Pt(111), since  $E_b$  and  $\nu_0$  were not known in literature we performed nucleation and growth experiments in order to find the correct decoration parameters (see Chap. 7). We selected  $T_{\text{dep}} = 350$  K with  $F = 9 \times 10^{-4}$  ML/s. In these conditions, our nucleation study of Rh on Pt(111) shows a Rh island density slightly smaller than the Co island density described above, thus ensuring complete lateral decoration (see Fig. 7.1a).

For the growth of all interfaces a complete capping was realized. Nominally, the formation of a continuous pseudomorphic epitaxial layer for a complete capping takes place by deposition at very high temperatures, where layer by layer growth occurs [220]. Due to the interface mixing between Co and Pt substrate starting at about 375 K [221] the

deposition temperature for the capping was limited to this temperature. Below 375 K, Pd and Rh grow in 3D mode (an example of Pd 3D growth can be seen in the supplementary information of Ref. [63]). To produce a smooth, one atom thick, capping layer we used a two-step growth procedure: first, deposition of 1 ML at the lowest possible temperature and second, subsequent annealing at room temperature [222]. The low-temperature deposition leads initially to the formation of a granular film which coalesce upon annealing at room temperature and forms a continuous monolayer. Regarding Ag, capping took place at 240 K, as it grows already as a continuous film at this temperature (see Fig. 6.5c).

For the successful growth and characterization of bi- and tri-metallic nanostructures some precautions should be considered. Since the nanostructures have atomically sharp interfaces and onion like interlines, temperatures at which atoms mix at the interface and at the edge shell must be avoided. Temperatures of atom insertion or exchange into the Pt(111) surface should be considered as well. The onset of this phenomena takes place for lower temperature during island growth than for already grown islands. For example, Co adatoms insert into the Pt(111) surface during deposition at  $T_{\text{dep}} = 180$  K [145] while interface exchange occurs at  $T_{\text{ann}} \geq 375$  K in islands or thin films [221]. In our studies we consider  $T_{\text{ann}} = 375$  K as the highest temperature during susceptibility measurements.

One additional effect to be considered is the nanostructure contamination. The nanostructures due to their low atom coordination have high reactivity to the residual gas, which degrades their magnetic properties quite fast [223]. Hence, MOKE measurements were always performed first, giving priority to the study of the magnetic properties of the nanostructures and afterwards to the study of the morphological characteristics by means of STM.

### 6.3 Magnetization Reversal Simulations

The energy required to reverse the magnetization of an island, i.e. the magnetization reversal energy, strongly depends on the reversal mechanism. As seen in Chap. 2, magnetic nanostructures can reverse their magnetization either by coherent rotation (CR), where the magnetic moments of the constituent atoms stay aligned during the entire reversal process [78, 224], or by nucleation and propagation of a domain wall (DW) [72, 225, 226] or by more complicated processes [227–229]. For this study two magnetization reversal models have been considered in the susceptibility simulations: CR and DW, where, depending on the island size and shape one is favored to the other [73–75].

From several STM images, acquired at random places on the crystal surface, we extracted the island size  $s$ , perimeter  $p$  and cross-section  $W_z$  (all given in atoms) for an ensemble of at least 500 islands (and additionally when needed, the partial decoration of the perimeter and of the overlayer). Since the islands in the ensemble have an irregular shape,  $W_z$  was considered as the largest width in each island. For the

### 6.3. Magnetization Reversal Simulations

CR model the magnetization reversal energy is :  $E_{\text{CR}} = sK_{\text{eff,CR}}$  where  $K_{\text{eff,CR}} = [(s - p)K_s + pK_p]/s$  is the effective anisotropy with  $K_s$  and  $K_p$  the anisotropy energies per atom for interface and interline, respectively. For the DW model we have:  $E_{\text{DW}} = 4W_z (A_{\text{Co-Co}}K_{\text{eff,DW}} + A_{\text{Co-4d}}K_{\text{eff,DW}})^{1/2}$  where  $K_{\text{eff,DW}} = [(W_z - 2)K_s + 2K_p]/W_z$  and  $A_{\text{Co-Co}}$  and  $A_{\text{Co-4d}}$  are the exchange stiffnesses between Co moments and Co and 4d transition metal moments, respectively. Additional parameters necessary for calculating the energy are: the Pt nearest neighbor distance  $d_{\text{nn}} = 2.775 \text{ \AA}$ , the reduced exchange stiffness between Co atoms due to the lower dimensionality of the atoms in the islands  $A_{\text{Co-Co}} = 15 \text{ pJ/m}$  [67, 74] and the pre-exponential factor  $\nu_0 = 5 \times 10^{11} \text{ Hz}$ .

In our simulations, the magnetization reversal energy of each individual island is calculated (for a specific set of  $K_s$  and  $K_p$  parameters) using CR and DW reversal mechanisms as a function of temperature. The smallest energy between the two reversal models is considered for each island. The contribution of each island is then summed up producing  $\chi'(T)$  and  $\chi''(T)$  curves. The corresponding developed Mathematica programming code is shown in section A.2 of the Appendix. For each reversal process, the increasing of  $K$  values for interface and interline anisotropy contribution results in a shift in the  $T_b$  to higher temperatures. In general  $K_s$  and  $K_p$  are anti-correlated as one can see in Fig. 5 of Ref. [74]. Any small change in one of the two energies leads to an opposite change to the other in order to maintain the susceptibility peaks at the same temperature. The precise evaluation of the agreement between the experimental data and the simulation curves was done by visual inspection and not by the sum of the squared residuals. During the fit, we focused primarily to the correct reproduction of the  $T_b$  peak position and secondly to the shape of the curves. In many cases the shape of the curves differs slightly from the experimental data, giving larger values to the sum of the squared residuals compared to the case of shifted  $T_b$  but well fitted curve shape. The errors bars in the  $K_s$  and  $K_p$  were derived by investigating changes in the  $\chi(T)$  curves from small variations around the optimum value.

The lack of atomic resolution in the STM topographies induces a larger uncertainty in the island perimeter evaluation compared to the surface. Kink sites, corners and in general the exact location of the perimeter atoms remain hidden; thus, the measured perimeter is a mean estimation of the actual perimeter length of the islands. The exact atomic structure of the perimeter strongly depends on the growth recipe. In addition, atoms at the perimeter with different coordination are expected to contribute differently to the island MAE. This implies that islands having the same perimeter and area in the STM images but grown with different recipes can show slightly different magnetic properties. This uncertainty on the island morphology is reflected on the  $K$  parameters which can slightly vary from one sample to the other. For this reason  $K_{\text{p,Co}}$  and  $K_{\text{s,Co}}$  have to be evaluated by fitting the  $\chi(T)$  curves for each sample. In addition, this uncertainty in the perimeter structure affects the value of  $K_p$  of the decorating element. To reduce this uncertainty we simultaneously fit the  $\chi(T)$  curves of pure Co islands and decorated islands in order to obtain the best estimation for the four  $K$  values,  $K_{\text{p,Co}}$ ,  $K_{\text{s,Co}}$  and

$K_{p,dec}, K_{s,dec}$ .

Between different evaporations, variations of the order of 5 to 10% in the coverage are observed. This imprecision in the coverage causes variations of  $T_b$  for nominally identical samples. For example, for pure Co islands with  $\Theta_{Co,total} = 0.25$  ML,  $T_b$  varies in the range  $115 \pm 15$  K. Therefore, the  $\chi(T)$  curves for pure Co islands were always acquired in every experiment in order to observe the exact change in  $T_b$  after the decoration or the capping with an element.

## 6.4 Dipolar Interactions

The reversal models described above assume non interacting islands. This situation is verified in our samples and supported mainly by two arguments. First, as we saw in Chap. 2 the width of  $\chi''(T)$  and the decay in  $\chi'(T)$  for  $T > T_b$  can bespoke the existence of mutual interactions. More specifically, for interacting particles, the  $T_b$  peak is broad and asymmetric; at the same time  $\chi'(T)$  for  $T > T_b$  decays with a slower rate than  $1/T$  [81]. The experimental  $\chi'(T)$  data show a slightly steeper decay than  $1/T$ , indication for non-interacting particles [62] (see Fig. 6.6a, orange line). Second, we estimated the mutual dipolar interactions affecting the islands in our samples. To this purpose we assumed point like, equally spaced islands in a triangular pattern (see sketch in Fig 6.3) with interdistances equal to the mean experimental island distance of  $k = 200 \text{ \AA}^1$ . All the islands have the same size, equals to the mean size of  $N = 1200$  atoms with  $m = 2.4\mu_B$  for the magnetic moment per Co atom including spin, orbital and induced magnetic moment in substrate/capping layer. The magnetic flux density generated by a point-like island at distance  $\mathbf{r}$  from the island in the center of the coordinate frame in given in units of Tesla by:

$$\mathbf{B}(\mathbf{r}) = \frac{\mu_0}{4\pi} \left( \frac{3\mathbf{r}(N\mathbf{m} \cdot \mathbf{r})}{r^3} - \frac{N\mathbf{m}}{r^3} \right) \quad (6.1)$$

where  $N\mathbf{m}$  is the total magnetic moment of each island. In our model the magnetic moment  $\mathbf{m}$  is always perpendicular to the island surface plane, due to the out-of-plane anisotropy, and thus to the distance  $\mathbf{r}$ . For this reason, the scalar product in the first term inside the parenthesis is 0 reducing the equation to:

$$\mathbf{B}(\mathbf{r}) = \frac{\mu_0}{4\pi} \left( -\frac{N\mathbf{m}}{r^3} \right) \quad (6.2)$$

Considering finite size particles in place of the point like assumption introduces an extra term proportional to  $(N\mathbf{m})/r^5$  [230]. As  $\mathbf{r}$  increases, the term with  $1/r^5$  goes much

---

<sup>1</sup>For this interdistance length one can easily exclude any mutual interactions from the RKKY model, where the effective distance is of a few nanometers.

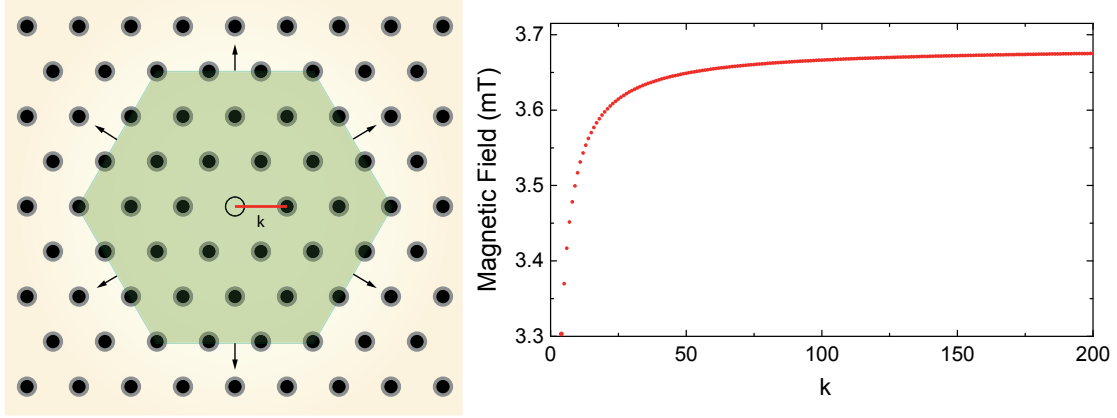


Figure 6.3 – Left side: Schematic representation of point like islands arranged in a trigonal lattice,  $k$  represents the distance between neighbor islands. Right side: Magnetic field on the center of the coordinate frame, corresponding to the white point like island, generated by the islands contained in a given hexagonal surface (green shadow area) of radius  $nk$  ( $n$  is an integer).

faster to zero compared to the term with  $1/r^3$ , therefore its contribution has negligible effect to our model. This implies that a model with point-like islands still reproduces quite realistic results of dipolar interactions of equally spaced islands.

Fig. 6.3 shows the dependence of the induced magnetic field generated by all the islands inside a given area as a function of its size. Already, for a  $10k$  radius (450 surrounding islands) the induced field has almost 1% difference from the value calculated for the area with radius  $11k$ . At  $100k$  the magnetic field is close to the saturation value and by increasing the integration radius to  $200k$  the magnetic field value is increasing by less than 0.2%. The calculated field from contribution of all islands in the hexagonal area with radius equal to  $200k$  (about 160 thousand islands) is 3.67 mT. This value is approximately one third the amplitude of the AC field used in the zero-field susceptibility measurements, justifying our experimental choice for the MOKE measurements, and indicates negligible dipolar interactions. All these findings strongly support the absence of accountable dipolar interactions between the islands of the specific grown ensemble.

## 6.5 Co/Ag Interline and Interface

### 6.5.1 Decoration morphology

The edge decoration and capping with Ag was studied by means of STM. Ag forms a non-uniform partial rim around the island edges with an apparent height of  $2.75 \pm 0.15$  Å, which can be easily separated due to a sharp chemical contrast from Co ( $2.2 \pm 0.1$  Å) in the STM images (see examples in Fig. 6.4 and Fig. 6.5a, b). The Ag coverage used in the experiments was foreseen for a three atom uniform lateral decoration around Co

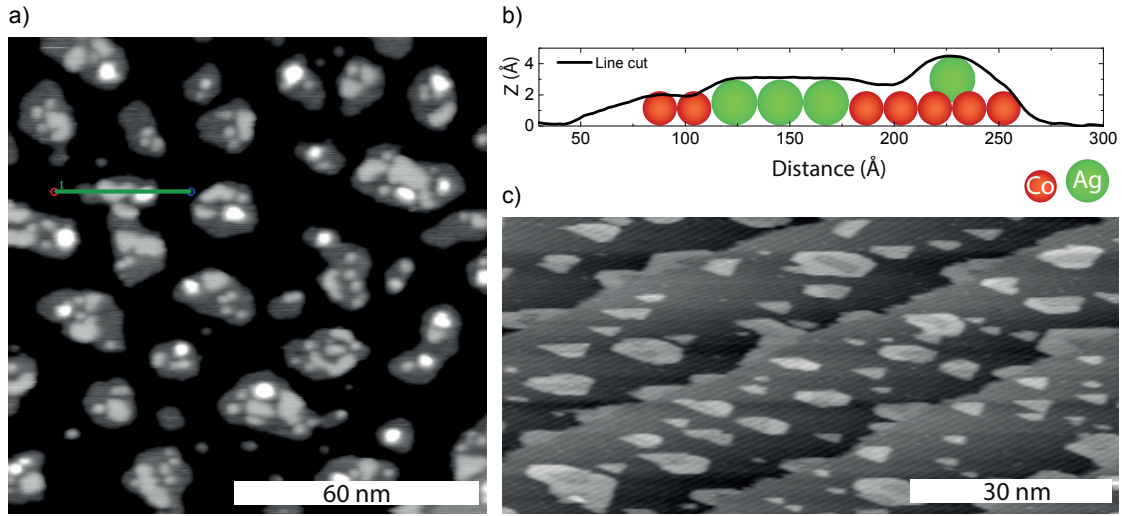


Figure 6.4 – a) STM topography of Ag clustering inside Co islands, light gray represents the Ag in the first layer and white color the Ag in the second. Co 0.25 ML deposited in two steps, 0.1 ML at  $T_{\text{dep}} = 130$  K and 0.15 ML at  $T_{\text{dep}} = 280$  K, followed by Ag 0.1 ML at  $T_{\text{dep}} = 280$  K ( $V_t = -0.4$  V,  $I_t = 1$  nA), b) line cut along the green line shown in a) showing the Co, Ag in first and second layer. Ball model illustrates the two different elements, red balls: Co atoms, green balls: Ag atoms. c) STM image of Co 0.14 ML islands (with the same growth recipe as in a) decorated partially with Ag = 0.08 ML at  $T_{\text{dep}} = 250$  K, the image has a non-constant thermal drift in the slow scan direction ( $V_t = -0.3$  V,  $I_t = 1$  nA).

edges. However, the Ag interline is not present in all islands and only a small portion is fully decorated. In general, Ag is found to decorate partially the Co island edges for  $220 \text{ K} < T_{\text{dep}} < 250 \text{ K}$  and  $\Theta_{\text{Ag}} = 0.1 \text{ ML}$ . The inhomogeneous Co decoration by Ag is attributed to the high mobility of Ag adatom when diffusing along Co step edges and crossing island corners. Due to this, the Ag adatoms attached to a Co island diffuse until they find another Ag adatom and nucleate. This explains Ag accumulation on one side of the island that leads to the observed partial decoration of Co islands.

The partial decoration is not related to the island size or shape as Ag atoms attach to the smallest islands and at the same time are absent in the neighboring islands of different size and *vice versa*. At  $T_{\text{dep}} = 220$  K with  $F = 3 \times 10^{-4}$  ML/s Ag forms also an overlayer on top of Co islands due to ES barrier. The increase of  $T_{\text{dep}} = 250$  K and at the same time: the reduction of flux to  $F = 1 \times 10^{-4}$  ML/s and total Co coverage to  $\Theta_{\text{Co}} = 0.14$  ML, led successfully to the complete elimination of the overlayer (see Fig. 6.4c). At  $T_{\text{dep}} = 280$  K Ag forms clusters inside the Co islands. Fig. 6.4a shows Co islands with inserted Ag creating local clusters inside the islands, the island shape has change from trigonal to round-like. This Ag clustering inside Co islands is not observed when depositing Ag at  $T_{\text{dep}} = 220$  K and subsequently annealing to  $T_{\text{ann}} = 300$  K. Regarding the Ag/Co interface,  $\Theta_{\text{Ag}} = 1$  ML was deposited on top of Co islands at



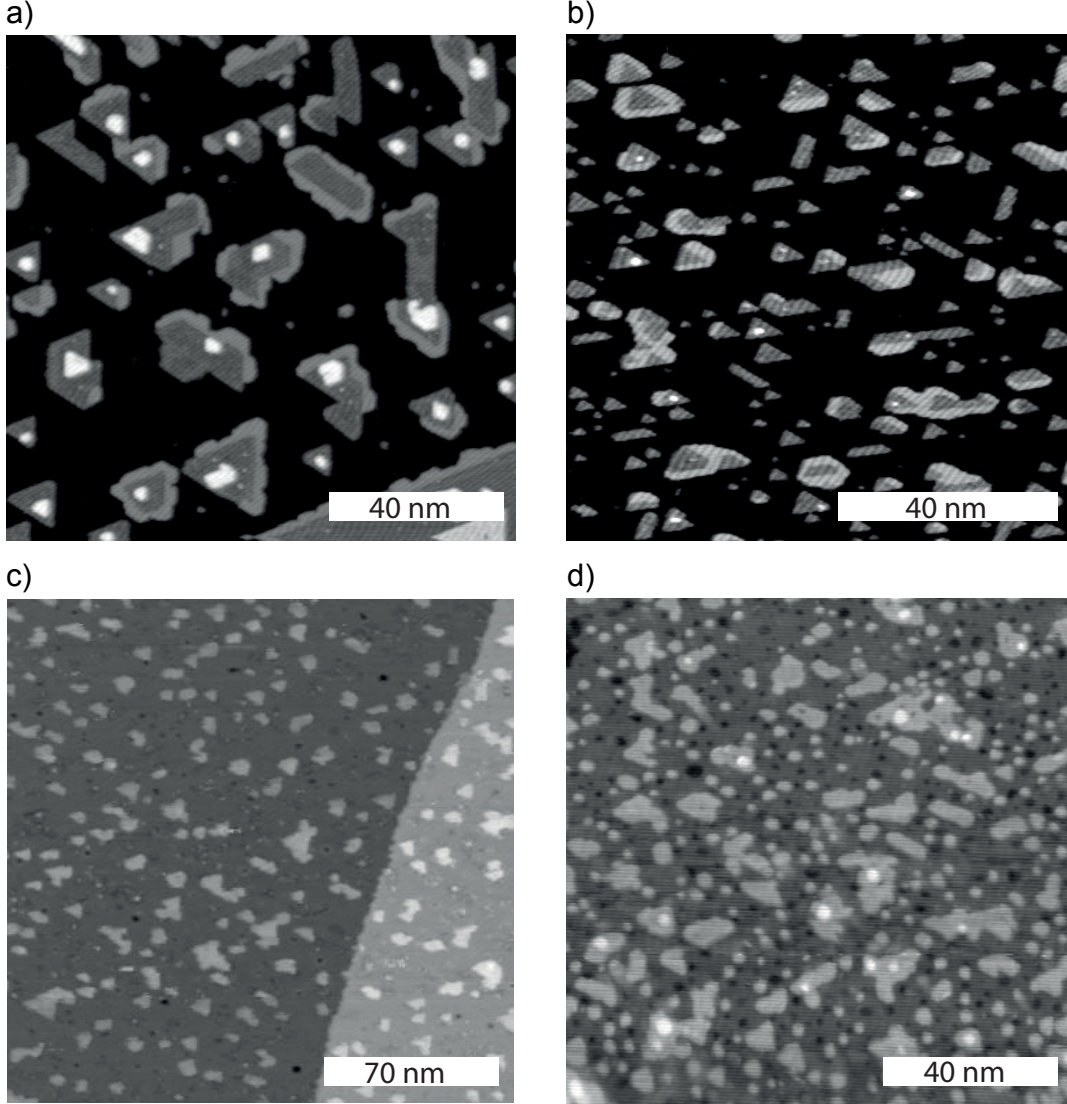


Figure 6.5 – a) Co 0.25 ML deposited in two steps, 0.1 ML at  $T_{\text{dep}} = 130$  K and 0.15 ML at  $T_{\text{dep}} = 280$  K, followed by Ag 0.1 ML at  $T_{\text{dep}} = 220$  K, light gray represents the Ag decoration and white color the Ag overlayer ( $V_t = -0.3$  V,  $I_t = 1$  nA), b) Co 0.14 ML, (0.1 ML  $T_{\text{dep}} = 130$  K and 0.04 ML  $T_{\text{dep}} = 280$  K), Ag 0.08 ML  $T_{\text{dep}} = 250$  K ( $V_t = -0.3$  V,  $I_t = 1$  nA), c) Co 0.14 ML (with the same growth recipe as in b) capped by 1 ML Ag at  $T_{\text{dep}} = 240$  K,  $T_{\text{ann}} = 300$  K ( $V_t = -0.4$  V,  $I_t = 1$  nA), d) 0.18 ML Co deposited as in a) and capped by 1 ML of Pd ( $T_{\text{dep}} = 90$  K and annealed to  $T_{\text{ann}} = 350$  K) ( $V_t = -0.6$  V,  $I_t = 1$  nA).

$T_{\text{dep}} = 240$  K. Fig. 6.5c shows Co islands completely capped by Ag, between Co islands, Ag forms a surface reconstruction due to the lattice mismatch with Pt(111) substrate (4.3%) as seen previously in Ref. [231].

### 6.5.2 Magnetic characterization

The  $K$  values for Ag interfaces and interlines have been evaluated based on samples with partial decoration and capping (see Fig. 6.6). This was strategically selected because in the case where the overlayer is absent, the islands are so small that i) their signal is close to the sensitivity limit of the MOKE setup and ii) the induced  $T_b$  shifts towards lower temperatures not accessible in our experimental setup. In the case of partial capping the  $T_b$  of Co islands with  $\Theta_{\text{Co}} = 0.25$  ML is at about 120 K and thus it is better suited to acquire full experimental  $\chi'(T)$  and  $\chi''(T)$  curves for comparison with the simulation. For this case we extracted additional information of the island ensemble as the portion of the Co perimeter in contact with Ag, the portion of Co perimeter left free, and the Ag area on top of the Co area and the free Co area. To decide on the sign of the interface and interline anisotropy terms and direct the simulation on the right direction we note that the reduction of  $T_b$  when decorating small Co islands (0.14 ML) with Ag (where

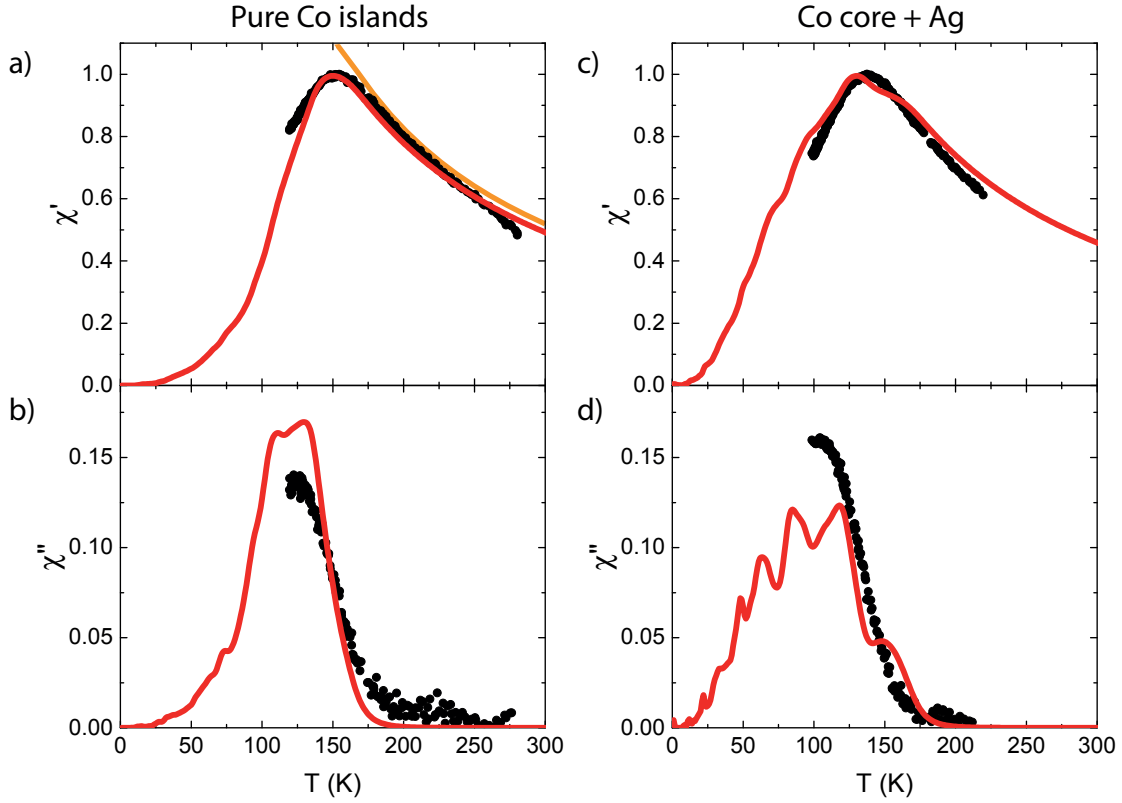


Figure 6.6 – Experimental and simulated zero-field susceptibility curves. The external field has been applied perpendicular to the sample surface. a), b) pure 0.25 ML Co islands deposited in two steps, 0.1 ML at  $T_{\text{dep}} = 130$  K and 0.15 ML at  $T_{\text{dep}} = 280$  K. e), d) 0.25 ML Co islands partially decorated with 0.1 ML Ag at  $T_{\text{dep}} = 220$  K. Black symbols: experimental data, red lines: best fit simultaneously reproducing curves for both Co and Ag decorated islands ( $K_{\text{s,Co}} = 0.065$  meV/atom,  $K_{\text{p,Co}} = 0.95$  meV/atom,  $K_{\text{s,Ag}} = 0.16$  meV/atom,  $K_{\text{p,Ag}} = -0.12$  meV/atom). Orange line:  $1/T$  decay.



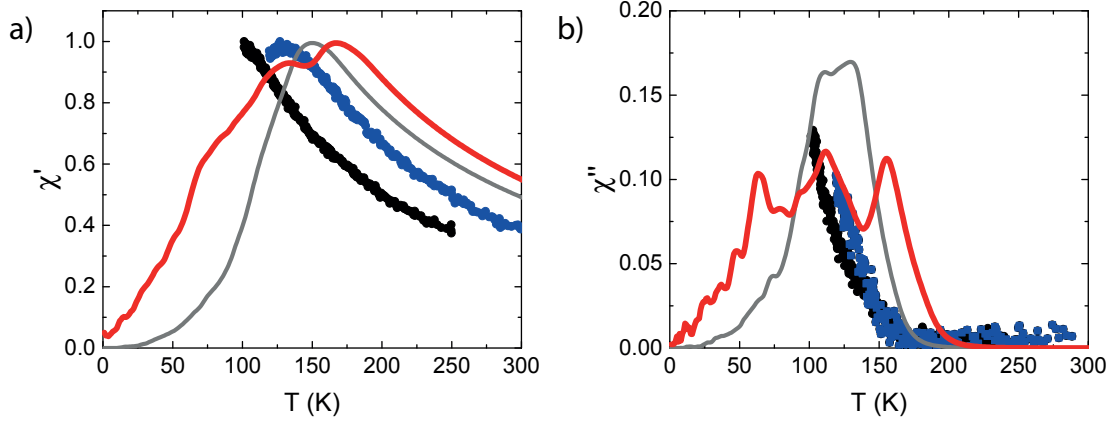


Figure 6.7 – Out-of-plane zero-field experimental and simulated susceptibility curves for Co islands completely capped with Ag. Black symbols: experimental data for small Co islands (0.14 ML), blue symbols: small Co islands completely capped with Ag, gray lines: simulation curves for 0.25 ML pure Co islands ( $K_{s,\text{Co}} = 0.065$  meV/atom,  $K_{p,\text{Co}} = 0.95$  meV/atom), red lines: prediction for 0.25 ML capped Co islands with Ag using  $K_{s,\text{Ag}} = 0.16$  meV/atom,  $K_{p,\text{Ag}} = -0.12$  meV/atom.

the overlayer is absent), reveals the negative sign of  $K_{s,\text{Ag}}$ , whereas the increase of  $T_b$  by full Ag capping indicates that the  $K_{s,\text{Ag}}$  is positive (see Fig. 6.7).

As discussed in the previous section, the best set of  $K$  values is obtained by simultaneously fitting the peaks in  $\chi'(T)$  and  $\chi''(T)$  observed in pure Co core and Co core - Ag decorated islands. With this procedure we find  $K_{s,\text{Co}} = 0.065 \pm 0.01$  meV/atom,  $K_{p,\text{Co}} = 0.95 \pm 0.05$  meV/atom, and  $K_{s,\text{Ag}} = 0.16 \pm 0.02$  meV/atom,  $K_{p,\text{Ag}} = -0.12 \pm 0.03$  meV/atom (Fig. 6.6 red lines). The errors bars in the  $K_s$  and  $K_p$  were derived by investigating the effect of small changes around the optimum values that can still reproduce the position of the  $T_b$  peaks and the shape of the experimental  $\chi'(T)$  and  $\chi''(T)$ .

The  $K_{s,\text{Ag}} = 0.16 \pm 0.02$  meV/atom is in great agreement with literature.  $K_{s,\text{Ag}} = 0.145$  meV/atom has been reported for Ag/Co interface in Ag/Co/Pt thin films grown on  $7 \times 7$  - Si(111) surface [198, 199] and to explain the increase of coercive field of 5 ML Co grown on Pt(111) after capping with 1 ML of Ag [196]. Additionally, Ag capping of Co/Pd(111) contributes positively to the out-of-plane MAE of the Co film with  $K_{s,\text{Ag}} = 0.1$  meV/atom [203] and a  $K_{s,\text{Ag}} = 0.125$  meV/atom has been reported for Ag/Co multilayers [232].

The pure Co islands reverse their magnetization by CR up to a size of 1400 atoms while for bigger sizes the DW mechanism takes over (see in Fig. 6.8a). In a previous work on pure Co islands the crossover between the two reversal mechanisms has been reported for island sizes of 600 atoms [74]. This difference is related to the island shape. The islands produced by the current recipe have about twice the width and half the mean

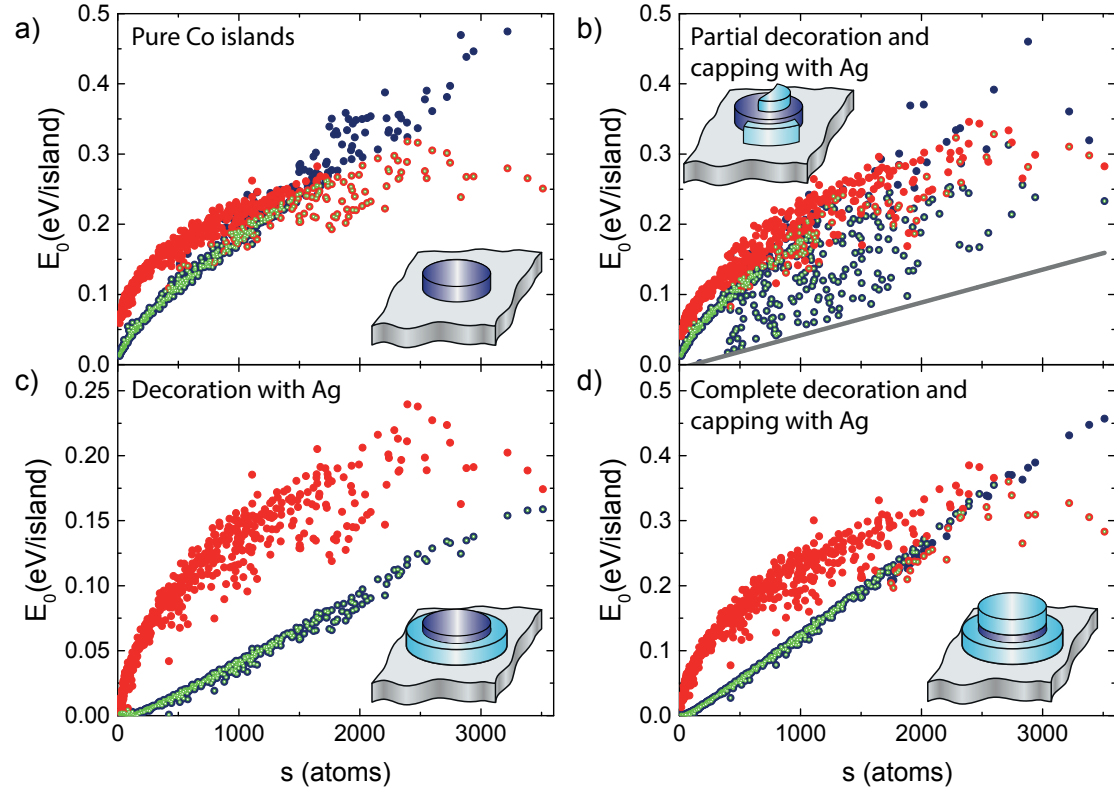


Figure 6.8 – Zero-field energy barriers  $E_0$  for a) pure Co islands, b) Co islands partially decorated and capped with Ag, c) prediction for complete decoration with Ag without capping, d) complete decoration and capping with Ag. Blue symbols indicate  $E_0$  values calculated with the CR, red the DW reversal mechanism for each island. Light green: lowest energy produced from one of the reversal mechanisms for all islands, gray line: linear regression of CR from c).

size compared with the ones in the previous work. Hence, the majority of the islands have a more compact shape which pushes the activation of the DW to larger island sizes than in the previous work. The partial decoration and capping with Ag reduces the  $E_0$  for DW model which dominates as reversal mechanism in the island ensemble. The energy scattering in Fig. 6.8b is generated by the many different combinations of Ag (partial) decoration length, islands size and Ag capping overlayer. Fig. 6.8c shows that a complete Ag decoration is expected to decrease the energy of the islands for the CR model, while it does not affect so much the DW reversal model as for each island only two atoms from the perimeter are contributing to the  $W_z$ . In Fig. 6.8b it is shown for comparison the linear regression (gray line) for the CR model for complete Ag decoration from c). The islands with energies closer to the line fit are mainly fully decorated rather than capped with Ag. Full Ag capping increases the reversal energies associated to both models and thus pushes the crossover between the two reversal mechanisms to bigger island sizes at about 1750 atoms (Fig. 6.8d). This implies a higher  $T_b$  for Ag capped islands as confirmed by the experimental data on small Co islands (0.14 ML).

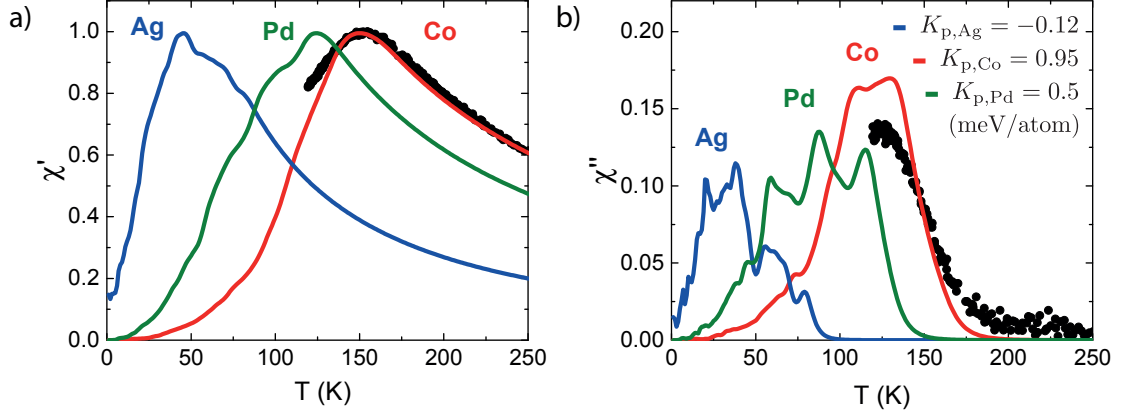


Figure 6.9 – Experimental and simulated zero-field susceptibility curves for islands of Co core and prediction susceptibility curves for complete decoration with Ag and Pd. The external field has been applied perpendicular to the sample surface. Black symbols: experimental data for pure Co islands 0.25 ML. Red lines: simulation curves with  $K_{s,Co} = 0.065$  meV/atom,  $K_{p,Co} = 0.95$  meV/atom. Blue lines: prediction for complete decoration of Co islands by Ag,  $K_{p,Ag} = -0.12$  meV/atom. Green lines: prediction for complete decoration of Co islands by Pd using  $K_{p,Pd} = 0.5$  meV/atom (value from [63]).

After capping the  $T_b$  is shifted by more than 25 K, with the exact value that could not be measured because the  $T_b$  of pure Co islands is below our instrumentation limit (see Fig. 6.7b). In the same figure it is shown the simulation curves for 0.25 ML pure Co islands and the prediction for full Ag capping (Fig. 6.7 gray and red lines). The increased energies in both reversal models and the shift in the crossover island size, as we show in previous Fig. 6.8d, for simulated Ag capping justifies the increase in  $T_b$  compared to pure Co islands. In this case the change in  $T_b$  is smaller:  $\Delta T_b = 17 \pm 3$  K. This difference compared to the small Co islands case can be explained by the difference in island shape and size which activates different reversal mechanism.

In order to understand the effect on  $T_b$  of a complete decoration with Ag, a prediction analysis for a complete Co/Ag interline was simulated for 0.25 ML Co islands using anisotropy coefficients values reproducing the  $\chi(T)$  curves for both Co and Ag decorated islands simultaneously. A one-atom Ag shell was found to reduce the  $T_b$  of pure Co islands of about 100 K (see in Fig. 6.9, blue lines). The same analysis was performed for a one-atom rim of Pd using the value found by Ouazi *et al.* [63]  $K_{p,Pd} = 0.5$  meV/atom (see Fig. 6.9 green lines). In this case  $T_b$  reduces by about 25 K. This comparison illustrates that a Co/Ag interline cannot work as a passivating rim between Co island edges and a Pd interline, as it reduces  $K_{p,Co}$  by 0.62 meV/atom more than a Co/Pd interline does.

## 6.6 Co/Pd Interface

The  $\text{Co}_x\text{Pd}_{1-x}$  alloys [195, 233–236] and Co/Pd multilayers [200, 201, 203, 237] have been extensively studied over the years due to their great potential for being used as magnetic medium in magnetic media. Recently, two-dimensional nanoislands with a Co core decorated and capped with Pd highlighted the different role played by Co/Pd interface and interline. In particular, it has been found that the Co/Pd interface contributes to the magnetization reversal energy by  $E_{\text{if,Co-Pd}} = 0.38 \pm 0.04$  meV/atom, in agreement with calculated value for Pd/Co/Pd(111) [201], while for the interline was found  $E_{\text{il,Co-Pd}} = 0.5 \pm 0.04$  meV/atom. However, in this previous work the magnetization reversal process has not been discussed. Here, with the help of new data, we show that Co islands capped with Pd mainly reverse their magnetization by DW.

One of the most important parameters in the DW model is the exchange stiffness  $A$ . The higher the  $A$  the thicker the domain wall, the larger the energy needed to form the DW for the same anisotropy energy coefficients (see Fig. 6.11a). The hybridization at the Co/Pd interface induces the polarization of Pd. The induced magnetic moment of Pd contributes to the DW energy via the interface magnetocrystalline anisotropy and the Co-Pd exchange stiffness  $A_{\text{Co-Pd}}$ . We note that an additional exchange stiffness  $A_{\text{Pd-Pd}}$  nominally should be considered in the simulation. Due to its small value coming from the reduced Pd moments compared to Co it was omitted for simplicity and instead, was considered incorporated to  $A_{\text{Co-Pd}}$ . The sketch of DW in an island cross section in Fig. 6.10 illustrates the exchange between Pd-Pd, Co-Pd and Co-Co atoms.

Since the exchange stiffness of pure Co islands is reduced due to low dimensionality [67] we expect the same effect in the exchange stiffness for Co-Pd. Former calculations on  $\text{Co}_2\text{Pd}_4$  subsequent films have reported an  $A_{\text{eff}} = 2$  pJ/m [238]. Accordingly, experimental work on  $\text{Co}_2\text{Pd}_5$  multilayers has shown an  $A_{\text{eff}} = 4$  pJ/m [239]. Both theoretical and experimental works suggest that  $A_{\text{Co-Pd}}$  is at least three times smaller the value used

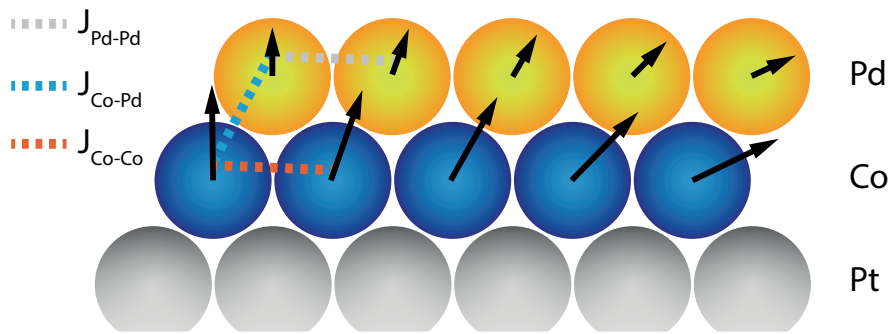


Figure 6.10 – Cross-section schematic of a Co island on Pt(111) capped by Pd. Gray, blue and orange dashed lines represent the exchange interaction between Pd-Pd, Co-Pd and Co-Co atoms, respectively. Arrows represent the atom magnetic moments, (in Pd represents the induced polarization due to the hybridization with the Co atoms).

for  $A_{\text{Co-Co}}$  in our simulations for the case of pure Co islands.

In addition to the exchange stiffness  $A$ , the surface magnetic anisotropy coefficient  $K_s$  affects the energy of the DW model. For fixed  $K_{\text{p,Pd}} = 0.5 \pm 0.04$  meV/atom,  $A_{\text{Co-Co}} = 15$  pJ/m and  $A_{\text{Co-Pd}} = 3$  pJ/m, fig. 6.11b illustrates the dependence of the DW reversal energy on  $K_{\text{s,Pd}}$ . For comparison, simulated DW energies for the same island sizes are shown in Fig. 6.11a with  $K_{\text{s,Pd}}$  and  $K_{\text{p,Pd}}$  fixed and a varying  $A_{\text{Co-Pd}}$ . The selection of a small  $A_{\text{Co-Pd}}$  requires a higher  $K_s$  to compensate the DW energy in order to reproduce the  $T_b$  of the island ensemble and *vice versa*. As one can see, the DW energy is more sensitive to the  $A_{\text{Co-Pd}}$  value below 3 pJ/m while for higher values the DW is only slightly affected.

The total coverage of pure Co islands for this section has been intentionally reduced to  $\Theta_{\text{Co,total}} = 0.18$  ML, by depositing only  $\Theta_{\text{Co}} = 0.08$  ML in the second step of the growth process, in order to produce islands with the same density and a smaller mean size of 870 atoms. The island size reduction is required in order to keep the island blocking temperature, after full Pd capping, below the limit of 375 K, at which irreversible alloying at the Co/Pt interface takes place [221].

The pure Co islands ( $\Theta_{\text{Co,total}} = 0.18$  ML) have approximately  $T_b = 80$  K (see Fig. 6.12b) which is essentially lower than the value observed for  $\Theta_{\text{Co,total}} = 0.25$  ML. The intensity of the reflected laser light after capping the pure Co islands with 1 ML of Pd is reduced in our measurements by a factor of three. The experimental  $\chi(T)$  curves after the Pd capping in Fig. 6.12a-d have been normalized to the  $\chi(T)$  signal of pure Co islands. The experimental data for pure Co islands are well reproduced by using  $K_{\text{s,Co}} = 0.065$  meV/atom and  $K_{\text{p,Co}} = 0.95$  meV/atom and both reversal mechanisms. The zero-field energy barrier  $E_0$  distribution highlights that only CR reversal process is activated as is shown in red dots in Fig. 6.12e (except a very few cases of islands larger than 1400 atoms which DW).

The capping of pure Co islands with Pd shifts  $T_b$  to 330 K. Simulation of the susceptibility curves using both reversal mechanisms, with fixed  $K_{\text{p,Pd}} = 0.5$  meV/atom,  $A_{\text{Co-Co}} = 15$  pJ/m and with varying  $K_{\text{s,Pd}}$  (0.8 - 1.0 meV/atom) and  $A_{\text{Co-Pd}}$  (0.75 - 1.5 pJ/m) are shown in Fig. 6.12a and b (blue, orange and green lines). Three different combinations of  $K_{\text{s,Pd}}$  and  $A_{\text{Co-Pd}}$  match the experimental peak in  $\chi''(T)$ . Among the three combinations the one with  $A_{\text{Co-Pd}} = 0$  J/m (blue line) reproduces better both experimental curves. The absence of the exchange interaction between Co and Pd atoms is unrealistic since there is an induced magnetic moment from the Co-Pd hybridization.

In the other two cases (orange and green lines), an increase of  $A_{\text{Co-Pd}}$  produces a broadening of the  $\chi(T)$  peaks. We note also that during the course of the simulations  $K_{\text{s,Pd}} = 0.4$  meV/atom from Ref. [63, 201] was tested for  $A_{\text{Co-Pd}}$  values up to 15 pJ/m (as if Pd was Co) but the simulations always resulted in much lower  $T_b$  peaks and broad curves (not shown). The reversal energy distribution has changed after the complete Pd

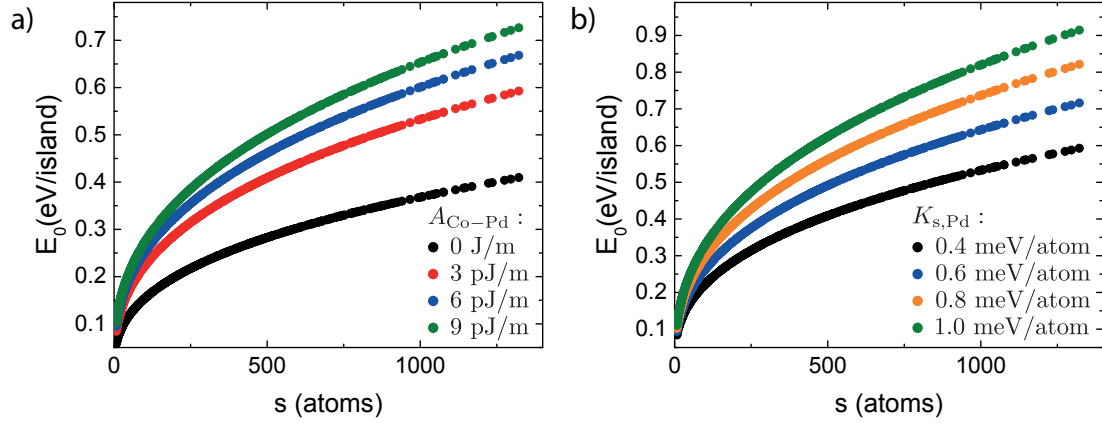


Figure 6.11 – Simulated zero-field energy barriers  $E_0$  for 0.18 ML Co islands capped with Pd using the DW reversal model. a) Fixed magnetic anisotropy energy ( $K_{p,Pd} = 0.5$  meV/atom,  $K_{s,Pd} = 0.4$  meV/atom),  $A_{Co-Co} = 15$  pJ/m and varying  $A_{Co-Pd}$ . Black line:  $A_{Co-Pd} = 0$  J/m, red line:  $A_{Co-Pd} = 3$  pJ/m, blue line:  $A_{Co-Pd} = 6$  pJ/m, green line:  $A_{Co-Pd} = 9$  pJ/m. b) Fixed  $K_{p,Pd} = 0.5$  meV/atom,  $A_{Co-Co} = 15$  pJ/m,  $A_{Co-Pd} = 3$  pJ/m, and varying  $K_{s,Pd}$ . Black line:  $K_{s,Pd} = 0.4$  meV/atom, blue line:  $K_{s,Pd} = 0.6$  meV/atom, orange line:  $K_{s,Pd} = 0.8$  meV/atom, green line:  $K_{s,Pd} = 1.0$  meV/atom.

capping for all presented combinations of  $K_{s,Pd}$  and  $A_{Co-Pd}$ . DW mechanism always dominates for islands bigger than about 700 atoms. However, the large broadening in the  $\chi(T)$  curves is due to the small island reversing their magnetization by CR. In cases of pure Co islands where  $K_p \gg K_s$ , the  $\chi(T)$  peaks are quite narrow. For island sizes larger than the crossover point, DW sets in and the energy needed to switch saturates as the island size increases and thus, the islands in this region switch much easier than if they were in CR. This saturation leads to sharper peaks than when CR is activated. Apparently DW reversal sets in for a smaller portion of the island ensemble, and thus this broadening of the curves is observed.

In the CR model the exchange stiffness it is not present because the magnetic moments of all constituent atoms in the island stay aligned during the entire reversal process ( $A$  is considered infinite). Therefore, the islands after the Pd capping are still considered as pure Co islands but with different  $K_s$  and  $K_p$  parameters and without taking into account the contribution of the atoms located on the second layer. Our approach for the CR model is quite simplistic. In a more complex CR model one would include an additional parameter which comprises the contribution originating from the capping of a polarized element to the energy. In that case the  $E_{CR}$  is increased for every island size and thus it is possible for the DW to be more favorable in a wider range of island sizes. For this reason we investigated the special case where only DW reversal mechanism is activated with fixed  $K_{p,Pd} = 0.5$  meV/atom and varying  $K_{s,Pd}$  (0.45 - 0.95 meV/atom) and  $A_{Co-Pd}$  (0.15 - 12 pJ/m). In Fig. 6.12c-d we show four examples of different combinations of



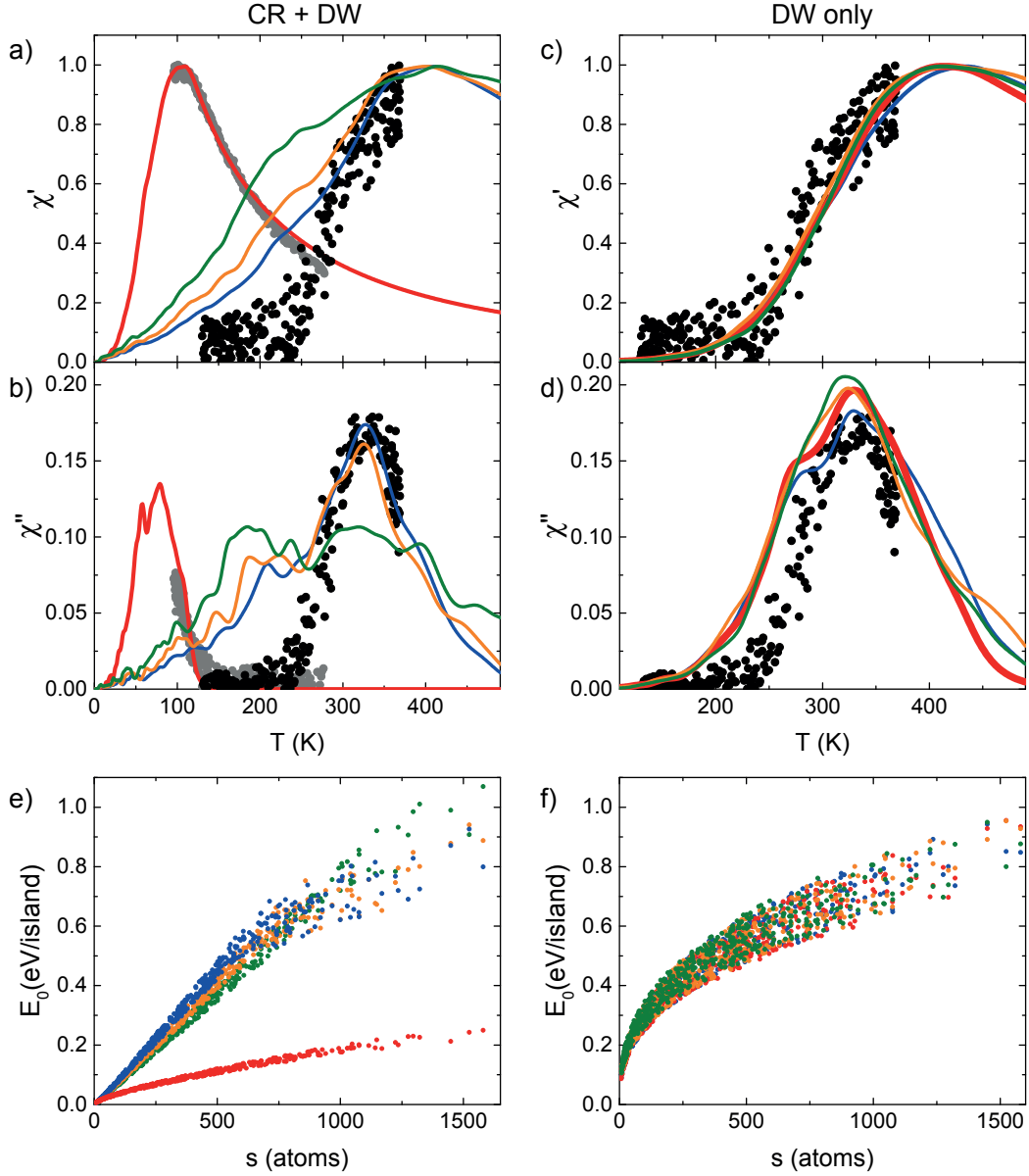


Figure 6.12 – Out-of-plane zero-field susceptibility curves for 0.18 ML pure Co islands and capped with 1 ML Pd (a-d). Symbols represent experimental data (gray) for pure Co islands and (black) Co islands capped with Pd. Continuous curves represent simulation using a-b) CR and DW models, c-d) DW only. In all cases  $K_{p,Pd} = 0.5$  meV/atom,  $A_{Co-Co} = 15$  pJ/m. a-b) Red lines: simulation curves for pure Co islands ( $K_{s,Co} = 0.065$  meV/atom,  $K_{p,Co} = 0.95$  meV/atom). Blue lines:  $K_{s,Pd} = 1.0$  meV/atom,  $A_{Co-Pd} = 0.75$  pJ/m; orange lines:  $K_{s,Pd} = 0.9$  meV/atom,  $A_{Co-Pd} = 1.5$  pJ/m, green lines:  $K_{s,Pd} = 0.8$  meV/atom,  $A_{Co-Pd} = 1.5$  pJ/m. c), d) Blue lines:  $K_{s,Pd} = 0.95$  meV/atom,  $A_{Co-Pd} = 1.5$  pJ/m, red lines:  $K_{s,Pd} = 0.75$  meV/atom,  $A_{Co-Pd} = 3$  pJ/m, orange lines:  $K_{s,Pd} = 0.6$  meV/atom,  $A_{Co-Pd} = 6$  pJ/m, green lines:  $K_{s,Pd} = 0.45$  meV/atom,  $A_{Co-Pd} = 12$  pJ/m. Zero-field energy barriers  $E_0$  for pure Co island (red dots) and Co islands capped with Pd using e) the lowest energy value either from CR or DW reversal models and f) solely DW.

$K_{s,\text{Pd}}$  and  $A_{\text{Co-Pd}}$  that match  $T_b$  and reproduce the experimental susceptibility curves. These sets give identical zero-field energy barriers (see in Fig. 6.12f). One can safely exclude the case with  $K_{s,\text{Pd}} = 0.45$  meV/atom, because the used  $A_{\text{Co-Pd}} = 12$  pJ/m is very close to Co-Co exchange interaction. By considering the previous reported experimental value  $A_{\text{eff}} = 4$  pJ/m [239] we can also exclude the case  $A_{\text{Co-Pd}} = 6$  pJ/m. The case for  $A_{\text{Co-Pd}} = 1.5$  pJ/m can be considered as the lowest limit as this value is close to the theoretical value reported for Co-Pd exchange stiffness [238]. We note  $K_{s,\text{Pd}} = 0.95$  meV/atom in this combination is more than two times larger than the best reported value in literature [200].

The value of  $A_{\text{Co-Pd}} = 3$  pJ/m is very close to former experimental result [239] for Co/Pd interface.  $K_{s,\text{Pd}} = 0.75$  meV/atom in this case is about two times larger the highest value reported for Pd/Co/Pd(111) [200, 201]. In these cases the most important contribution to the out-of-plane MAE comes mainly from  $d_{xy}$  and the  $d_{x^2-y^2}$  states which are close to the Fermi level. The hybridization at the interface brings these states at the Fermi level and their contribution to the anisotropy energy is enhanced by the large Pd spin-orbit interaction [240, 241]. However, in our case one has to consider two different interfaces, one between Co and the Pt substrate and one between Pd and Co generated by the capping. The induced polarization of Pd could be larger with respect to the one from Pd/Co/Pd interface due to a different level of the hybridization of Co with the Pt(111) substrate. More specifically in this double interaction, the latter hybridization may have increased the energy split between the  $d_{xy}$  and the  $d_{x^2-y^2}$  states which contribute to the out-of-plane magnetization, resulting in an even higher MAE than from the actual Co/Pd interface. This lift of the degeneracy of the two bands, which happens at the "hot spots" in the band structure, has been already shown in FeCo submonolayer island alloys [63] but also for FeCo bulk alloys [242]. Unfortunately, up to this date single sequences or multilayers made of Pd/Co/Pt(111) have not been studied and thus, we cannot verify this  $K_{s,\text{Pd}} = 0.75$  meV/atom value only by the susceptibility simulation analysis. However, we strongly believe that  $K_{s,\text{Pd}}$  is close to this value due to the increased polarization of Pd at the Co/Pd interface, which shifts the  $T_b$  of pure Co islands above room temperature.

### 6.7 Co/Rh Interline and Interface

Rh, as Pd, is a highly polarizable element, which shows a significant magnetic moment when it hybridizes with a magnetic element. Formerly, a strong hybridization between Co (Fe) layers and the supporting surface Rh(111) has been reported [215]. In addition, an oscillatory dependence of the orientation of the magnetization easy axis as a function of Co film thickness has been found. Rh has been also used as a spacer, mediating an exchange coupling between two ferromagnetic layers, as Co, which couples ferromagnetically or anti-ferromagnetically, depending on the Rh thickness [243]. Due to its exchange coupling, Rh has been predicted in a previous study to induce a large in-plane MAE when capping three layers of Co grown on Pd(111) [201]. This indicates an induced magnetic moment



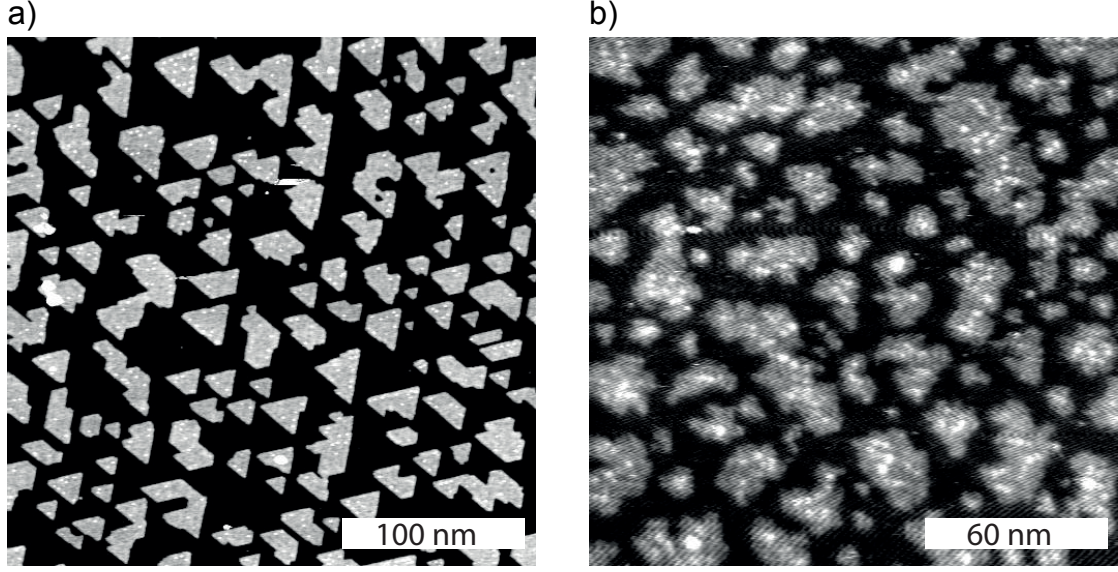


Figure 6.13 – a) Co 0.32 ML (0.1 ML at 130 K and subsequently 0.22 ML at  $T_{\text{dep}} = 280$  K) ( $V_t = -0.3$  V,  $I_t = 1$  nA), b) Co 0.32 ML (same growth recipe as in a), 0.07 ML Rh decoration, deposited at  $T_{\text{dep}} = 350$  K ( $V_t = -1.1$  V,  $I_t = 1$  nA).

in the Rh layer close to the Co/Rh interface. Evidently, Rh is anticipated to polarize strongly with Co islands when it hybridizes either at the interface or in the perimeter.

Preliminary experiments for the lateral decoration of 0.25 ML of pure Co islands with Rh, had shown a significant reduction in  $T_b$  after the decoration, pinpointing to a negative  $K_{p,\text{Rh}}$ . The peaks for both  $\chi(T)$  curves were well below the temperature measuring limit of our setup after the decoration with 0.07 ML Rh. We decided to increase the mean island size of the islands while maintaining the same density by increasing the coverage in the second deposition step to  $\Theta_{\text{Co}} = 0.22$  ML in order to shift the  $T_b$  to a higher temperature. The total Co coverage was increased to  $\Theta_{\text{Co,total}} = 0.32$  ML with an island mean size of 1600, a representative STM topography can be seen in Fig. 6.13a. Above this coverage islands start to coalesce (see Fig. 2.3a). Consequently, the susceptibility curves will significantly change in shape and the  $T_b$  will shift to a much larger temperature. The  $T_b$  of the ensemble of 0.32 ML pure Co islands has shifted approximately to 140 K.

During the experiments relating to the decoration and the capping of pure Co islands with Rh we encountered a thermal drift in the acquisition of the signal in the susceptibility measurements. This thermal drift induced a non-physical displacement of the  $\chi''(T)$  peak to the right-hand side with respect to the peak in  $\chi'(T)$  and a  $\chi'(T)$  decrease at high temperature much steeper than  $1/T$  (Fig. 6.14a and b). To compensate for the thermal drift we applied a linear correction to the  $\chi(T)$  curves. In all the cases the method was applied, all correction parameters were the same, ensuring its proper use. To test the accuracy of our method we fitted the susceptibility curves for an ensemble

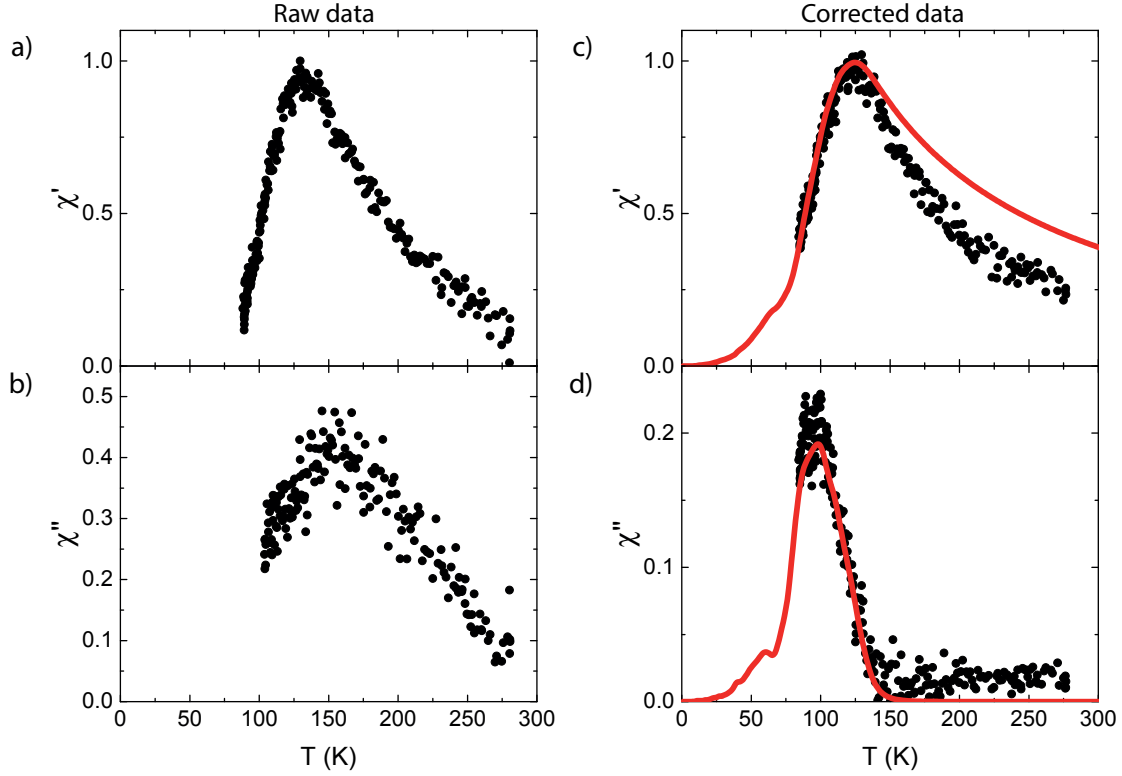


Figure 6.14 – Zero-field susceptibility measurements of a), b) 0.22 ML pure Co islands raw data and c), d) corrected data (black symbols) and simulation curves (red lines) with  $K_{s,\text{Co}} = 0.06$  meV/atom,  $K_{p,\text{Co}} = 0.9$  meV/atom.

of pure Co island affected by the thermal drift. The simulated curves reproduced the corrected experimental data accurately using the  $K_{p,\text{Co}}$  and  $K_{s,\text{Co}}$  values determined in the previous sections. The results are shown in Fig. 6.14c, d and Fig. 6.15a, b for 0.22 ML and for 0.32 ML Co islands, respectively. This method was used additionally to derive the actual experimental curves for the decoration and capping with Rh.

Rh decorates completely the Co islands, for the coverage  $\Theta_{\text{Rh}} = 0.07$  ML. The Rh deposition at  $T_{\text{dep}} = 350$  K creates a rim around pure Co islands of irregular shape but without nucleating on top of the islands (see Fig. 6.13b). The small portion in the second layer is Co which starts to appear a few hours after the Co deposition. The same effect is shown in Fig. 6.13a for pure Co, which was taken hours after the deposition because of the priority of acquisition of the magnetic measurements.

In the susceptibility measurements we observed that even the use of increased Co coverage does not suffice to reveal the  $T_b$  after the decoration with Rh (see Fig. 6.15a and b). For this reason the most suited  $K_{p,\text{Rh}}$  value was derived from the simulation curves that reproduce best the  $\chi'(T)$  experimental points and simultaneously, the onset for the  $\chi''(T)$  signal. In the simulation we used both reversal mechanisms with  $K_{s,\text{Co}} = 0.065$  meV/atom

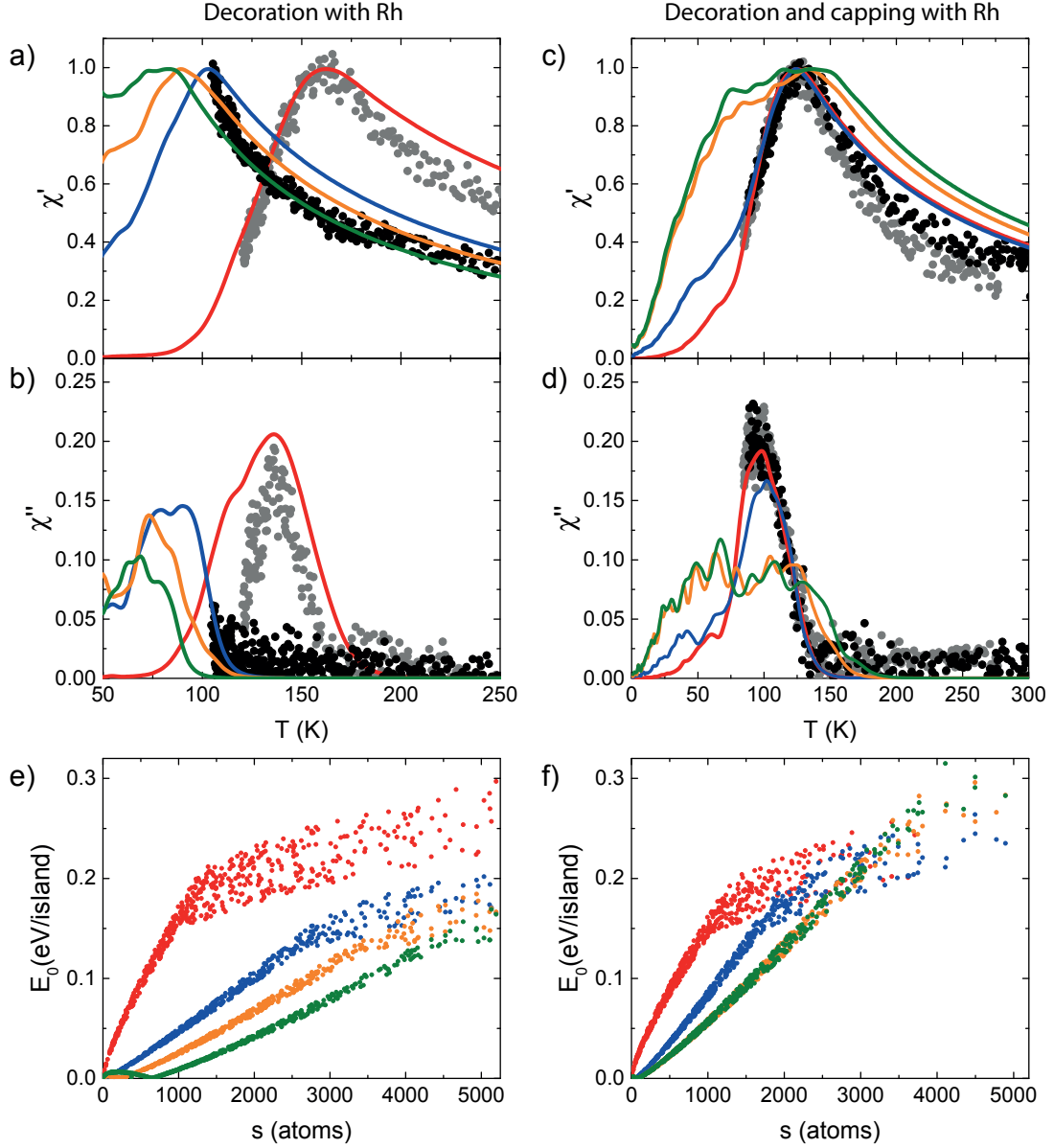


Figure 6.15 – Out-of-plane zero-field susceptibility for experimental and simulated curves using CR and DW reversal mechanisms for 0.32 ML Co islands decorated with Rh (a, b) and 0.22 ML Co capped with Rh (c, d). a-d) Gray symbols: experimental data for pure Co islands, red lines: simulation curves for pure Co islands with  $K_{s,\text{Co}} = 0.065$  meV/atom,  $K_{p,\text{Co}} = 0.95$  meV/atom. a-b) Black symbols: Co islands decorated with Rh, blue lines:  $K_{p,\text{Rh}} = -0.1$  meV/atom, orange lines: simulation curves with  $K_{p,\text{Rh}} = -0.3$  meV/atom and green lines:  $K_{p,\text{Rh}} = -0.45$  meV/atom. c), d) Black symbols: Co islands capped with Rh. Simulation curves produced with fixed  $K_{p,\text{Rh}} = -0.3$  meV/atom and different combinations of  $K_{s,\text{Rh}}$  and  $A_{\text{Co-Rh}}$ . Blue lines:  $K_{s,\text{Rh}} = 0.13$  meV/atom and  $A_{\text{Co-Rh}} = 0$  J/m, orange lines:  $K_{s,\text{Rh}} = 0.10$  meV/atom and  $A_{\text{Co-Rh}} = 1.5$  pJ/m, green lines:  $K_{s,\text{Rh}} = 0.10$  meV/atom and  $A_{\text{Co-Rh}} = 3$  pJ/m. e) Zero-field energy barriers  $E_0$  for the decorated Co islands with Rh using the mentioned  $K_{p,\text{Rh}}$  values and f) for Rh capping using the  $K_{s,\text{Rh}}$  and  $A_{\text{Co-Rh}}$  from c), d).

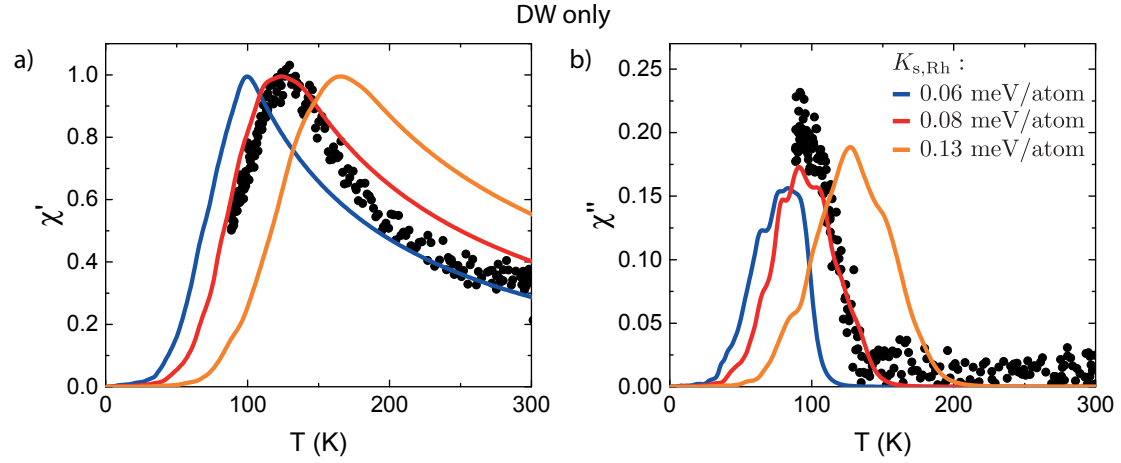


Figure 6.16 – Out-of-plane zero-field susceptibility for experimental and simulated curves using only DW reversal mechanism for Co islands capped with Rh. Black symbols: Co islands capped with 1 ML Rh. Simulation curves produced with fixed  $K_{p,Rh} = -0.3$  meV/atom,  $A_{Co-Rh} = 1.5$  pJ/m and varying  $K_{s,Rh}$ . Blue lines:  $K_{s,Rh} = 0.06$  meV/atom, red lines:  $K_{s,Rh} = 0.08$  meV/atom and orange lines:  $K_{s,Rh} = 0.13$  meV/atom.

for the Co surface atoms and  $K_{p,Rh}$  as free parameter. Three  $\chi(T)$  curves can be seen for three different values of  $K_{p,Rh}$  in Fig. 6.15a and b. Following our criterium the best fit is obtained with  $K_{p,Rh} = -0.3$  meV/atom. Co/Rh interline strongly affects the out-of-plane MAE of Co perimeter atoms and consequently the island magnetization reversal process. This effect can be seen in zero-field energy barriers. Before decoration, the crossover between CR and DW for pure Co islands is located approximately at the island size of 1100 atoms. The decoration of Co shifts the crossover to island sizes of about 3500 atoms for the selected  $K_{p,Rh} = -0.3$  meV/atom (see Fig. 6.15e). This occurs because CR model is more sensitive to the perimeter atoms than DW.

The complete capping with Rh demonstrates that the contribution from the Co/Rh interface compensates the negative interline effect as  $T_b$  remains unchanged, with respect to the pure Co case, after deposition of 1 ML Rh. Thus, the Co/Rh interface contributes positively to the out-of-plane MAE of pure Co islands. Rh like Pd is a highly polarizable element and thus, for the derivation of the anisotropy coefficient for the Co/Rh interface, the exchange stiffness for Co-Rh was implemented in the simulation model. For the investigation of the  $K_{s,Rh}$  coefficient we used CR-DW model with  $K_{p,Rh} = -0.3$  meV/atom fixed and varying  $A_{Co-Rh}$ . In Fig. 6.15c-d are shown three  $\chi(T)$  curves obtained for different combinations of  $A_{Co-Rh}$  and  $K_{s,Rh}$ .  $K_{s,Rh} = 0.13$  meV/atom gives the best fit but the used exchange stiffness is zero. This case can be safely excluded as it refers to the absence of Rh polarization at the interface. For the other two cases, increasing  $A_{Co-Rh}$  and decreasing  $K_{s,Rh}$  leads to very broad peaks, which do not follow the  $\chi(T)$  curves.

Finally, in order to investigate the effect coming only from DW, we performed a simulation analysis for a range of  $A_{\text{Co-Rh}}$  between 1 and 4 pJ/m,  $K_{\text{p,Rh}} = -0.3$  meV/atom and varying  $K_{\text{s,Rh}}$ . Higher  $A_{\text{Co-Rh}}$  values generate curves which are not consistent with the experimental data. The best fit is obtained with  $A_{\text{Co-Rh}} = 1.5$  pJ/m. For this value we show three  $\chi(T)$  curves in Fig. 6.16. For  $K_{\text{s,Rh}} = 0.08$  meV/atom the simulated curves are in good agreement with the experimental data. This value is about one order of magnitude larger than the one reported previously with  $K_{\text{s}}$  of Co/Rh interface for multilayer grown on Rh(111) buffer layer [202].

## 6.8 Multilayer Pd Capping of Co islands

The complete capping of pure Co islands by a single layer of Pd has yielded the largest shift in  $T_{\text{b}}$  from all studied  $4d$  elements in line with the work of Ouazi *et al.* [63]. Previous studies on ultrathin films have shown that more than one single Pd layer is required to maximize the perpendicular magnetic anisotropy of the Co/Pd interface [203, 204]. Therefore, we investigated how the Pd multilayer thickness affects the blocking temperature of nanostructures with lower atom coordination than thin films. For this study we considered 0.25 ML pure Co islands, as function of Pd layer number.

During this study, Co islands were grown as previously described in section 6.2 producing  $T_{\text{b}} = 109 \pm 6$  K and thereafter, were capped with four subsequent Pd monolayers. For each additional Pd capping, susceptibility measurements were taken. The first Pd layer

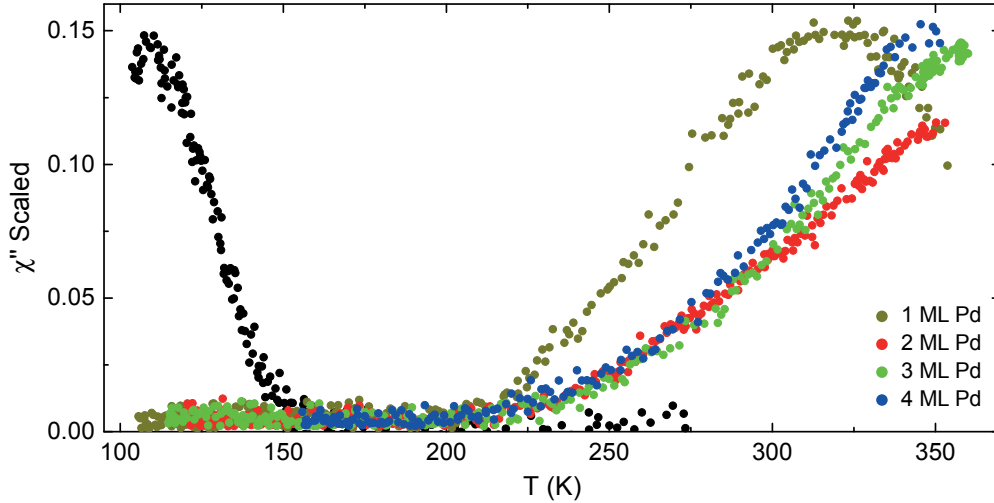


Figure 6.17 – Imaginary part of susceptibility  $\chi''(T)$  for 0.25 ML Co islands covered by four subsequent layers of Pd. Black symbols: 0.25 ML Co, dark green: 0.25 ML Co capped by one Pd layer, red: by two Pd layers, green: by three Pd layers and blue: by four Pd layers. Data from all capping Pd layers are normalized with the same parameters used for pure Co islands.



shifts the  $T_b = 321 \pm 5$  K, implying a  $\Delta T_b = 212 \pm 11$  K, as predicted before [63] and in agreement with results on section 6.6. The  $T_b$  for thicker Pd layer capping overcomes the measuring range for this system (see Fig 6.17). The interface mixing between Co and Pt starting at about 375 K gives a superior limit for the temperature in our measurements [221]. Due to this limitation we have to derive the highest  $T_b$  by the onset of the change in slope in the susceptibility signal. The curve starting to increase for last at higher temperatures, indicates the highest  $T_b$ . We note that for 2 to 4 ML of Pd capping, the correct normalization of the experimental data is impossible due to the lack of the peak in  $\chi''(T)$ . Since all data were acquired during the same experiment, the Pd capping curves were normalized with respect to the signal for pure Co islands in order to be used for comparison. As the Pd thickness increases the intensity of the light is expected to reduce further affecting the slope in the  $\chi''(T)$  curves. Hence, it is expected that the actual  $T_b$  would be higher than it is estimated from the current assumption. From the imaginary part of the susceptibility measurements it can be seen that  $T_b$  reaches its maximum value for a thickness of the Pd capping layer of about 2 ML. As the Pd layers increase the  $T_b$  is reducing, with four layers to reach  $350 \pm 5$  K. Former calculations on Co/Pd monolayers show that the magnetic moment induced in Pd survives for up to three monolayers [244, 245]. Consequently, one could expect a maximum in MAE for capping with three Pd monolayers and the MAE to remain constant for higher number of layers. Our observations partially agree with this expectation. In particular we observe a peak in MAE for capping with two Pd monolayers instead of three, in agreement with previous studies on Co/Pd thin films [203, 204]. In these studies MAE was found to maximize at about two layers of Pd capping and above this thickness the MAE reduces to a lower stationary value which is preserved for at least ten atomic layers.

## 6.9 Conclusions

We have studied the effect on the MAE produced by decorating and/or capping Co islands on Pt(111) by forming atomically sharp interlines and interfaces with three  $4d$  elements, namely Ag, Pd and Rh. For pure Co islands we found  $K_{s,Co} = 0.065 \pm 0.01$  meV/atom and  $K_{p,Co} = 0.95 \pm 0.05$  meV/atom. Ag was found to produce a partial decoration of the Co island edges and the anisotropy for the interline was found  $K_{p,Ag} = -0.12 \pm 0.03$  meV/atom. The complete Ag capping increases the out-of-plane MAE and generates an interface anisotropy of  $K_{s,Ag} = 0.16 \pm 0.02$  meV/atom in agreement with previous studies [196, 198, 199]. Capping with Pd strongly increases  $T_b$  with a shift to high temperatures of about 200 K. We report  $K_{s,Pd} = 0.75$  meV/atom for the Co/Pd interface using:  $K_{p,Pd} = 0.5$  meV/atom for Co/Pd interline, exchange stiffness  $A_{Co-Pd} = 3$  pJ/m and only the DW reversal mechanism. The capping with two Pd monolayers of pure Co islands has been found to maximize  $T_b$  in agreement with formerly reported studies on thin films [203, 204]. Rh decorates laterally Co islands forming a rim of irregular shape without nucleating on top of Co islands for the used deposition parameters. The Co/Rh interline

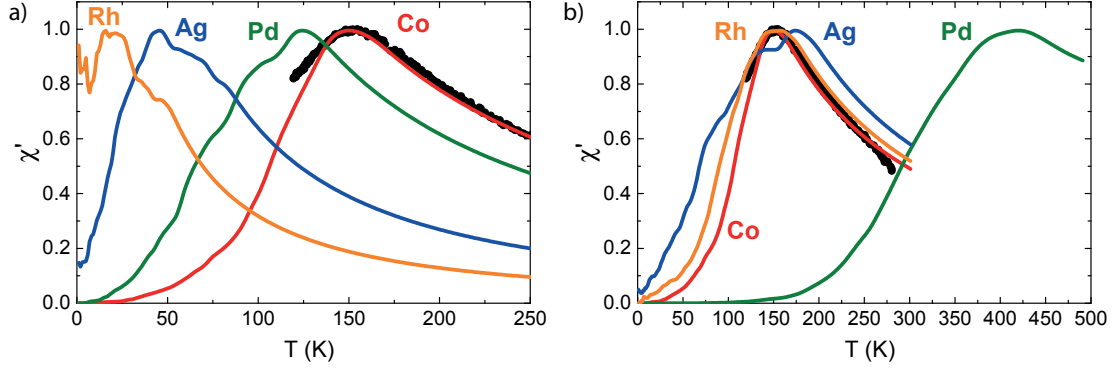


Figure 6.18 – Prediction curves of  $\chi'(T)$  for 0.25 ML Co islands a) decorated and b) capped with the studied  $4d$  elements. The curves have been calculated using the corresponding anisotropy coefficients previously derived. Black symbols: experimentally measured  $\chi'(T)$  for islands corresponding to 0.25 ML Co.

has been found to decrease the MAE of pure Co islands with  $K_{p,Rh} = -0.3$  meV/atom. The Co/Rh interface exhibits  $K_{s,Rh} = 0.08$  meV/atom by using  $A_{Co-Rh} = 1.5$  pJ/m and only DW reversal mechanism. The  $K_{s,Rh}$  is almost an order of magnitude larger than previous report on multilayers [202].





# 7 Nucleation and Growth of Rh/Pt(111)

In this chapter we present our results on the nucleation and growth of Rh/Pt(111), studied by means of STM. Rh becomes highly polarizable when hybridizes with a ferromagnetic element [194, 202] and in low coordinated configurations [246]. In a recent work on monolayer films of Co on Rh(111) [215], it was found that the interaction between Co adlayer and the substrate enhances spin and orbital moments and MAE of the Co adlayer. Moreover, Rh induced magnetic moments at the interface show strong ferromagnetic alignment with Co moments. Ouazi *et al.* [63] have shown the strong effect on the out-of-plane MAE of pure Co islands played by the formation of interfaces and interlines with other transitional metal elements. For example, an interline of Co/Fe increases the MAE by 70% compared to pure Co islands, whereas the lateral decoration of Co islands with Pd reduces the MAE by 60%. The lateral decoration of magnetic nanostructures made of Co core with Rh is expected to affect the MAE due to the strong ferromagnetic alignment of Rh with Co moments at the interline.

For a successful Rh decoration of pure Co islands grown on Pt(111), the diffusion parameters  $E_b$  and  $\nu_0$  for Rh on Pt(111) must be known. Since the nucleation and growth of Rh on Pt(111) has never been studied before, we performed nucleation and growth experiments in order to define the correct decoration recipe. For this reason, we focused in this part on the measurement of the island density as a function of the deposition temperature.

## 7.1 Experimental Procedure

Pt(111) crystal surface has been prepared before each experiment by three cycles of sputtering and annealing. More specifically, cycles of  $\text{Ar}^+$  ion sputtering were performed at room temperature and at 800 K, and subsequently exposed at the latter temperature to  $5 \times 10^{-8}$  mbar of  $\text{O}_2$  atmosphere for 10 minutes in order to reduce the C impurities on the surface. Finally, at the end of every cycle the crystal was annealed to 1300 K. The

base pressure in the UHV chamber is  $p_b \leq 6 \times 10^{-11}$  mbar. For the whole deposition and annealing temperature range used, the experiments were performed under liquid He flux in the cryostat, maintaining always the pressure lower than  $p = 7 \times 10^{-11}$  mbar. Rh has been evaporated from high purity rod (99.99%) using a commercial (Omicron) electron bombardment evaporator. Sample cooling to the desired deposition temperature requires some time, during which partial contamination of the Pt(111) surface may occur due to the residual gas. For this reason, the sample was degassed shortly by a flash annealing to 800 K before each deposition to ensure a perfectly clean surface. After Rh deposition the sample was cooled down in order to freeze surface diffusion and avoid post-deposition effects [175]. The sample morphology has been characterized by STM, operated always at the lowest measuring temperature of our setup (90 K), for more information see in Chapter 4. For each deposition temperature we have measured at least ten sets of STM topographies of opposite scan direction in order to compensate for the thermal drift in the slow scanning direction.

## 7.2 Island Nucleation

We investigated the nucleation of Rh/Pt(111) by measuring the island density as a function of deposition temperature  $T_{\text{dep}}$  for a Rh coverage  $\Theta_{\text{Rh}} = 0.12$  ML using  $F = 9 \times 10^{-4}$  ML/s, with one monolayer corresponding to one Rh atom per Pt(111) unit cell. For this coverage, the islands are within pure growth regime, where island coalescence is absent. The island density  $n_x$  is expressed in ML and is shown in the Arrhenius plot in Fig. 7.1a. In our analysis, only objects with apparent height larger than 50% of the apparent height of big Rh islands were considered as islands ( $200 \text{ \AA}^2$ ). Smaller clusters than this threshold were excluded as are most likely impurities on the surface appearing larger due to the tip-convolution of the STM.

The Arrhenius plot in Fig. 7.1a shows the island densities as a function of deposition temperature between 98 K and 500 K. Starting from  $T_{\text{dep}} = 98$  K the logarithm of the island densities decreases linearly up to 150 K. In the regime  $150 \text{ K} \leq T_{\text{dep}} \leq 250 \text{ K}$  the slope reduces dramatically and a sort of plateau is observed. For  $T_{\text{dep}} \geq 280 \text{ K}$  the  $\log(n_x)$  decreases linearly with a larger slope than in the first regime. In general, the appearance of a plateau between two decreasing regimes for island densities  $n_x$  is expected only for clusters growth on templates [50, 247]. An example is also shown in this thesis in Fig. 5.1a for Sm cluster nucleation on moiré pattern formed by graphene on Ir(111). This behavior is rather strange as in our case the island density should continuously decrease as the deposition temperature increases.

Considering all the data points valid in the plot we reasonable derive a regime with critical cluster size  $i = 1$  for  $98 \text{ K} \leq T_{\text{dep}} \leq 280 \text{ K}$  and  $i = 2$  for  $T_{\text{dep}}$  higher than 280 K, where the change in slope is evident (see Fig. 7.1a blue and red dashed lines). The change in slope between the two regimes corresponds to the onset for cluster diffusion due to the

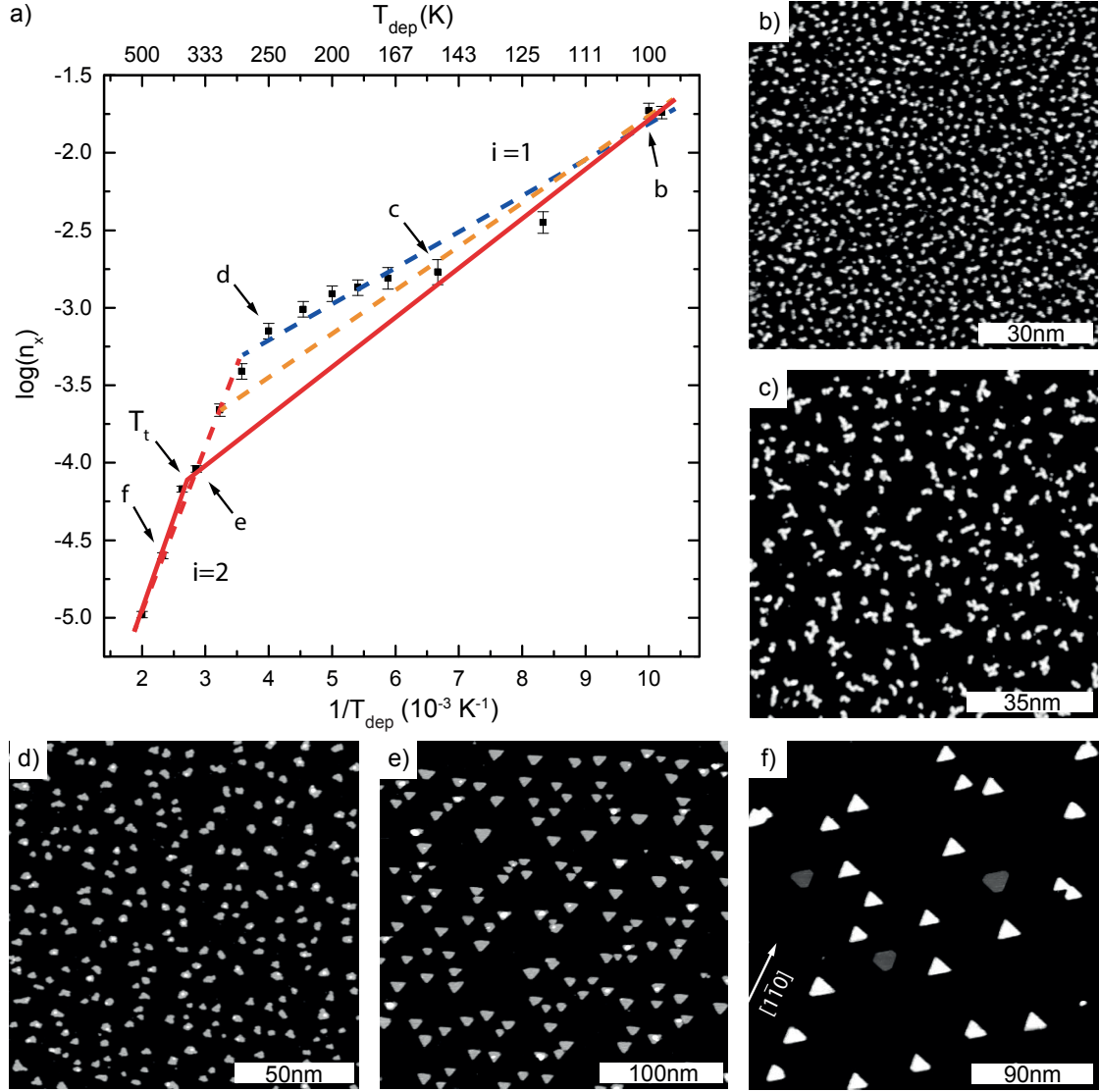


Figure 7.1 – a) Arrhenius plot of the Rh island density  $n_x$  as a function of deposition temperature  $T_{\text{dep}}$  for  $\Theta_{\text{Rh}} = 0.12$  ML and  $F = 9 \times 10^{-4}$  ML/s. Black symbols: experimental island densities measured from the STM topographies. Blue dashed line: linear regression including all the island densities in the range  $98 \text{ K} \leq T_{\text{dep}} \leq 280 \text{ K}$ . Orange dashed line: linear regression for  $T_{\text{dep}} \leq 150 \text{ K}$  and  $T_{\text{dep}} = 310 \text{ K}$ . Red lines: linear regression of the experimental points  $98 \text{ K} \leq T_{\text{dep}} \leq 150 \text{ K}$  and  $T_{\text{dep}} \geq 380 \text{ K}$  for critical cluster size  $i = 1$  and  $i = 2$ , respectively.  $T_t = 360 \text{ K}$  is the transition temperature between the two regimes. b) - f) STM topographies of Rh/Pt(111). b)  $T_{\text{dep}} = 100 \text{ K}$ , small single layer islands ( $V_t = -0.8 \text{ V}$ ,  $I_t = 1 \text{ nA}$ ). c)  $T_{\text{dep}} = 150 \text{ K}$ , single layer islands of ramified shape. ( $V_t = -0.6 \text{ V}$ ,  $I_t = 1 \text{ nA}$ ). d)  $T_{\text{dep}} = 250 \text{ K}$ , islands become compact in shape, a small fraction of second layer is grown. ( $V_t = -0.8 \text{ V}$ ,  $I_t = 1 \text{ nA}$ ). e)  $T_{\text{dep}} = 350 \text{ K}$ , islands have trigonal compact shape ( $V_t = -1.0 \text{ V}$ ,  $I_t = 1 \text{ nA}$ ). f)  $T_{\text{dep}} = 430 \text{ K}$ , 1 ML-high islands have rounded corners and are less than 10% of the ensemble, 2 ML-high islands have opposite orientation with sharp corners. The arrow indicates the step direction of the Pt(111) substrate ( $V_t = -1.2 \text{ V}$ ,  $I_t = 1 \text{ nA}$ ).

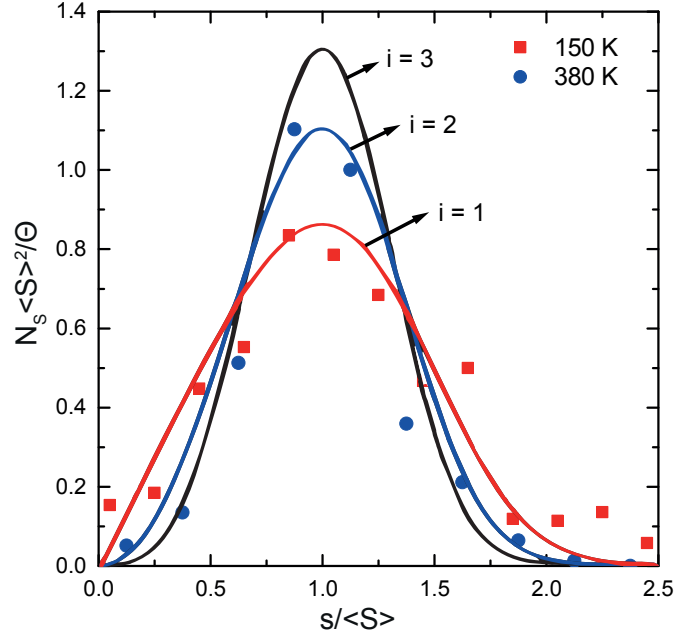


Figure 7.2 – Island size distribution for samples grown at  $T_{\text{dep}} = 150$  K (red squares) and  $T_{\text{dep}} = 380$  K (blue dots). Curves: theoretical predictions for  $i = 1$  (red),  $i = 2$  (blue) and  $i = 3$  (black) [104].

increase of the critical cluster size  $i$ , where monomers and dimers are mobile and trimers are stable nuclei. By applying a linear regression in the first regime, using in Eq. 2.15,  $i = 1$  and  $\eta(\Theta) = 0.25$  [90] we derive from the slope and the intercept  $E_m = 139 \pm 43$  meV and  $\nu_0 = 1.1 \times 10^{8 \pm 1}$  Hz, respectively. The estimated attempt frequency is four orders of magnitude smaller compared to typical values for surface diffusion. This indicates that some processes not included in the nucleation theory affect the Rh adatom diffusion and thus the island densities between the range  $170 \text{ K} \leq T_{\text{dep}} \leq 280 \text{ K}$ .

Imposing the linear regime with  $i = 1$  only for  $T_{\text{dep}} = 310$  K and  $T_{\text{dep}} \leq 170$  K (see Fig. 7.1a orange dashed lines) we derive a larger values for attempt frequency and monomer diffusion barrier:  $\nu_0 = 1.7 \times 10^9$  Hz and  $E_m = 164 \pm 43$  meV. The value of the attempt frequency is still unrealistic as it diverges substantially from the typical values of  $\nu_0$ . The  $E_m$  is comparable with the estimated  $E_m = 168 \pm 5$  meV for Ag/Pt(111) [107] for which the island density is much smaller for the corresponding  $T_{\text{dep}}$  (using similar F). These two arguments indicate that also the island density for  $T_{\text{dep}} = 310$  K is not described by nucleation theory and should be excluded in our analysis.

Omitting completely the data points for island densities between  $170 \text{ K} \leq T_{\text{dep}} \leq 310$  K and applying a linear fit for island densities between  $98 \text{ K} \leq T_{\text{dep}} \leq 150$  K we derive  $E_m = 214 \pm 32$  meV and  $\nu_0 = 1.3 \times 10^{11 \pm 0.7}$  Hz. In this regime, for all  $T_{\text{dep}}$  the island size distribution follows the corresponding theoretical curve for  $i = 1$  [104] (see Fig. 7.2 red squares). The extension of the linear regression cross the island density for  $T_{\text{dep}} = 350$  K

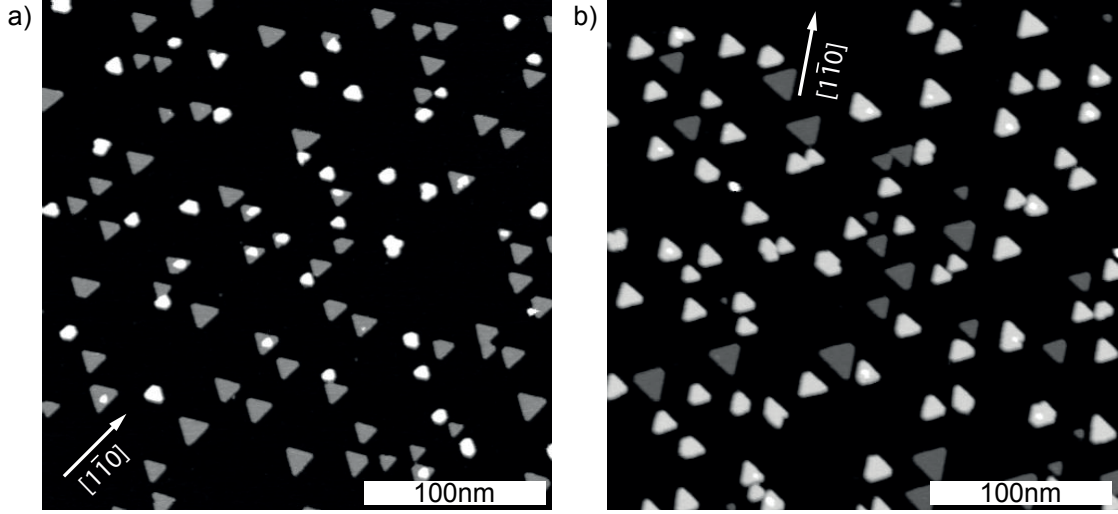


Figure 7.3 – STM topographies for Rh deposition at  $T_{\text{dep}} = 380$  K. a)  $\Theta_{\text{Rh}} = 0.12$  ML. The islands start to become double layer and change orientation,  $47 \pm 4\%$  of the islands are double layer. The island density is  $n_x = (6.8 \pm 0.4) \times 10^{-5}$  ML ( $V_t = -0.8$  V,  $I_t = 1$  nA). b)  $\Theta_{\text{Rh}} = 0.25$  ML. Most of the second layer islands are completely reversed, at this coverage  $73 \pm 3\%$  of the islands are double layer. The island density is in the saturation regime with  $n_x = (7.2 \pm 0.4) \times 10^{-5}$  ML ( $V_t = -1.0$  V,  $I_t = 1$  nA). Arrows indicate the step direction of the Pt(111) substrate.

indicating the end of the  $i = 1$  regime.  $T_{\text{dep}} = 350$  K also defines the onset of the regime with  $i = 2$ . Island size distributions for all experimental  $T_{\text{dep}}$  in this regime are reproducing accurately the theoretical curves for  $i = 2$  [104], as exemplified for  $T_{\text{dep}} = 380$  K in Fig. 7.2 (blue dots). The two red continuous lines in Fig. 7.1a are the linear regressions for the two regimes which approximately intersect at  $T_t = 360$  K. The slope of the linear regression in the second regime gives the dimer binding energy  $E_b$ . For  $i = 2$  in Eq. 2.15 we derive  $E_b = 464 \pm 15$  meV.

This latter choice is reasonable for the following reasons: i) The estimated monomer diffusion barrier  $E_{\text{m,Rh}} = 214 \pm 32$  meV outside the plateau, is slightly higher than for Co/Pt(111) ( $E_{\text{m,Co}} = 200 \pm 10$  meV [145]) using similar  $F$ , which is in line with the fact that the island densities are higher than in the case of Co/Pt(111) for the corresponding  $T_{\text{dep}}$ . ii) The same prefactor  $\nu_0$  is found by fitting the two regime with  $i = 1$  and  $i = 2$  with Eq. 2.15 as expected. iii) The same dimer dissociation energy is calculated using two different methods. The first method estimates the dimer dissociation barrier by summing the dimer binding energy and the monomer migration barrier calculated with the use of the rate equations:  $E_{\text{diss}} = E_b + E_{\text{m}} = 0.68 \pm 0.03$  eV. The second method, based on mean field arguments, uses the intersection temperature between the two linear regimes, namely  $T_t = 360$  K. At this temperature the dimer lifetime before dissociation  $\tau_{\text{diss}}$  becomes comparable to the time interval  $\Delta\tau$  between the dimer formation and the incorporation of one additional monomer stabilizing it to a trimer

(thus,  $\Delta\tau \approx n_x/F$  [248]). The dimer energy dissociation can be then estimated from  $E_{\text{diss}} = -k_B T_t \ln(1/\nu_0 \tau_{\text{diss}}) \approx -k_B T_t \ln(F/\nu_0 n_x) = 0.71 \pm 0.04$  eV. Both values are in good agreement and below the upper limit found for Rh<sub>2</sub> dissociation in gas phase  $E_{\text{diss}} = 2.75$  eV/atom [249]. In this work the Rh-Rh distance is 2.28 Å and thus closer than our 2.75 Å resulting from the Pt(111) lattice parameter, which explains the increased value.

We attribute the observed deviation from the nucleation theory for the island densities measured in the temperature range  $170 \text{ K} \leq T_{\text{dep}} \leq 310 \text{ K}$  to the contamination of the crystal surface with adsorbates originating from the residual gas. A good candidate for such adsorbate is CO which has been already demonstrated to modify the diffusion barrier of Pt adatoms on Pt(111) [98]. Below 170 K, CO molecules are immobile on the Pt(111) surface [250]. If the CO adsorbed amount is below  $10^{-3}$  ML, which sounds reasonable for a base pressure in the  $10^{-11}$  mbar range, no effect is seen on the Arrhenius plot given the much higher intrinsic density of the Rh islands. Above 170 K, CO can diffuse, meet Rh adatoms and pin them. At temperatures higher than 330 K the adsorbed CO molecules diffuse very fast to Pt(111) step edges where they stick. The consequent short residence time of the CO molecules on the Pt(111) terraces minimizes the CO-Rh sticking probability. Thus, also in the high temperature regime, no effect is expected on the Rh island density.

### 7.3 Island Morphology

For  $T_{\text{dep}} = 100 \text{ K}$  islands are small and due to the convolution with the STM tip we are unable to determine any preferred growth direction for the island edges (see Fig. 7.1b). For Rh deposited in the range  $120 \text{ K} \leq T_{\text{dep}} \leq 200 \text{ K}$ , the island shape becomes ramified, growing small branches perpendicular to A steps ( $\{100\}$ -facet, see section 2.2.4), a characteristic example is shown in Fig. 7.1c. Above  $T_{\text{dep}} = 200 \text{ K}$  and up to 250 K the islands are small and of compact shape (not shown). The next regime is found for  $250 \text{ K} \leq T_{\text{dep}} \leq 280 \text{ K}$  where islands have become more compact in shape with a small amount of the ensemble to be trigonal (Fig. 7.3d). At  $T_{\text{dep}} = 310 \text{ K}$ , all islands have trigonal shape with sides grown preferentially perpendicularly to A steps and a small amount of Rh is observed on the second layer. The deposition at  $T_{\text{dep}} = 350 \text{ K}$  results in trigonal islands with atomically sharp edges, growing in the same preferred direction as previously. In this case islands start to develop a second layer which is not proportional to their size, as seen in Fig. 7.1e.

At  $T_{\text{dep}} = 380 \text{ K}$  two species of islands are observed: single layer islands with their sides growing perpendicular to A steps and two monolayer-high islands which have rounded edges with island sides growing perpendicular to the B steps ( $\{111\}$ -facet, see Fig. 7.3a). This effect can be better seen after increasing the Rh coverage to 0.25 ML in Fig. 7.3b. The formation of the second layer is not caused by statistical growth,

as the probability of direct impingement of an adatom onto the top of an island is comparable to the coverage  $\Theta$ . Instead, here we observe the existence of either single layer or double layer islands, implying in the latter ones a flux of adatoms climbing from the first layer to the second. Scaling laws are valid for single layer islands only and thus, when a second layer is developed, it should be checked if the island ensemble still lies in the supersaturation regime. We observe an island density which is still in the saturation regime with  $n_x = (7.2 \pm 0.4) \times 10^{-5}$  ML, equal to the one for  $\Theta_{\text{Rh}} = 0.12$  ML,  $n_x = (6.8 \pm 0.4) \times 10^{-5}$  ML. At  $\Theta_{\text{Rh}} = 0.12$  ML about half of the islands have become double layer, whereas when  $\Theta_{\text{Rh}} = 0.25$  ML almost 75% of the islands are double layer. We observe an onset size for the islands to become complete double layer of  $1300 \pm 200$  atoms. This was found valid also for  $T_{\text{dep}} = 430$  K. At this temperature, only 10% of the islands remain single layer (see in Fig. 7.1f).

## 7.4 Conclusions

We have investigated the nucleation of Rh/Pt(111) by measuring the island density as a function of deposition temperature  $T_{\text{dep}}$  for a Rh coverage  $\Theta_{\text{Rh}} = 0.12$  ML, in order to find the correct decoration parameters for the formation of Co/Rh interline in pure Co islands. By imposing the linear regression for the  $98 \text{ K} \leq T_{\text{dep}} \leq 150 \text{ K}$  in the regime for  $i = 1$  we were able to derive satisfactory values for monomer diffusion barrier  $E_{\text{m}} = 214 \pm 32$  meV and attempt frequency  $\nu_0 = 1.3 \times 10^{11 \pm 0.7}$  Hz. At temperature higher than  $T_{\text{dep}} = 360$  K we observe a second regime with  $i = 2$ , we estimated the dissociation energy  $E_{\text{diss}} = 0.68 \pm 0.03$  eV. The island size distributions for all  $T_{\text{dep}}$  follow the theoretical curves expected for the different critical cluster size regimes. It was observed that Rh adatom is highly sensitive even to small amounts of CO adsorbates as their presence produces for  $170 \text{ K} \leq T_{\text{dep}} \leq 310 \text{ K}$  higher island densities than expected, despite the fact the pressure during deposition was always maintained below  $p_{\text{dep}} = 7 \times 10^{-11}$  mbar.







# Conclusions and Perspectives

The areal density in conventional magnetic storage media has recently surpassed the limit of 1 Tbit/in<sup>2</sup>. One promising method to further increase the areal density consists in building arrays of magnetic nanoclusters with uniform magnetic properties, as cluster superlattices by using self-organized growth on template surface. However, any further miniaturization of the bits can make comparable the anisotropy energy to the thermal energy and thus, the temperature marking the transition between the ferromagnetic to superparamagnetic state (which is called the superparamagnetic limit  $T_b$ ) tends to become smaller than room temperature. As the bits become smaller, a larger fraction of atoms is located at the particle surface with respect to the ones in the particle volume. Due to the reduced atom coordination at the surface, interfaces and interlines play a critical role to the magnetic anisotropy energy (MAE) and thus it is crucial to understand these interactions in order to engineer the MAE of small particles [62, 63]. In this thesis we have focused on two main objectives. The first considered the development of a procedure to grow high dense cluster arrays of rare earth on a template. Rare earth cluster arrays have never been studied before, despite their potential in magnetic applications. In the second, we aimed at tuning the magnetic hardness of nanostructures consisting of Co-core on Pt(111) by forming atomically sharp interlines and interfaces with a variety of  $4d$  elements. In both parts the nanostructures have been grown by atomic beam epitaxy (ABE) in ultra high vacuum conditions (UHV) and their morphological and magnetic properties have been characterized by scanning tunneling microscopy (STM) and magneto-optical Kerr effect (MOKE).

In the first part we used as template the graphene (gr) moiré pattern on Ir(111) as template. It results from the lattice mismatch between gr and Ir(111). The interparticle distance of 2.52 nm is defined by the moiré period, which corresponds to a density of 115 Tbit/in<sup>2</sup> [60]. We report the first cluster superlattice made of rare earths, namely Sm, grown on the moiré template of graphene/Ir(111). Sm clusters nucleate in registry with the moiré pattern, forming a superlattice when Sm is deposited for substrate temperatures between 80 K and 110 K. The superlattice shows high spatial order quality with the main source of disorder represented by the vacancies caused by graphene defects, which are approximately 12% of the moiré cells. The Sm cluster size distribution has a Gaussian shape with  $\sigma_{SD} = 0.31 \pm 0.01$  nm. For coverages up to  $\Theta_{Sm} = 0.5$  ML, Sm cluster

## Conclusions and Perspectives

---

spatial order is preserved yielding a mean cluster size of 50 atoms, while for higher coverages coalescence starts. Superlattices of Sm clusters with an average size of 9 atoms ( $\Theta_{\text{Sm}} = 0.08$  ML) lose the order by annealing at 140 K suggesting a weak Sm-graphene bonding. The Sm superlattice shows long-range order extending over several tens of nanometers and a cluster size distribution competing the finest superlattices grown by ABE. In addition to Sm, similar experiments were carried out for Dy in order to investigate whether the superlattice formation is a general property of rare earth elements on gr/Ir(111) or specific to Sm. For deposition temperatures ranging from 47 K to 210 K ( $\Theta_{\text{Dy}} = 0.07$  ML) we did not observe the formation of cluster arrays. A cluster density close to the graphene moiré density was found for  $T_{\text{dep}} = 70$  K, 10 K lower than for Sm. This observation suggests a lower diffusion barrier for Dy compared to Sm, in agreement with theoretical calculations on free-standing graphene [174].

The success in growing the Sm superlattice can open the possibility to grow two-element magnetic nanoclusters as for example  $\text{SmCo}_5$ , one of the strongest magnets discovered so far using Sm as cluster seeding element. For such 2D magnetic superlattices a clear breakthrough would be their extension in the third dimension. This 3D growth could be realized by adding another gr sheet on top of the existing nanocluster arrays. The gr cover sheet will have two beneficial purposes. i) It acts as a protective layer inhibiting contamination from residual adsorbates which degrade the magnetic properties of the nanoclusters. ii) Nucleation of nanoclusters on the second gr layer directly above the first array will pave the way for the formation, by repetition, of magnetic nanopillars as in the case of Co/Au [80, 251]. The expansion of the magnetic cluster arrays in the third dimension will increase the nanocluster volume by subsequent stacking and thus their MAE, pushing the superparamagnetic limit higher than room temperature while maintaining the areal density constant. One final consideration is the growth of the gr overlayers. The use of chemical vapor deposition (CVD) of hydrocarbon gas directly on the surface, due to high temperature annealing, can cause cluster coalescence which alters substantially the spatial order of the superlattice [252]. For this reason a gr transfer method from another surface as epitaxial single-crystal Cu(111) [253] on top of the grown superlattice could be more favorable to CVD as it could be realized also in UHV conditions without the annealing process.

The second part focuses on the study of a possible strategy to enhance the MAE of bimetallic nanostructures, grown on Pt(111), having a Co-core by forming atomically sharp interlines and interfaces with 4d elements, namely Ag, Pd and Rh. In this alternative approach to homogeneous cluster alloys, the interfaces and interlines were created via full control of extrinsic parameters in kinetic growth [91], as temperature and deposition flux, throughout the whole preparation procedure, in order to grow structures with desired morphological characteristics. The Co core islands selected for this study are single layer, compact in shape in order to form sharp atomic interlines and have a mean size of about 1200 atoms. In addition to the morphological and magnetic characterization of bimetallic nanostructures, susceptibility simulation analysis, using coherent rotation

(CR) and domain wall nucleation and propagation (DW) models, was performed in order to quantify the anisotropy energy contributions to the total MAE, coming from the interline ( $K_p$ ) and the interface ( $K_s$ ). We report an increased MAE when pure Co islands are capped by Ag, Rh and Pd, with Pd producing the largest variation in the blocking temperature,  $T_b$ . The capping with two Pd monolayers of pure Co islands has been found to maximize the  $T_b$  in agreement with previous studies on thin films [203, 204]. The lateral decoration of Co edges with all studied elements has been found to reduce the out-of-plane MAE, with Pd producing the smallest decrease in  $T_b$ .

The Pd capping of Co islands has been found as in a previous study [63] to shift the onset of superparamagnetic state at room temperature. During a complete Pd capping, the adatoms arriving at the terrace diffuse and attach to Co edges forming an interline. The contribution of this Co/Pd interline to the MAE is smaller with respect to the one coming from the edge Co atoms at the perimeter and thus reduces the positive effect from the Co/Pd interface. In order to shift the  $T_b$  to higher temperatures the Co/Pd interline has to be replaced either by an element that will act as a passivating spacer between Co edge atoms and Pd atoms after the Pd capping or an element that will increase the MAE of the Co perimeter atoms. Sm and Ce seem to be good candidates to this purpose. These two elements belong to the early lanthanides and since, their  $4f$  electron orbitals are less than half filled they couple ferromagnetically with the delocalized transition metal electrons leading to a higher moment and stronger magnetism [254]. In addition, they have the most aspherical  $4f$  orbital shape from all lanthanides [255]. Depending on the electron coupling with the edge Co atoms one of those two should align the longer axis of its orbital moment perpendicularly to the substrate, enhancing the out-of-plane MAE of the islands. Therefore  $3d$ - $4f$  interline could demonstrate a strong out of plane magnetization anisotropy which will be preserved after the Pd capping shifting the magnetic hardness to much higher than room temperatures. Preliminary test experiments performed during this thesis with Sm, did not lead to successful decoration because Sm has a strong tendency to alloy with the Pt at the surface and thus, an extensive study is necessary to define a possible recipe for the edge decoration.



# Appendix

## A.1 Supplementary information for Chapter 5

In this section are presented supplementary information for Rh cluster nucleation on graphene/Ir(111) and one example of a disordered system for which  $\xi$  is small and  $\kappa$  is large. In general for ordered systems  $\kappa$  indicates over which distance the spatial order is preserved. In low range-ordered or disordered systems, where  $\xi$  is small,  $\kappa$  parameter can be nonphysically high since both  $f$  and  $A_\infty$  are small. A characteristic example is shown in Fig. A.1.2, where  $\xi \approx 0.1$  and  $\kappa \approx 8.5$  nm.

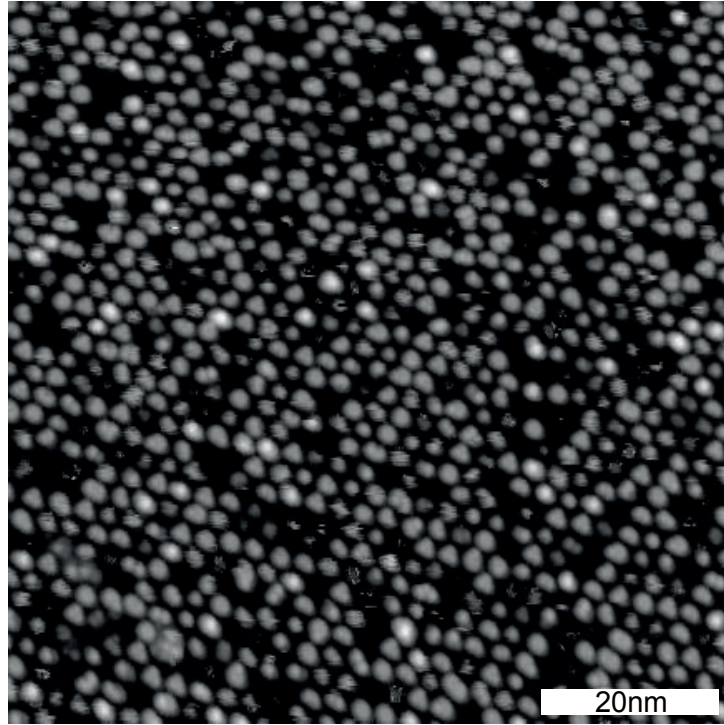


Figure A.1.1 – STM image of Rh clusters ( $\Theta_{\text{Rh}} = 0.12$  ML) grown at  $T_{\text{dep}} = 130$  K on graphene/Ir(111),  $\xi = 0.73$  and  $\kappa = 39.7$  nm ( $V_t = -1$  V,  $I_t = 60$  pA).

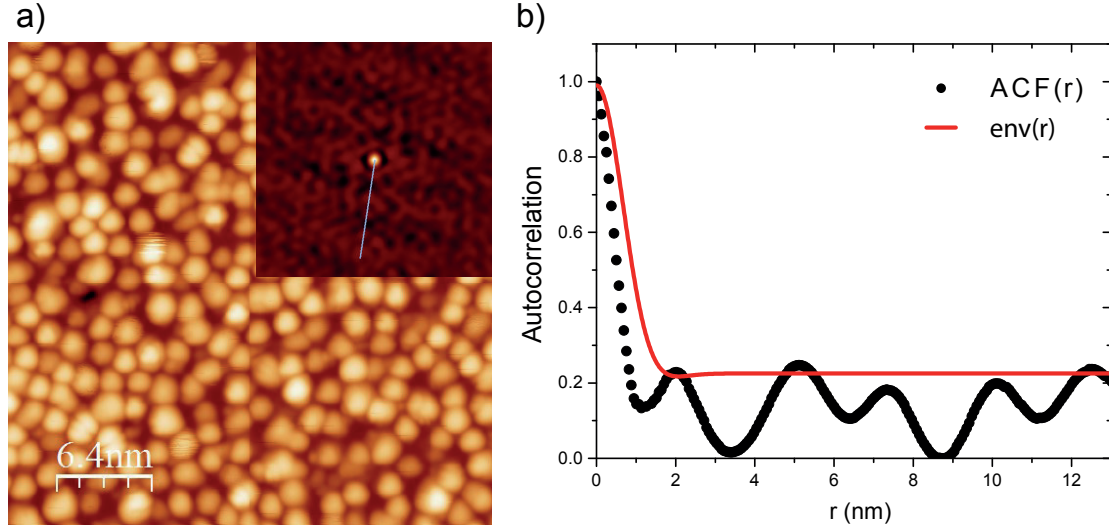


Figure A.1.2 – a) STM image for  $\Theta_{\text{Dy}} = 0.08 \text{ ML}$ ,  $T_{\text{dep}} = 47 \text{ K}$  ( $V_t = +1.0 \text{ V}$ ,  $I_t = 100 \text{ pA}$ ). Inset: 2D-ACF of the image in a), indicating short-range order. b) Line-profile from inset (black dots) and envelope fit with eq 5.1 (red line),  $\xi \approx 0.1$  and  $\kappa \approx 8.5 \text{ nm}$ .

## A.2 Mathematica Code used in Chapter 6

In this section are presented the main Mathematica code parts used for the simulation analysis in Chapter 6.

Building the  $\chi'(T)$  and  $\chi''(T)$  functions:

```
\[Mu] = 2.4* 0.0579; (* magnetic moment meV/T *)
\[Nu] =
  5*10^11; (* attempt frequency *)
\[Tau] = 1/\[Nu];
kB = 1/11.6; (* meV/K *)
Tmin = 30;
Tmax = 600;
F = 8.975; (* magnetic field frequency *)
n = 900; (* number of atoms *)
n\[Mu] = n \[Mu];
K = 0.9 n^0.8 ; (* anisotropy in meV *)
TB =
  K/kB/ Log[1/(2 Pi F \[Tau])];

chiprime[F_, T_, K_, n\[Mu]_] :=
  n\[Mu]^2/(kB T) 1/(1 + ( 2 \[Pi] F \[Tau] Exp[K/(kB T)])^2);
chisecond[F_, T_, K_, n\[Mu]_] :=
```

```

n\[Mu]^2/(kB T) (2 \[Pi] F \[Tau] Exp[K/(kB T)])/(
  1 + ( 2 \[Pi] F \[Tau] Exp[K/(kB T)]^2);
\[Chi][x_] = -(1/2) + E^(1/x)/(
  Sqrt\[Pi] Sqrt[x] Erfi[1/Sqrt[x]]) (* \[Chi]eq *)

sampleratiotab =
  Table[{Exp[x], \[Chi][Exp[x]] Exp[x]}, {x, -20, 20, .1}];
ratio = Interpolation[sampleratiotab] ;
(* chiprime and chisecond normalization *)
chi1[F_, T_, K_, n\[Mu]_] := chiprime[F, T, K, n\[Mu]] ratio[kB T/K];
chi2[F_, T_, K_, n\[Mu]_] := chisecond[F, T, K, n\[Mu]] ratio[kB T/K];

```

Fitting the background noise for clean Pt(111) sample:

```

(*A= amplitude, P= phase, B=background*)
T = (#1 + 4) & @@@
susceptibiliteB[[
  All, {1}]]; (* offset on the temperature that sometimes appears *)
\[Chi]B = (#1 Exp[I (#2) Pi/180]) & @@@ susceptibiliteB[[All, {2, 3}]];
\[Chi]AB = (#1) & @@@ susceptibiliteB[[All, {2}]];
\[Chi]PB = (#1) & @@@ susceptibiliteB[[All, {3}]];
(* fit of background noise for phase and amplitude *)
\[Chi]ABf =
  NonlinearModelFit[{T, \[Chi]AB} // Transpose, a + b x, {a, b, c}, x];
\[Chi]PBf =
  NonlinearModelFit[{T, \[Chi]PB} // Transpose, a + b x, {a, b, c},
    x];

```

Subtracting the background noise and correcting the phase and amplitude in order to derive the actual experimental  $\chi'(T)$  and  $\chi''(T)$  curves:

```

Phase = 115; (*offset on the phase to be adapted since it change from \
a measurement to the other *)

DeltaA = 11.8; (*offset on the amplitude to be adapted since it \
change from a measurement to the other *)

(* Building chi and \
subtracting the background noise *)

```



## Appendix

```
\[Chi]R = (#2 Exp[
    I \[Pi]/180 (#3 - Phase)] - ((\[Chi]ABf[#1 + DT] + DeltaA) *
    Exp[I \[Pi]/180 (\[Chi]PBf[#1 + DT] - Phase)])) & @@@
susceptibilite[All, {1, 2, 3}]];
\[Chi]max = Max[Abs\[Chi]R];
\[Chi]1max = Max[Abs[Re\[Chi]R]];
(* Plotting experimental chi1 and chi2 *)
suscdatRe =
ListPlot[{TR, Abs[Re\[Chi]R]]/\[Chi]1max} // Transpose]
suscdatIm =
ListPlot[{TR, Abs[Im\[Chi]R]]/\[Chi]1max} // Transpose]
```

Building simulating  $\chi'(T)$  and  $\chi''(T)$  curves using CR and DW reversal mechanisms for island sizes and perimeter extracted from STM topographies:

```
dataSet = Transpose[data];
(* setting columns *)
Coperimeter = dataSet[[1]];
Agperimeter = dataSet[[2]];
Coarea = dataSet[[3]];
Agarea = dataSet[[4]];

Subscript[i, in] = 1;
Subscript[i, fin] = Length[Coarea];

Seztot = 4*(Coarea + Agarea)/(Coperimeter + Agperimeter);
(* island cross section *)
SezAg = 1.95*Sqrt[Agarea/\[Pi] ]; (* Overlayer cross section *)
SezCo = Seztot - SezAg;
Subscript[d, nn] = 2.75 ; (* atom-atom distance in Angstrom *)
J = 1.5 10^(-11); (* J/m *)
A = J/(1.6 10^(-22))/(10^10/Subscript[d, nn]); (*meV/atom *)

Subscript[K, CoA] = 0.065; (* Ks for Co *)
Subscript[K, CoP] = 0.95; (* Kp for Co *)
Subscript[K, AgA] = 0.16; (* Ks for Ag *)
Subscript[K, AgP] = -0.12; (* Kp for Ag *)

Subscript[Etot, DW] =
4*(SezCo - 2)*Sqrt[A*Subscript[K, CoA]] +
4*SezAg*Sqrt[A*Subscript[K, AgA]] +
```

```

4*2*Sqrt[A*(Subscript[K, CoP] + Subscript[K, AgP])/2];
(* Domain wall model *)
Subscript[Etot, CR] =
  Subscript[K, CoA]*Coarea + Subscript[K, CoP]*Coperimeter +
  Subscript[K, AgA]*Agarea + Subscript[K, AgP]*Agperimeter;
(* Coherent rotation model *)
mult = 0.995;

(* Summing the smallest energy from the two models for all islands
as a function of temperature for chi1 and chi2 *)
fitchi1[T_] :=
  Sum[If[Subscript[Etot, DW][[i]] < Subscript[Etot, CR][[i]],
    chi1[F, T,
      Subscript[Etot, DW][[i]], \[Mu]*(Coarea[[i]] + Agarea[[i]])],
    chi1[F, T,
      Subscript[Etot, CR][[
        i]], \[Mu]*(Coarea[[i]] + Agarea[[i]])]], {i, Subscript[i, in],
      Subscript[i, fin]}(*Interval of islands in the sum*);
tabfitchi1 = Table[{T, fitchi1[T]}, {T, 1, 301, 1}];
tabchi1norm =
  Transpose[{tabfitchi1[[All, 1]], (* normaliation *)
    mult*tabfitchi1[[All, 2]]/Max[tabfitchi1[[All, 2]]]}];
fitchi2[T_] :=
  Sum[If[Subscript[Etot, DW][[i]] < Subscript[Etot, CR][[i]],
    chi2[F, T,
      Subscript[Etot, DW][[i]], \[Mu]*(Coarea[[i]] + Agarea[[i]])],
    chi2[F, T,
      Subscript[Etot, CR][[
        i]], \[Mu]*(Coarea[[i]] + Agarea[[i]])]], {i, Subscript[i, in],
      Subscript[i, fin]}(*Interval of islands in the sum*);
tabfitchi2 = Table[{T, fitchi2[T]}, {T, 1, 300, 1}];
tabchi2norm =
  Transpose[{tabfitchi2[[All, 1]], (* normaliation *)
    mult*tabfitchi2[[All, 2]]/Max[tabfitchi2[[All, 2]]]}];

(* Plotting simulated chi1 and chi2 curves *)
simchi1 =
  ListPlot[{tabchi1norm}, Joined -> True];
simchi2 =
  ListPlot[{tabchi2norm}, Joined -> True];

```



# Bibliography

- [1] B. Jacob, S. Ng, and D. Wang, *Memory Systems: Cache, DRAM, Disk* (Morgan Kaufmann Publishers Inc., San Francisco, CA, USA, 2007).
- [2] M. N. Baibich, J. M. Broto, A. Fert, F. N. Van Dau, F. Petroff, P. Etienne, G. Creuzet, A. Friederich, and J. Chazelas, Phys. Rev. Lett. **61**, 2472 (1988).
- [3] G. Binasch, P. Grünberg, F. Saurenbach, and W. Zinn, Phys. Rev. B **39**, 4828 (1989).
- [4] M. Julliere, Phys. Lett. A **54**, 225 (1975).
- [5] S. S. P. Parkin, C. Kaiser, A. Panchula, P. M. Rice, B. Hughes, M. Samant, and S.-H. Yang, Nat. Mater. **3**, 862 (2004).
- [6] S. Yuasa, T. Nagahama, A. Fukushima, Y. Suzuki, and K. Ando, Nat. Mater. **3**, 868 (2004).
- [7] M. Hattori, H. Suzuki, and S. Sugaya, “Trends in technologies for hdds, odds, and ssds,” Toshiba Storage Products For ICT Society (2010).
- [8] E. Grochowski, *Future Technology Challenges for NAND Flash and HDD Products*, Tech. Rep. (Flash Memory Summit, 2012).
- [9] HGST, *Perpendicular Magnetic Recording Technology*, Tech. Rep. (2007).
- [10] M. L. Plumer, J. van Ek, and W. C. Cain, ArXiv e-prints (2012).
- [11] H. J. Richter, J. Phys. D: Appl. Phys. **40**, R149 (2007).
- [12] P. Kasiraj, R. New, J. De Souza, and M. Williams, “System and method for writing data to hdd in bands,” (2005), uS Patent App. 10/674,093.
- [13] T. Albrecht (SPIE Bacus, 2009).
- [14] S. Xiao, X. Yang, K. Y. Lee, J. J. Hwu, K. Wago, and D. Kuo, J. Micro. Nanolithogr. MEMS MOEMS **12**, 031110 (2013).

## Bibliography

---

- [15] N. Weiss, T. Cren, M. Epple, S. Rusponi, G. Baudot, S. Rohart, A. Tejeda, V. Repain, S. Rousset, P. Ohresser, F. Scheurer, P. Bencok, and H. Brune, *Phys. Rev. Lett.* **95**, 157204 (2005).
- [16] T. R. Albrecht, H. Arora, V. Ayanoor-Vitikkate, J. M. Beaujour, D. Bedau, D. Berman, A. L. Bogdanov, Y. A. Chapuis, J. Cushen, E. E. Dobisz, G. Doerk, H. Gao, M. Grobis, B. Gurney, W. Hanson, O. Hellwig, T. Hirano, P. O. Jubert, D. Kercher, J. Lille, Z. Liu, C. M. Mate, Y. Obukhov, K. C. Patel, K. Rubin, R. Ruiz, M. Schabes, L. Wan, D. Weller, T. W. Wu, and E. Yang, *EEE Trans. Magn.* **51**, 1 (2015).
- [17] S. Sun, *Adv. Mater.* **18**, 393 (2006).
- [18] T. Hyeon, *Chem. Commun.* , 927 (2003).
- [19] C. Petit, A. Taleb, and M. P. Pileni, *J. Phys. Chem. B* **103**, 1805 (1999).
- [20] S. I. Woods, J. R. Kirtley, S. Sun, and R. H. Koch, *Phys. Rev. Lett.* **87**, 137205 (2001).
- [21] G. A. Held, G. Grinstein, H. Doyle, S. Sun, and C. B. Murray, *Phys. Rev. B* **64**, 012408 (2001).
- [22] A.-H. Lu, E. Salabas, and F. Schüth, *Angew. Chem. Int. Ed.* **46**, 1222 (2007).
- [23] X. Yang, S. Xiao, W. Wu, Y. Xu, K. Mountfield, R. Rottmayer, K. Lee, D. Kuo, and D. Weller, *J. Vac. Sci. Technol., B* **25**, 2202 (2007).
- [24] V. Auzelyte, C. Dais, P. Farquet, D. Grützmacher, L. J. Heyderman, F. Luo, S. Olliges, C. Padeste, P. K. Sahoo, T. Thomson, A. Turchanin, C. David, and H. H. Solak, *J Micro Nanolithogr MEMS MOEMS* **8**, 021204 (2009).
- [25] X. Yang, Y. Xu, C. Seiler, L. Wan, and S. Xiao, *J. Vac. Sci. Technol., B* **26**, 2604 (2008).
- [26] H. H. Solak and Y. Ekinici, *J. Vac. Sci. Technol., B* **25**, 2123 (2007).
- [27] X. Yang, Y. Xu, K. Lee, S. Xiao, D. Kuo, and D. Weller, *IEEE Trans. Magn.* **45**, 833 (2009).
- [28] J. Åkerman, *Science* **308**, 508 (2005).
- [29] E. Karl, Z. Guo, J. W. Conary, J. L. Miller, Y. G. Ng, S. Nalam, D. Kim, J. Keane, U. Bhattacharya, and K. Zhang, in *2015 IEEE International Solid-State Circuits Conference - (ISSCC) Digest of Technical Papers* (2015) pp. 1–3.
- [30] Intel, *14 nm lithography process*, Tech. Rep. (2015).

- [31] J. Z. Sun, “Spin-transfer torque switched magnetic tunnel junctions in magnetic random access memory,” (2016).
- [32] J. Sun, *IBM STT-MRAM 20th Anniversary Symposium*, Tech. Rep. (Thomas J. Watson Research Center, 2016).
- [33] J. Sato, M. Oogane, H. Naganuma, and Y. Ando, *Appl. Phys. Express* **4**, 113005 (2011).
- [34] S. Ikeda, J. Hayakawa, Y. Ashizawa, Y. M. Lee, K. Miura, H. Hasegawa, M. Tsunoda, F. Matsukura, and H. Ohno, *Appl. Phys. Lett.* **93**, 082508 (2008).
- [35] M. Hosomi, H. Yamagishi, T. Yamamoto, K. Bessho, Y. Higo, K. Yamane, H. Yamada, M. Shoji, H. Hachino, C. Fukumoto, H. Nagao, and H. Kano, in *IEEE International Electron Devices Meeting, 2005. IEDM Technical Digest.* (2005) pp. 459–462.
- [36] *J. Phys. Condens. Matter* **19**, 165209 (2007).
- [37] K. L. Wang, J. G. Alzate, and P. K. Amiri, *J. Phys. D: Appl. Phys.* **46**, 074003 (2013).
- [38] Y. Guan, J. Z. Sun, X. Jiang, R. Moriya, L. Gao, and S. S. P. Parkin, *Appl. Phys. Lett.* **95**, 082506 (2009).
- [39] D. C. Worledge, G. Hu, D. W. Abraham, J. Z. Sun, P. L. Trouilloud, J. Nowak, S. Brown, M. C. Gaidis, E. J. O’Sullivan, and R. P. Robertazzi, *Appl. Phys. Lett.* **98**, 022501 (2011).
- [40] S. Ikeda, K. Miura, H. Yamamoto, K. Mizunuma, H. D. Gan, K. Endo, S. Kanai, J. Hayakawa, F. Matsukura, and H. Ohno, *Nat. Mater.* **9**, 721 (2010).
- [41] A. Kikitsu, T. Maeda, H. Hieda, R. Yamamoto, N. Kihara, and Y. Kamata, *IEEE Trans. Magn.* **49**, 693 (2013).
- [42] M. P. Stoykovich and P. F. Nealey, *Materials Today* **9**, 20 (2006).
- [43] R. Ruiz, H. Kang, F. A. Detcheverry, E. Dobisz, D. S. Kercher, T. R. Albrecht, J. J. de Pablo, and P. F. Nealey, *Science* **321**, 936 (2008).
- [44] B. Voigtländer, G. Meyer, and N. M. Amer, *Phys. Rev. B* **44**, 10354 (1991).
- [45] A. T. N’Diaye, S. Bleikamp, P. J. Feibelman, and T. Michely, *Phys. Rev. Lett.* **97**, 215501 (2006).
- [46] F. D. Natterer, S. Rusponi, M. Papagno, C. Carbone, and H. Brune, *J. Phys. Condens. Matter* **24**, 314203 (2012).

## Bibliography

---

- [47] S. Schumacher, *Structure, Magnetism, and Binding of Novel Two-Dimensional Materials: Europium-Intercalated Graphene, Cluster Lattices, and Polar Oxide Bilayers*, Ph.D. thesis, Universität zu Köln (2014).
- [48] A. T. N'Diaye, T. Gerber, C. Busse, J. Mysliveček, J. Coraux, and T. Michely, *New J. Phys.* **11**, 103045 (2009).
- [49] S. Rousset, V. Repain, G. Baudot, Y. Garreau, and J. Lecoeur, *J. Phys. Condens. Matter* **15**, S3363 (2003).
- [50] H. Brune, M. Giovannini, K. Bromann, and K. Kern, *Nature* **394**, 451 (1998).
- [51] A. Cavallin, L. Fernández, M. Ilyn, A. Magaña, M. Ormaza, M. Matena, L. Vitali, J. E. Ortega, C. Grazioli, P. Ohresser, S. Rusponi, H. Brune, and F. Schiller, *Phys. Rev. B* **90**, 235419 (2014).
- [52] I. Brihuega, C. H. Michaelis, J. Zhang, S. Bose, V. Sessi, J. Honolka, M. A. Schneider, A. Enders, and K. Kern, *Surf. Sci.* **602**, L95 (2008).
- [53] S. Degen, C. Becker, and K. Wandelt, *Farad. Discuss.* **125**, 343 (2004).
- [54] M. Pivetta, G. E. Pacchioni, U. Schlickum, J. V. Barth, and H. Brune, *Phys. Rev. Lett.* **110**, 086102 (2013).
- [55] J.-L. Li, J.-F. Jia, X.-J. Liang, X. Liu, J.-Z. Wang, Q.-K. Xue, Z.-Q. Li, J. S. Tse, Z. Zhang, and S. B. Zhang, *Phys. Rev. Lett.* **88**, 066101 (2002).
- [56] R. Skomski and D. Sellmyer, *J. Rare Earths* **27**, 675 (2009).
- [57] F. Donati, S. Rusponi, S. Stepanow, C. Wäckerlin, A. Singha, L. Persichetti, R. Baltic, K. Diller, F. Patthey, E. Fernandes, J. Dreiser, Ž. Šljivančanin, K. Kummer, C. Nistor, P. Gambardella, and H. Brune, *Science* **352**, 318 (2016).
- [58] A. Singha, F. Donati, C. Wäckerlin, R. Baltic, J. Dreiser, M. Pivetta, S. Rusponi, and H. Brune, *Nano Lett.* **16**, 3475 (2016).
- [59] M. Steinbrecher, A. Sonntag, M. d. S. Dias, M. Bouhassoune, S. Lounis, J. Wiebe, R. Wiesendanger, and A. A. Khajetoorians, *Nat. Commun.* **7**, 10454 EP (2016).
- [60] R. Baltic, M. Pivetta, F. Donati, C. Wäckerlin, A. Singha, J. Dreiser, S. Rusponi, and H. Brune, *Nano Letters* **16**, 7610 (2016).
- [61] K.-H. Meiwes-Broer, *Metal Clusters at Surfaces: Structure, Quantum Properties, Physical Chemistry* (Springer Berlin Heidelberg, 2000) Chap. Electronic Level Structure of Metal Clusters at Surfaces, pp. 151–173.
- [62] S. Rusponi, T. Cren, N. Weiss, M. Epple, P. Bulushek, L. Claude, and H. Brune, *Nat. Mater.* **2**, 546 (2003).



- [63] S. Ouazi, S. Vlaic, S. Rusponi, G. Moulas, P. Bulushek, K. Halleux, S. Bornemann, S. Mankovsky, J. Minár, J. Staunton, H. Ebert, and H. Brune, *Nat. Commun.* **3**, 1313 (2012).
- [64] Q. Dong, W. Qu, W. Liang, K. Guo, H. Xue, Y. Guo, Z. Meng, C.-L. Ho, C.-W. Leung, and W.-Y. Wong, *Nanoscale* **8**, 7068 (2016).
- [65] C. Petit, S. Rusponi, and H. Brune, *J. Appl. Phys.* **95**, 4251 (2004).
- [66] B. Odom, D. Hanneke, B. D’Urso, and G. Gabrielse, *Phys. Rev. Lett.* **97**, 030801 (2006).
- [67] S. Bornemann, O. Šipr, S. Mankovsky, S. Polesya, J. B. Staunton, W. Wurth, H. Ebert, and J. Minár, *Phys. Rev. B* **86**, 104436 (2012).
- [68] P. Bruno, *Phys. Rev. B* **39**, 865 (1989).
- [69] G. van der Laan, *J. Phys. Condens. Matter* **10**, 3239 (1998).
- [70] L. Néel, *J. Phys. Radium* **15**, 376 (1954).
- [71] E. C. Stoner and E. P. Wohlfarth, *Phil. Trans. R. Soc. A* **240**, 599 (1948).
- [72] H.-B. Braun, *Phys. Rev. Lett.* **71**, 3557 (1993).
- [73] M. Bode, O. Pietzsch, A. Kubetzka, and R. Wiesendanger, *Phys. Rev. Lett.* **92**, 067201 (2004).
- [74] A. Cavallin, F. D. Natterer, S. Ouazi, G. Moulas, A. Lehnert, S. Rusponi, and H. Brune, *Phys. Rev. B* **90**, 144427 (2014).
- [75] S. Ouazi, S. Wedekind, G. Rodary, H. Oka, D. Sander, and J. Kirschner, *Phys. Rev. Lett.* **108**, 107206 (2012).
- [76] X. Batlle and A. Labarta, *J. Phys. D: Appl. Phys.* **35**, 15 (2002).
- [77] L. Néel, *Ann. Géophys* **5**, 99 (1949).
- [78] W. F. Brown, *Phys. Rev.* **130**, 1677 (1963).
- [79] R. Chantrell, N. Ayoub, and J. Popplewell, *J. Magn. Magn. Mater.* **53**, 199 (1985).
- [80] O. Fruchart, P.-O. Jubert, C. Meyer, M. Klaua, J. Barthel, and J. Kirschner, *J. Magn. Magn. Mater.* **239**, 224 (2002).
- [81] R. W. Chantrell, N. Walmsley, J. Gore, and M. Maylin, *Phys. Rev. B* **63**, 024410 (2000).
- [82] K. Wandelt, *Surface and Interface Science: Properties of Elemental Surfaces*, Vol. 2 (Wiley, 2012).

## Bibliography

---

- [83] G. Ehrlich and F. G. Hudda, J. Chem. Phys **44**, 1039 (1966).
- [84] R. L. Schwoebel and E. J. Shipsey, J. Appl. Phys. **37**, 3682 (1966).
- [85] J. Krug, J. Stat. Phys. **87**, 505 (1997).
- [86] G. Zinsmeister, Thin Solid Films **2**, 497 (1968).
- [87] G. Zinsmeister, Thin Solid Films **7**, 51 (1971).
- [88] J. A. Venables, Philos. Mag. **27**, 697 (1973).
- [89] J. Evans, P. Thiel, and M. Bartelt, Surf. Sci. Rep. Surf. Sci. Rep. **61**, 1 (2006).
- [90] J. A. Venables, G. D. T. Spiller, and M. Hanbucken, Rep. Prog. Phys. **47**, 399 (1984).
- [91] H. Brune, Surf. Sci. Rep. **31**, 121 (1998).
- [92] T. A. Witten and L. M. Sander, Phys. Rev. Lett. **47**, 1400 (1981).
- [93] H. Brune, H. Röder, K. Bromann, K. Kern, J. Jacobsen, P. Stoltze, K. Jacobsen, and J. Nørskov, Surf. Sci. **349**, L115 (1996).
- [94] M. Hohage, M. Bott, M. Morgenstern, Z. Zhang, T. Michely, and G. Comsa, Phys. Rev. Lett. **76**, 2366 (1996).
- [95] P. Stoltze, J. Phys. Condens. Matter **6**, 9495 (1994).
- [96] J. Nørskov, K. Jacobsen, P. Stoltze, and L. Hansen, Surf. Sci. **283**, 277 (1993).
- [97] S. Ovesson, A. Bogicevic, and B. I. Lundqvist, Phys. Rev. Lett. **83**, 2608 (1999).
- [98] M. Kalff, G. Comsa, and T. Michely, Phys. Rev. Lett. **81**, 1255 (1998).
- [99] T. Michely, M. Hohage, M. Bott, and G. Comsa, Phys. Rev. Lett. **70**, 3943 (1993).
- [100] F. Family and P. Meakin, Phys. Rev. Lett. **61**, 428 (1988).
- [101] F. Family and P. Meakin, Phys. Rev. A **40**, 3836 (1989).
- [102] M. I. Baskes, Phys. Rev. B **46**, 2727 (1992).
- [103] J. G. Amar, F. Family, and P.-M. Lam, Phys. Rev. B **50**, 8781 (1994).
- [104] J. G. Amar and F. Family, Phys. Rev. Lett. **74**, 2066 (1995).
- [105] J. A. Stroschio and D. T. Pierce, Phys. Rev. B **49**, 8522 (1994).
- [106] J. A. Stroschio, D. T. Pierce, and R. A. Dragoset, Phys. Rev. Lett. **70**, 3615 (1993).

- [107] H. Brune, G. S. Bales, J. Jacobsen, C. Boragno, and K. Kern, *Phys. Rev. B* **60**, 5991 (1999).
- [108] H. Roder, E. Hahn, H. Brune, J.-P. Bucher, and K. Kern, *Nature* **366**, 141 (1993).
- [109] M. C. Bartelt, S. Günther, E. Kopatzki, R. J. Behm, and J. W. Evans, *Phys. Rev. B* **53**, 4099 (1996).
- [110] K. S. Novoselov, A. K. Geim, S. V. Morozov, D. Jiang, Y. Zhang, S. V. Dubonos, I. V. Grigorieva, and A. A. Firsov, *Science* **306**, 666 (2004).
- [111] Y. Zhang, Y.-W. Tan, H. L. Stormer, and P. Kim, *Nature* **438**, 201 (2005).
- [112] A. A. Balandin, S. Ghosh, W. Bao, I. Calizo, D. Teweldebrhan, F. Miao, and C. N. Lau, *Nano Lett.* **8**, 902 (2008).
- [113] C. Lee, X. Wei, J. W. Kysar, and J. Hone, *Science* **321**, 385 (2008).
- [114] J. Coraux, A. T. N'Diaye, C. Busse, and T. Michely, *Nano Lett.* **8**, 565 (2008).
- [115] X. Zhou, Y. Wei, Q. He, F. Boey, Q. Zhang, and H. Zhang, *Chem. Commun.* **46**, 6974 (2010).
- [116] Z. Wang, X. Zhou, J. Zhang, F. Boey, and H. Zhang, *J. Phys. Chem. C* **113**, 14071 (2009).
- [117] Q. He, H. G. Sudibya, Z. Yin, S. Wu, H. Li, F. Boey, W. Huang, P. Chen, and H. Zhang, *ACS Nano* **4**, 3201 (2010).
- [118] S. He, B. Song, D. Li, C. Zhu, W. Qi, Y. Wen, L. Wang, S. Song, H. Fang, and C. Fan, *Adv. Funct. Mater.* **20**, 453 (2010).
- [119] Y. Ohno, K. Maehashi, Y. Yamashiro, and K. Matsumoto, *Nano Lett.* **9**, 3318 (2009).
- [120] J. T. Robinson, F. K. Perkins, E. S. Snow, Z. Wei, and P. E. Sheehan, *Nano Lett.* **8**, 3137 (2008).
- [121] K. R. Ratinac, W. Yang, S. P. Ringer, and F. Braet, *Environ. Sci. Technol.* **44**, 1167 (2010).
- [122] A. A. Barlian, W. T. Park, J. R. Mallon, A. J. Rastegar, and B. L. Pruitt, *Proc. IEEE* **97**, 513 (2009).
- [123] J. J. Park, W. J. Hyun, S. C. Mun, Y. T. Park, and O. O. Park, *Appl. Mater. Interfaces* **7**, 6317 (2015).
- [124] A. Candini, S. Klyatskaya, M. Ruben, W. Wernsdorfer, and M. Affronte, *Nano Lett.* **11**, 2634 (2011).

## Bibliography

---

- [125] A. T. N'Diaye, J. Coraux, T. N. Plasa, C. Busse, and T. Michely, *New J. Phys.* **10**, 043033 (2008).
- [126] J. Coraux, A. T. N'Diaye, M. Engler, C. Busse, D. Wall, N. Buckanie, F.-J. M. zu Heringdorf, R. van Gastel, B. Poelsema, and T. Michely, *New J. Phys.* **11**, 023006 (2009).
- [127] E. Loginova, S. Nie, K. Thürmer, N. C. Bartelt, and K. F. McCarty, *Phys. Rev. B* **80**, 085430 (2009).
- [128] H. Hattab, A. T. N'Diaye, D. Wall, G. Jnawali, J. Coraux, C. Busse, R. van Gastel, B. Poelsema, T. Michely, F.-J. M. zu Heringdorf, and M. H. von Hoegen, *Appl. Phys. Lett.* **98**, 141903 (2011).
- [129] C. Vo-Van, A. Kimouche, A. Reserbat-Plantey, O. Fruchart, P. Bayle-Guillemaud, N. Bendiab, and J. Coraux, *Appl. Phys. Lett.* **98**, 181903 (2011).
- [130] J. Knudsen, P. J. Feibelman, T. Gerber, E. Grånäs, K. Schulte, P. Stratmann, J. N. Andersen, and T. Michely, *Phys. Rev. B* **85**, 035407 (2012).
- [131] C. Busse, P. Lazić, R. Djemour, J. Coraux, T. Gerber, N. Atodiresei, V. Caciuc, R. Brako, A. T. N'Diaye, S. Blügel, J. Zegenhagen, and T. Michely, *Phys. Rev. Lett.* **107**, 036101 (2011).
- [132] D. F. Förster, T. O. Wehling, S. Schumacher, A. Rosch, and T. Michely, *New J. Phys.* **14**, 023022 (2012).
- [133] P. J. Feibelman, *Phys. Rev. B* **80**, 085412 (2009).
- [134] P. J. Feibelman, *Phys. Rev. B* **77**, 165419 (2008).
- [135] D. Weller, O. Mosendz, G. Parker, S. Pisana, and T. S. Santos, *Phys. Status Solidi A* **210**, 1245 (2013).
- [136] G. Binnig, H. Rohrer, C. Gerber, and E. Weibel, *Phys. Rev. Lett.* **49**, 57 (1982).
- [137] S. Vlaic, *Magnetism and Atomic Scale Structure of Bimetallic Nanostructures at Surfaces*, Ph.D. thesis, École Polytechnique Fédérale de Lausanne (EPFL) (2013).
- [138] M.-C. Blüm, *Supramolecular assembly, chirality, and electronic properties of rubrene studied by STM and STS*, Ph.D. thesis, École Polytechnique Fédérale de Lausanne (EPFL) (2006).
- [139] J. Bardeen, *Phys. Rev. Lett.* **6**, 57 (1961).
- [140] J. Tersoff and D. R. Hamann, *Phys. Rev. B* **31**, 805 (1985).
- [141] M. Faraday, *Trans. R. Soc.* **5**, 592 (1845).

- 
- [142] J. Kerr, *Philos. Mag.* **3**, 321 (1877).
- [143] J. Kerr, *Philosophical Magazine Series 5* **5**, 161 (1878).
- [144] Z. Qiu and S. Bader, *MRS Bulletin* **20**, 34 (1995).
- [145] P. Bulushek, *Submonolayer growth of cobalt on metallic and insulating surfaces studied by scanning tunneling microscopy and kinetic Monte-Carlo simulations*, Ph.D. thesis, École Polytechnique Fédérale de Lausanne (EPFL) (2008).
- [146] P. Gambardella, S. Rusponi, M. Veronese, S. S. Dhesi, C. Grazioli, A. Dallmeyer, I. Cabria, R. Zeller, P. H. Dederichs, K. Kern, C. Carbone, and H. Brune, *Science* **300**, 1130 (2003).
- [147] P. Gambardella, S. S. Dhesi, S. Gardonio, C. Grazioli, P. Ohresser, and C. Carbone, *Phys. Rev. Lett.* **88**, 047202 (2002).
- [148] C.-Y. You and S.-C. Shin, *J. Appl. Phys.* **84**, 541 (1998).
- [149] Z. Q. Qiu and S. D. Bader, *Rev. Sci. Instrum.* **71**, 1243 (2000).
- [150] A. Lehnert, P. Bulushek, N. Weiss, J. Giesecke, M. Treier, S. Rusponi, and H. Brune, *Rev. Sci. Instrum.* **80**, 023902 (2009).
- [151] K. Besocke, *Surf. Sci.* **181**, 145 (1987).
- [152] N. Weiss, *Propriétés magnétiques de nanostructures de cobalt adsorbées*, Ph.D. thesis, École Polytechnique Fédérale de Lausanne (EPFL) (2004).
- [153] A. Lehnert, *Magnetism of Individual atoms and of Epitaxial Monolayers*, Ph.D. thesis, École Polytechnique Fédérale de Lausanne (EPFL) (2009).
- [154] R. Gaisch, J. K. Gimzewski, B. Reihl, R. R. Schlittler, M. Tschudy, and W. D. Schneider, *Ultramicroscopy* **42-44**, 1621 (1992).
- [155] I. Horcas, R. Fernández, J. M. Gómez-Rodríguez, J. Colchero, J. Gómez-Herrero, and A. M. Baro, *Rev. Sci. Instrum.* **78**, 013705 (2007).
- [156] K. Aït-Mansour, H. Brune, D. Passerone, M. Schmid, W. Xiao, P. Ruffieux, A. Buchsbaum, P. Varga, R. Fasel, and O. Gröning, *Phys. Rev. B* **86**, 085404 (2012).
- [157] K. Takayanagi, Y. Tanishiro, S. Takahashi, and M. Takahashi, *Surf. Sci.* **164**, 367 (1985).
- [158] J. Jia, J.-Z. Wang, X. Liu, Q.-K. Xue, Z.-Q. Li, Y. Kawazoe, and S. B. Zhang, *Appl. Phys. Lett.* **80**, 3186 (2002).
- [159] J.-Z. Wang, J.-F. Jia, Z.-H. Xiong, and Q.-K. Xue, *Phys. Rev. B* **78**, 045424 (2008).

## Bibliography

---

- [160] C. Wöll, S. Chiang, R. J. Wilson, and P. H. Lippel, *Phys. Rev. B* **39**, 7988 (1989).
- [161] J. V. Barth, H. Brune, G. Ertl, and R. J. Behm, *Phys. Rev. B* **42**, 9307 (1990).
- [162] M. Sicot, S. Bouvron, O. Zander, U. Rüdiger, Y. S. Dedkov, and M. Fonin, *Appl. Phys. Lett.* **96**, 093115 (2010).
- [163] A. K. Engstfeld, S. Beckord, C. D. Lorenz, and R. J. Behm, *ChemPhysChem* **13**, 3313 (2012).
- [164] S. Berner, M. Corso, R. Widmer, O. Groening, R. Laskowski, P. Blaha, K. Schwarz, A. Goriachko, H. Over, S. Gsell, M. Schreck, H. Sachdev, T. Greber, and J. Osterwalder, *Angew. Chem. Int. Ed.* **46**, 5115 (2007).
- [165] M. Schmid, G. Kresse, A. Buchsbaum, E. Napetschnig, S. Gritschneider, M. Reichling, and P. Varga, *Phys. Rev. Lett.* **99**, 196104 (2007).
- [166] G. Rau, S. Baumann, S. Rusponi, F. Donati, S. Stepanow, L. Gagnaniello, J. Dreiser, C. Piamonteze, F. Nolting, S. Gangopadhyay, O. R. Albertini, R. Macfarlane, C. P. Lutz, B. A. Jones, P. Gambardella, A. J. Heinrich, and H. Brune, *Science* **344**, 988 (2014).
- [167] S. Baumann, F. Donati, S. Stepanow, S. Rusponi, W. Paul, S. Gangopadhyay, G. Rau, G. E. Pacchioni, L. Gagnaniello, M. Pivetta, J. Dreiser, C. Piamonteze, C. P. Lutz, R. Macfarlane, B. A. Jones, P. Gambardella, A. J. Heinrich, and H. Brune, *Phys. Rev. Lett.* **115**, 237202 (2015).
- [168] D. Weller, A. Moser, L. Folks, M. E. Best, W. Lee, M. F. Toney, M. Schwickert, J. U. Thiele, and M. F. Doerner, *IEEE Trans. Magn.* **36**, 10 (2000).
- [169] T. Nozawa, S. Sato, and R. Takahashi, *Top. Catal.* **52**, 609 (2009).
- [170] J. Trillo and S. Bernal, *J. Catal.* **66**, 184 (1980).
- [171] A. de Klerk, *Top. Catal.* **57**, 715 (2014).
- [172] K. Tanabe, M. Misono, Y. Ono, and H. Hattori, *New Solid Acids and Bases Their Catalytic Properties*, *Stud. Surf. Sci. Catal.*, Vol. 51 (Elsevier, 1989).
- [173] N. W. C. Eric M. Kennedy, *Appl. Catal.*, Vol. 75 (Elsevier, 1991).
- [174] X. Liu, C.-Z. Wang, M. Hupalo, H.-Q. Lin, K.-M. Ho, and M. C. Tringides, *Crystals* **3**, 79 (2013).
- [175] B. Müller, L. Nedelmann, B. Fischer, H. Brune, and K. Kern, *Phys. Rev. B* **54**, 17858 (1996).
- [176] S. Pichler, M. I. Bodnarchuk, M. V. Kovalenko, M. Yarema, G. Springholz, D. V. Talapin, and W. Heiss, *ACS Nano* **5**, 1703 (2011).

- [177] E. A. Eklund, E. J. Snyder, and R. Williams, *Surf. Sci.* **285**, 157 (1993).
- [178] H.-N. Yang, Y.-P. Zhao, A. Chan, T.-M. Lu, and G.-C. Wang, *Phys. Rev. B* **56**, 4224 (1997).
- [179] S. Rusponi, G. Costantini, C. Boragno, and U. Valbusa, *Phys. Rev. Lett.* **81**, 4184 (1998).
- [180] N. A. Khan and C. Matranga, *Surf. Sci.* **602**, 932 (2008).
- [181] W. Cullen and P. First, *Surf. Sci.* **420**, 53 (1999).
- [182] F. H. Ellinger and W. H. Zachariasen, *J. Am. Chem. Soc.* **75**, 5650 (1953).
- [183] X. Liu, C. Z. Wang, M. Hupalo, W. C. Lu, M. C. Tringides, Y. X. Yao, and K. M. Ho, *Phys. Chem. Chem. Phys.* **14**, 9157 (2012).
- [184] B. Johansson, *Phys. Rev. B* **19**, 6615 (1979).
- [185] G. K. Wertheim and G. Crecelius, *Phys. Rev. Lett.* **40**, 813 (1978).
- [186] A. Stenborg, O. Björneholm, A. Nilsson, N. Mårtensson, J. N. Andersen, and C. Wigren, *Phys. Rev. B* **40**, 5916 (1989).
- [187] E. Lundgren, J. N. Andersen, R. Nyholm, X. Torrelles, J. Rius, A. Delin, A. Grechnev, O. Eriksson, C. Konvicka, M. Schmid, and P. Varga, *Phys. Rev. Lett.* **88**, 136102 (2002).
- [188] A. Buchsbaum, M. De Santis, H. C. N. Tolentino, M. Schmid, and P. Varga, *Phys. Rev. B* **81**, 115420 (2010).
- [189] D. D. Chambliss, R. J. Wilson, and S. Chiang, *Phys. Rev. Lett.* **66**, 1721 (1991).
- [190] S. Vlaic, L. Gragnaniello, S. Rusponi, A. Cavallin, F. Donati, Q. Dubout, C. Piamonteze, J. Dreiser, F. Nolting, and H. Brune, *Phys. Rev. B* **89**, 245402 (2014).
- [191] V. Repain, G. Baudot, H. Ellmer, and S. Rousset, *Mat. Sci. Eng. B-Solid* **96**, 178 (2002).
- [192] S. Piramanayagam and K. Srinivasan, *J. Magn. Magn. Mater.* **321**, 485 (2009).
- [193] I. M. Billas, A. Châtelain, and W. A. de Heer, *Science* **265**, 1682 (1994).
- [194] A. Chouairi, H. Dreyssé, H. Nait-Laziz, and C. Demangeat, *Phys. Rev. B* **48**, 7735 (1993).
- [195] S. Hashimoto, Y. Ochiai, and K. Aso, *Jpn. J. Appl. Phys.* **28**, 1596 (1989).
- [196] F. C. Chen, Y. E. Wu, C. W. Su, and C. S. Shern, *Phys. Rev. B* **66**, 184417 (2002).
- [197] T. Kingetsu and K. Sakai, *J. Appl. Phys.* **73**, 7622 (1993).



## Bibliography

---

- [198] T. Kingetsu, Japanese J. Appl. Phys. **33**, L106 (1994).
- [199] T. Kingetsu, J. Appl. Phys. **76**, 4267 (1994).
- [200] S. Purcell, M. Johnson, N. McGee, W. Zeper, and W. Hoving, J. Magn. Magn. Mater. **113**, 257 (1992).
- [201] J. Dorantes-Dávila, H. Dreyssé, and G. M. Pastor, Phys. Rev. Lett. **91**, 197206 (2003).
- [202] X. Ying, K. V. Rao, P. J. Jensen, and J. J. Xu, IEEE Trans. Magn. **34**, 876 (1998).
- [203] J. Kohlhepp and U. Gradmann, J. Magn. Magn. Mater. **139**, 347 (1995).
- [204] B. N. Engel, M. H. Wiedmann, R. A. Van Leeuwen, and C. M. Falco, Phys. Rev. B **48**, 9894 (1993).
- [205] R. Allenspach and A. Bischof, Phys. Rev. Lett. **69**, 3385 (1992).
- [206] B. N. Engel, M. H. Wiedmann, and C. M. Falco, J. Appl. Phys. **75**, 6401 (1994).
- [207] S. Boukari, E. Beaurepaire, H. Bulou, B. Carrière, J. P. Deville, F. Scheurer, M. De Santis, and R. Baudoing-Savois, Phys. Rev. B **64**, 144431 (2001).
- [208] H. Li, S. C. Wu, D. Tian, Y. S. Li, J. Quinn, and F. Jona, Phys. Rev. B **44**, 1438 (1991).
- [209] J. Redinger, S. Blügel, and R. Podloucky, Phys. Rev. B **51**, 13852 (1995).
- [210] A. Mokrani, H. Dreyssé, S. Bouarab, and C. Demangeat, J. Magn. Magn. Mater. **113**, 201 (1992).
- [211] S. Blügel, Phys. Rev. Lett. **68**, 851 (1992).
- [212] U. Pustogowa, J. Zabloudil, C. Uiberacker, C. Blaas, P. Weinberger, L. Szunyogh, and C. Sommers, Phys. Rev. B **60**, 414 (1999).
- [213] J. Thiele, C. Boeglin, K. Hricovini, and F. Chevrier, Phys. Rev. B **53**, R11934 (1996).
- [214] C. Shern, J. Tsay, H. Her, Y. Wu, and R. Chen, Surf. Sci. **429**, L497 (1999).
- [215] A. Lehnert, S. Dennler, P. Błoński, S. Rusponi, M. Etzkorn, G. Moulas, P. Bencok, P. Gambardella, H. Brune, and J. Hafner, Phys. Rev. B **82**, 094409 (2010).
- [216] P. Błoński, A. Lehnert, S. Dennler, S. Rusponi, M. Etzkorn, G. Moulas, P. Bencok, P. Gambardella, H. Brune, and J. Hafner, Phys. Rev. B **81**, 104426 (2010).
- [217] A. Hillion, A. Cavallin, S. Vlaic, A. Tamion, F. Tournus, G. Khadra, J. Dreiser, C. Piamonteze, F. Nolting, S. Rusponi, K. Sato, T. J. Konno, O. Proux, V. Dupuis, and H. Brune, Phys. Rev. Lett. **110**, 087207 (2013).

- [218] J. Stöhr and H. Siegmann, *Magnetism: From Fundamentals to Nanoscale Dynamics*, Springer Series in Solid-State Sciences (Springer Berlin Heidelberg, 2006).
- [219] C.-J. Lin, G. Gorman, C. Lee, R. Farrow, E. Marinero, H. Do, H. Notarys, and C. Chien, *J. Magn. Magn. Mater.* **93**, 194 (1991).
- [220] R. Kunkel, B. Poelsema, L. K. Verheij, and G. Comsa, *Phys. Rev. Lett.* **65**, 733 (1990).
- [221] O. Robach, C. Quiros, P. Steadman, K. F. Peters, E. Lundgren, J. Alvarez, H. Isern, and S. Ferrer, *Phys. Rev. B* **65**, 054423 (2002).
- [222] G. Moulas, A. Lehnert, S. Rusponi, J. Zabloudil, C. Etz, S. Ouazi, M. Etzkorn, P. Bencok, P. Gambardella, P. Weinberger, and H. Brune, *Phys. Rev. B* **78**, 214424 (2008).
- [223] T. Cren, S. Rusponi, N. Weiss, M. Epple, and H. Brune, *J. Phys. Chem. B* **108**, 14685 (2004).
- [224] W. Wernsdorfer, E. B. Orozco, K. Hasselbach, A. Benoit, B. Barbara, N. Demoncy, A. Loiseau, H. Pascard, and D. Mailly, *Phys. Rev. Lett.* **78**, 1791 (1997).
- [225] W. Wernsdorfer, B. Doudin, D. Mailly, K. Hasselbach, A. Benoit, J. Meier, J. P. Ansermet, and B. Barbara, *Phys. Rev. Lett.* **77**, 1873 (1996).
- [226] H.-B. Braun, *J. Appl. Phys.* **99**, 08F908 (2006).
- [227] H.-B. Braun, *J. Appl. Phys.* **85**, 6172 (1999).
- [228] S. Rohart, V. Repain, A. Thiaville, and S. Rousset, *Phys. Rev. B* **76**, 104401 (2007).
- [229] S. Rohart, P. Campiglio, V. Repain, Y. Nahas, C. Chacon, Y. Girard, J. Lagoute, A. Thiaville, and S. Rousset, *Phys. Rev. Lett.* **104**, 137202 (2010).
- [230] P. Politi and M. G. Pini, *Phys. Rev. B* **66**, 214414 (2002).
- [231] H. Röder, R. Schuster, H. Brune, and K. Kern, *Phys. Rev. Lett.* **71**, 2086 (1993).
- [232] F. den Broeder, W. Hoving, and P. Bloemen, *J. Magn. Magn. Mater.* **93**, 562 (1991).
- [233] P. Ohresser, E. Otero, F. Wilhelm, A. Rogalev, C. Goyhenex, L. Joly, H. Bulou, M. Romeo, V. Speisser, J. Arabski, G. Schull, and F. Scheurer, *J. Appl. Phys.* **114**, 223912 (2013).
- [234] M. Ohtake, S. Ouchi, F. Kirino, and M. Futamoto, *J. Appl. Phys.* **111**, 07A708 (2012).

## Bibliography

---

- [235] A. Murdoch, A. Trant, J. Gustafson, T. Jones, T. Noakes, P. Bailey, and C. Baddeley, *Surf. Sci.* **608**, 212 (2013).
- [236] L. Vivas, A. Figueroa, F. Bartolomé, J. Rubín, L. García, C. Deranlot, F. Petroff, L. Ruiz, J. González-Calbet, N. Brookes, F. Wilhelm, A. Rogalev, and J. Bartolomé, *J. Magn. Magn. Mater.* **400**, 248 (2016).
- [237] B. N. Engel, C. D. England, R. A. Van Leeuwen, M. H. Wiedmann, and C. M. Falco, *Phys. Rev. Lett.* **67**, 1910 (1991).
- [238] P. Manchanda, R. Skomski, P. K. Sahota, M. Franchin, H. Fangohr, and A. Kashyap, *J. Appl. Phys.* **111**, 07C724 (2012).
- [239] V. Kamberský, P. de Haan, J. Šimšová, S. Porthun, R. Gemperle, and J. Lodder, *J. Magn. Magn. Mater.* **157**, 301 (1996).
- [240] G. H. O. Daalderop, P. J. Kelly, and M. F. H. Schuurmans, *Phys. Rev. B* **42**, 7270 (1990).
- [241] G. H. O. Daalderop, P. J. Kelly, and M. F. H. Schuurmans, *Phys. Rev. B* **50**, 9989 (1994).
- [242] T. Burkert, L. Nordström, O. Eriksson, and O. Heinonen, *Phys. Rev. Lett.* **93**, 027203 (2004).
- [243] S. Blizak, G. Bihlmayer, S. Blügel, and S. E. H. Abaidia, *Phys. Rev. B* **91**, 014408 (2015).
- [244] O. Šipr, S. Bornemann, H. Ebert, S. Mankovsky, J. Vackář, and J. Minár, *Phys. Rev. B* **88**, 064411 (2013).
- [245] J. Hafner and D. Spišák, *Phys. Rev. B* **76**, 094420 (2007).
- [246] V. Sessi, K. Kuhnke, J. Zhang, J. Honolka, K. Kern, C. Tieg, O. Šipr, J. Minár, and H. Ebert, *Phys. Rev. B* **82**, 184413 (2010).
- [247] S. Rousset, B. Croset, Y. Girard, G. Prévot, V. Repain, and S. Rohart, *C. R. Phys.* **6**, 33 (2005).
- [248] P. J. Feibelman and T. Michely, *Surf. Sci.* **492**, L723 (2001).
- [249] V. Piacente, G. Balducci, and G. Bardi, *J. Less-Common MET.* **37**, 123 (1974).
- [250] B. Poelsema, L. K. Verheij, and G. Comsa, *Phys. Rev. Lett.* **49**, 1731 (1982).
- [251] O. Fruchart, M. Klaua, J. Barthel, and J. Kirschner, *Phys. Rev. Lett.* **83**, 2769 (1999).
- [252] A. Cavallin, *Growth and Magnetism of Nanostructures Investigated by STM, MOKE, and XMCD*, Ph.D. thesis, École Polytechnique Fédérale de Lausanne (EPFL) (2013).

- [253] K. M. Reddy, A. D. Gledhill, C.-H. Chen, J. M. Drexler, and N. P. Padture, *Appl. Phys. Lett.* **98**, 113117 (2011).
- [254] K. H. J. Buschow and F. R. D. Boer, *J. Magn. Magn. Mater.* (Kluwer Academic, New York, 2003).
- [255] J. D. Rinehart and J. R. Long, *Chem. Sci.* **2**, 2078 (2011).



# Acknowledgements

First I thank my supervisor Professor Harald Brune for giving me the opportunity to carry out this research within his group and make this PhD thesis.

I want to thank Stefano Rusponi who supervised this work and with whom I have worked closely during these four years. I am grateful for all the technical discussions which allowed us to find optimal solutions when designing the experiments and moreover for his coaching, and experiential skills which steered this thesis to this fruitful outcome. I wish to thank Marina Pivetta for her support, her great contribution in data analysis and the experiments on rare earth superlattices and also for all scientific discussions.

I would also like to thank Professors Hugo Dil, Mikhail Fonin, Frédéric Mila and Dr. Johann Coraux for serving on the jury committee of this thesis.

I want to thank Fabio Donati for all the thoughtful scientific discussions, his constructive feedback, and the climbing activities.

I thank all the doctoral students and post doc members of our group: Aparajita Singha, Maximilian Bauer, Jean-Guillaume De Groot, Edgar Fernandes, Romana Baltić, Quentin Dubout, Hamed Achour, Giulia Pacchioni, Chongqi Yu, Darius Merk, Simone Borroni, Alberto Cavallin, Katharina Diller, Fabian Natterer, Luca Gragnaniello, Christian Wäckerlin and Nicolas Weiss for the great company and the colorful discussions during launches, coffee breaks and for all the fun moments we had during the group outings.

My most heartfelt gratitude goes to my parents and my sister Niki who had always supported me and believed in my resolve. Σας ευχαριστώ για την στήριξη, συμπαράσταση, εμπιστοσύνη και αμέριστη αγάπη που μου δείξατε όλα αυτά τα χρόνια!

Last, I have kept my earnest thanks to my beloved companion Sophia for her unstinting support and inspiration all these years. Σοφία μου σε ευχαριστώ!

*Lausanne, 28 June 2017*

Δημήτρης Μουσαδάκος





# Dimitris Mousadakos

---

## *Curriculum Vitae*

---

### Education

- 2017 **PhD**, *Physics*, Swiss Federal Institute of Technology in Lausanne (EPFL).  
2012 **MSc**, *Microsystems and Nanodevices*, National Technical University of Athens.  
2010 **Diploma**, *Physics*, National and Kapodistrian University of Athens.

---

### Skills

- IT Python, Mathematica, C, Fortran, Pascal, ImageJ, OriginLab, Latex, MS Office, Adobe: Lightroom, Photoshop, Illustrator
- Experimental Techniques Scanning Tunneling Microscope (STM), Magneto-Optical Kerr Effect (MOKE), Molecular Beam Epitaxy (MBE), Powder Preparation, Melt-Spinning, Scanning Electron Microscope (SEM), Atomic Force Microscopy (AFM), Surface Profilometry, Vibrating Sample Magnetometer (VSM), Nanolithography, Lithography Mask Design, Nanoparticle Deposition (Magnetron-DC Sputtering), X-Ray Diffraction

---

### Languages

- English Fluent  
German Grundstufe (B1)  
French B1  
Greek Native

---

### Personal Details

- Date of Birth 26.04.1982  
Nationality Greek  
email dmousadakos@gmail.com  
Skype dmousadakos  
Linkedin [www.linkedin.com/in/dmousadakos](http://www.linkedin.com/in/dmousadakos)

---

### Publications

- D. Mousadakos, M. Pivetta, H. Brune, and S. Rusponi. Sm cluster superlattice on graphene/ir(111). *New J. Phys.*, (submitted), 2017.

- E. Skotadis, D. Mousadakos, J. Tanner, D. Tsoukalas, and P. Broutas. Flexible platinum nanoparticle strain sensors. In *Proceedings of the European Solid-State Device Research Conference (ESSDERC)*, pages 354–357, Sept 2013.
- E. Skotadis, D. Mousadakos, K. Katsabrokou, S. Stathopoulos, and D. Tsoukalas. Flexible polyimide chemical sensors using platinum nanoparticles. *Sensor Actuat B-Chem*, 189:106 – 112, 2013.
- E. Skotadis, D. Mousadakos, K. Katsabrokou, S. Stathopoulos, and D. Tsoukalas. Platinum nanoparticle chemical sensors on polyimide substrates. *Procedia Eng.*, 47:778 – 781, 2012.
- J.L. Tanner, D. Mousadakos, K. Giannakopoulos, E. Skotadis, and D. Tsoukalas. High strain sensitivity controlled by the surface density of platinum nanoparticles. *Nanotechnology*, 23(28):285501, 2012.
- J.L. Tanner, D. Mousadakos, P. Broutas, S. Chatzandroulis, Y.S. Raptis, and D. Tsoukalas. Nanoparticle strain sensor. *Procedia Eng.*, 25:635 – 638, 2011.

